Wayne State University Dissertations

1-1-2011

Computational simulation of skull fracture patterns in pediatric subjects using a porcine model

Christina Devito Wagner
Wayne State University,

Follow this and additional works at: http://digitalcommons.wayne.edu/oa_dissertations

Part of the Biomechanics Commons, and the Biomedical Engineering and Bioengineering Commons

**COMPUTATIONAL SIMULATION OF SKULL FRACTURE PATTERNS
IN PEDIATRIC SUBJECTS USING A PORCINE MODEL**

by

CHRISTINA DEVITO WAGNER

DISSERTATION

Submitted to the Graduate School

of Wayne State University,

Detroit, Michigan

in partial fulfillment of the requirements

for the degree of

DOCTOR OF PHILOSOPHY

2012

MAJOR: BIOMEDICAL ENGINEERING

Approved by:

_____   _____
Advisor   Date

_____   _____

_____   _____

_____   _____

ACKNOWLEDGMENTS

In completion of this work, I would like to express my appreciation to the scientists and researchers who have helped me along the way. Firstly, my advisor, Dr. King-Hay Yang, and the entire staff of the Wayne State University Bioengineering Center, who gave me the opportunity to learn a wide variety of skills in my years in our department. Not only have I been given the chance to perform both experimental and computational impact biomechanics research while working on many different projects, I have also acquired invaluable administration, communication, and technology proficiencies that I do not believe I would have become skilled at elsewhere. My fellow students in the Advanced Human Modeling Laboratory have been a source of inspiration and technical support, when necessary. I would especially like to thank Drs. Liying Zhang, Paul Begeman, Haojie Mao, Xin Jin, and Aditya Belwadi, who have been with me practically from the beginning. And lastly, I must express my gratitude to the chair of the Biomedical Engineering Department, Dr. Albert King, without whom, the tradition of biomechanics research at Wayne State would not be what it is today.

My co-investigators, especially those at Michigan State University, have been immeasurably valuable in providing their data and expertise to this work. These people include Dr. Roger Haut, Dr. Todd Fenton, Eric Meyer, Tim Baumer, Brian Powell, and Nic Passalaqua. A computational model cannot be developed accurately without experimental data, and I believe the collaboration we undertook yielded meaningful results for the biomechanics and forensics scientific communities. Additionally, the role of radiology in this work cannot be understated. The Department of Radiology at the

Wayne State University College of Medicine, especially Dr. Wilbur Smith, has been consistently supportive of our biomechanics research efforts.

A final note:

The emotional support of my family and friends is something that I took for granted when I began graduate school. However, now that I have reached my goals and am embarking on a new road in life, I realize that none of this would have been possible without them. My parents instilled in me a curious mind and always encouraged me to think critically and aim high. My brother and my friends, in particular some who I met near the end of this journey, have been unwavering in their belief in my abilities, even when I doubted myself. Their contributions may seem minimal from a scientific perspective, but I assure you, they are the very foundation of this work.

TABLE OF CONTENTS

CHAPTER 1

INTRODUCTION

Motivation and Background

In cases of suspected child abuse with skeletal trauma, it is often the role of the injury biomechanist, forensic pathologist, clinical radiologist and forensic anthropologist to determine the mechanism of injury when child victims cannot speak for themselves. This is a challenging task, especially for the head, as comprehensive biomechanical data on skull fracture in infants and children do not currently exist, and frequently the determination regarding cause of injury is based on anecdotal evidence from the medical literature and unsubstantiated eyewitness accounts. The current process can result in unreliable autopsy interpretation and miscarriages of justice due to a lack of scientific verification in expert witness testimony. A method to examine the mechanisms of skeletal trauma, specifically skull fracture, in children would be beneficial in providing a solid biomechanical foundation to the forensic investigators in these child abuse cases.

This information is particularly needed for investigations of skull fracture in infants and toddlers younger than two years of age, whose fontanels and sutures have not closed completely. A large study, including 996 children under the age of two with fracture due to intentional injury, showed 27% of these children had skull fractures (Loder and Feinberg 2007). In another study of 904 intentional injury cases, approximately one third of all fractures were skull fractures (Merten, Radkowski et al. 1983). In a smaller study cohort of 54 pediatric head injury cases due to intentional injury, it was found that 56% suffered complex or linear skull fractures (Reece and Sege

2000). Other studies have examined both skull fracture and spreading of the sutures. Of 100 cases of intentional injury in infants, 22% showed evidence of skull fracture, but 42% showed suture spreading, with or without fracture (Kogutt, Swischuk et al. 1974).

Additionally, skull fractures from intentional injury are more likely to be fatal than accidental injuries, according to the results of Hobbs (Hobbs 1984). In this study of 89 children under the age of two with skull fracture, 19 of the 20 fatalities were cases of intentional injury, although this may be related to concomitant brain injury.

The forensic investigators lack the information required to associate specific skull fracture patterns to mechanical input and injury scenarios. In cases of intentional injury, some reported cranial fracture characteristics were more likely to include the following: (Hobbs 1984; Worlock, Stower et al. 1986; Meservy, Towbin et al. 1987; Leventhal, Thomas et al. 1993; Walker, Cook et al. 1997):

- Multiple or complex fractures with separation of bone fragments
- Bilateral fractures
- Depressed fractures
- Wide, long, or growing fractures
- Crossing of the suture lines
- Fracture of multiple cranial bones
- Fracture in occipital or temporal regions

However, one must understand that these fracture characteristics are not unique to cases of intentional injury, and abuse can be a factor even if none of these characteristics is present. For example, in the Reece and Sege (Reece and Sege 2000) study mentioned above, linear fractures were much more common than complex

fractures. In addition, the parietal bone is the most common fracture site in both intentional and non-intentional skull fracture (Hobbs 1984; Meservy, Towbin et al. 1987; Leventhal, Thomas et al. 1993).

The above conclusions were drawn from forensic case studies and anecdotal evidence. Well-controlled infant injury biomechanics studies are absent from the literature, leading to an unclear understanding of the injury mechanism. In order to fully investigate the impact event leading to skull fracture, computational modeling techniques can be beneficial. The method to be applied for this research, finite element modeling, allows for an anatomically-detailed geometry to be represented by discrete two-dimensional (2D) or three-dimensional (3D) shapes. The behavior of these discrete "elements" is governed by constitutive equations and strain energy functions, resulting in a prediction of the stress and strain profiles experienced by each element and the structure as a whole. Using this method, many well-controlled impact scenarios can be applied to identical models, eliminating anatomical variability and facilitating true comparison in resulting biomechanics. Another advantage of computational modeling is the ability to analyze several biomechanical outputs within the continuum, as opposed to experimental studies wherein global or isolated local measurements are taken. Using these numerical methods, a more complete picture of infant skull biomechanics is possible.

Specific Aims

As a preliminary step in the development of computational models that could be used to investigate pediatric skull fracture in the future, piglets have been identified as a

possible surrogate from which to generate data in the absence of human data. To this end, the following specific aims have been achieved:

1) Determine appropriate constitutive laws and material properties for the piglet skull and suture in more than one age group, including an appropriate failure criterion

2) Predict skull fracture patterns in a piglet model using finite element methods and replicate these patterns visually

3) Investigate the sensitivity of the computational models to changes in loading direction at a single impact point

Structure of the Dissertation

In Chapter 2, the biomechanics related to pediatric skull fracture will be discussed, particularly in how the infant head response to impact differs from that of the adult and the fracture mechanics thereof. Chapter 3 will introduce the piglet as a biomechanical surrogate for the infant skull; review the relevant literature related to pediatric material properties; and propose a novel technique for computational modeling of skull fracture in LS-DYNA, taking into account the morphological structure of the piglet braincase. Two finite element models representing piglet heads at two different ages (and levels of maturity) were developed. Validation of these models was performed against drop stand impacts performed at Michigan State University by comparing the fracture patterns and other biometrics. Age-specific piglet computational models developed in Chapter 3 are parametrically exercised in Chapter 4, employing robustness studies designed to determine model sensitivity to the failure criterion and to investigate the effects of slight variances in loading direction. Chapter 5 offers

discussion of the feasibility and validity of using these finite element modeling techniques as a forensic tool, as well as the current state of fracture modeling in LS-DYNA and recommendations for improvement.

CHAPTER 2

INFANT SKULL FRACTURE BIOMECHANICS

Infant Skull Anatomy

In the adult, the skull is comprised of 22 flattened, irregular bones, divided into cranial bones that encase the brain and facial bones which help facilitate sight, respiration, mastication, and other functions, as seen in Table 1 and Figure 1. These bones are joined by interdigitated sutures, which restrict movement between the bones (with the exception of the mandible).

Table 1 Classification of skull bones

Cranial	Paired	Temporal (bilateral)
		Parietal (bilateral)
	Unpaired	Occipital
		Frontal
		Sphenoid
		Ethmoid
Facial	Paired	Nasal
		Maxilla
		Lacrimal
		Zygoma
		Palatine
		Inferior nasal conchae
	Unpaired	Vomer
		Mandible
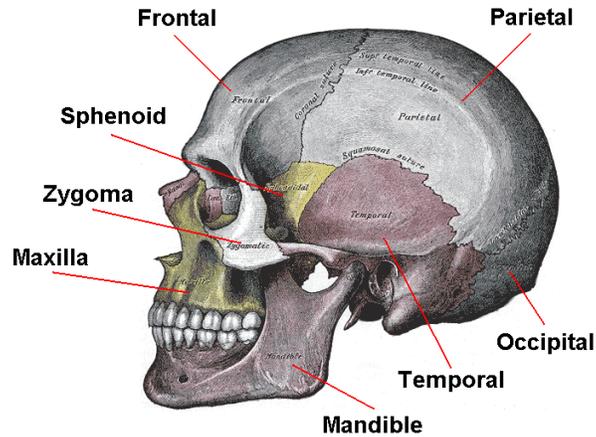
Figure 1 Bones of the skull taken from Gray, 1918

In the child, the skull differs from the mature skull in geometrical proportion, connectivity, and osteologic structure. The pediatric skull is disproportionately large at birth, and the face comprises only one-eighth of the area of the head compared to one-half in the adult. This is illustrated graphically in Figure 2. The frontal and parietal bones are prominent, leading to an additional geometric dissimilarity between the infant and the adult. Growth is slow from the seventh year onward, and it is at this point that the foramen magnum and orbits have reached approximately full size.
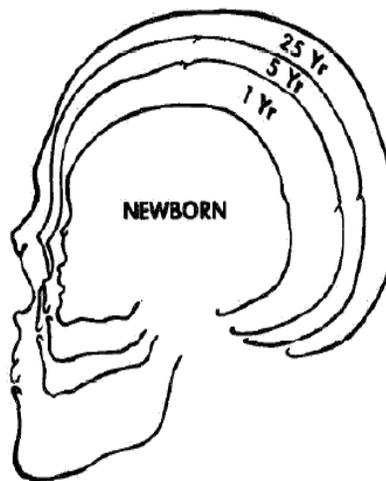
Figure 2 Growth of the skull taken from Burdi 1969

The bones of the infant skull are not tightly coupled as in the adult. Instead, the bones are loosely connected by fibrous tissue at the suture lines, as shown in Figure 3. In areas where more than one other bone comes together around the parietal bones, a "soft spot" called the fontanelle is formed in which a tough membrane lies between the scalp and the brain. There are six of these fontanelles in the newborn skull, which close at varying rates due to expansion and ossification of surrounding bone. The largest fontanelle, the anterior fontanelle, measures about 40 mm by 25 mm at birth and closes sometime before the second year.
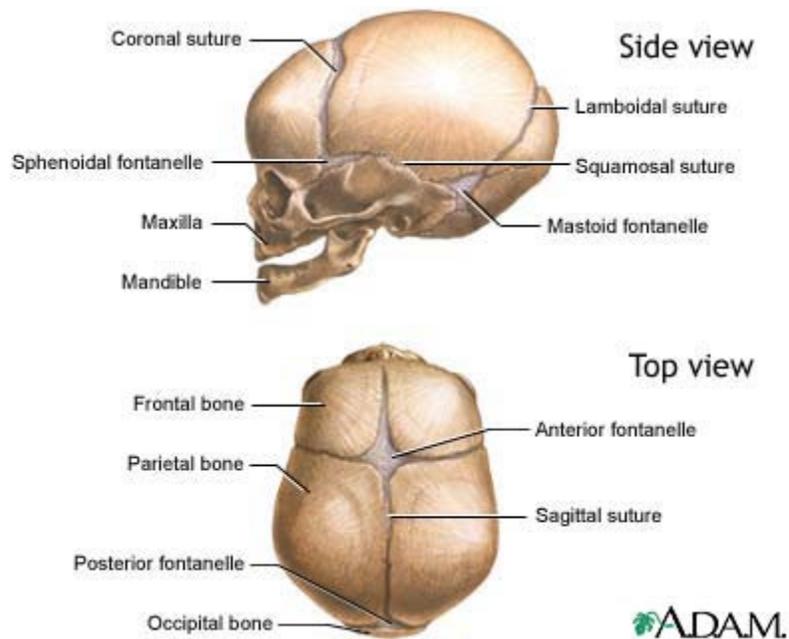
Figure 3 Fontanelles and sutures of the infant skull from
http://www.nlm.nih.gov/medlineplus/ency/imagepages/1127.htm

There are two types of growth that occur in the skull. *Surface growth* involves increasing bone thickness through ectocranial and endocranial bone deposition. This type of growth also encompasses development of the diploe layer. Adult skull bones have a three-layered sandwich structure consisting of the cortical lamina interna and

externa with a less dense intermediate diploe layer. According to Holck (Holck 2005), an infant's skull is made of lamellar layers, strengthening the thin bone plate. The three-layer composition does not begin to develop until the third year of age. *Marginal growth* involves ossification extending towards the periphery, expanding the area of the bone, and is facilitated by sutures and fontanelles. The growth of the brain causes outward displacement of the skull bones of the cranial vault, and the bone remodeling assists in the alteration of the skull plate curvature. This is illustrated schematically in Figure 4, with plus and minus signs showing bone resorption and deposition.
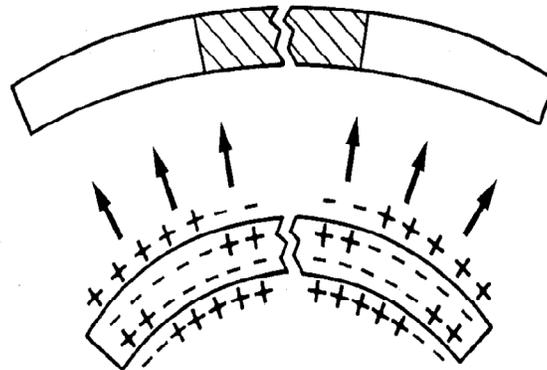
Figure 4 Growth in the infant skull taken from Cohen, 1993

The posterior fontanelle, the two sphenoidal fontanelles, and the two mastoid fontanelles close within six months to two years after birth (2-3 months is typical) (Hummel and Fortado 2005). The sutures "fuse" by two years of age (Hummel and Fortado 2005), but a small amount of fibrous tissue remains to facilitate future marginal growth (see Figure 5).
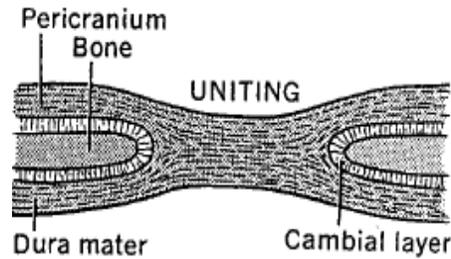
Figure 5 Suture morphology taken from Cohen, 1993

At birth, some of the skull bones may encompass more than one piece (e.g. occipital, frontal, temporal, sphenoid, and mandible). Ossification occurs gradually during the growth process at a variable rate dependent upon many factors, including location. For this study, the bones of interest are the parietal and occipital because these are the bones most affected by parietal impact, and their gross development will be discussed in further detail below.

An infant occiput is shown in Figure 6. In approximately the fourth year of life, the occipital squama and the two inferior lateral portions unite, and by the sixth year the bone consists of a single piece.
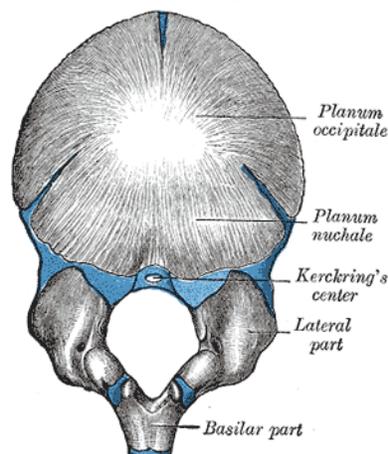
Figure 6 Gray's Anatomy infant occiput taken from Gray, 1918

In contrast, the parietal bone forms from a single ossification center and does not exhibit the fusion process necessary to unite partially ossified portions (Figure 7). Ossification extends radially from this point, leading to the periphery being less mature than that exhibited near the center (Gray 1918). The parietal bone is not circular, but displays angles at four corners, which are the last part to form, replacing the fontanels. (Note that there is a difference between ossification, the formation of bone tissue, and mineralization, the hardening of this tissue, both of which will affect material response. Bone tissue formation, described here, is followed by mineralization, in which the inorganic components are deposited and does not necessarily match the rate of ossification. This is relevant to tissue behavior and will be discussed further in Chapter 3.)
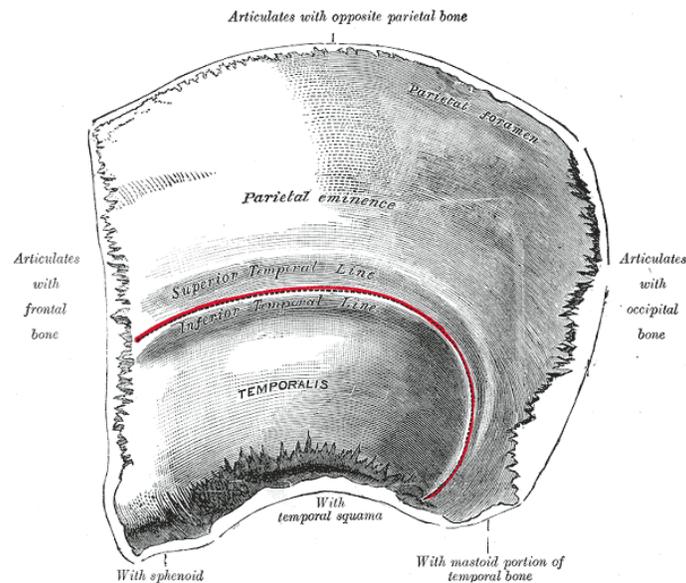
Figure 7 Gray's Anatomy infant left parietal taken from Gray, 1918

Infant Skull Biomechanics

Deformation due to impact

The infant skull is much more compliant than the adult skull, partially due to the level of bone development and partially due to the presence of unfused sutures and membranous fontanels. Mechanically, the bones of the infant skull form a segmented construction that can be considered a collection of loosely connected curved plates. As mentioned previously, infant bone plates differ from adult skull bones in that they do not have a fully developed sandwich structure, and a lower calcium content which could result in a material with brittle, nearly elastic behavior. It has been stated that impact to the infant skull causes significant elastic deformation and high strains (Ommaya, Goldsmith et al. 2002), but this has not been confirmed experimentally. Alternatively, it could be expected that impulsive loading would produce relatively little skull deformation, although pressure wave propagation through the brain may or may not be significant. It has been postulated by Ommaya and Goldsmith that the infant skull can resist compressive and shear loading, but is "incapable of transmitting bending" at the sutures. Although it is clear that the sutures play some role in skull deformation in the infant, the exact implications of this anatomical feature are not precisely known. The face, however, is relatively rigid when compared to the compliant infant braincase with unfused sutures and may have less effect on global deformation.

Experimental studies to elucidate the exact nature of infant skull deformation and confirm subjective observations of skull biomechanics in living children are limited. One group of researchers (Prange, Luck et al. 2004) has hypothesized that the intact infant

head demonstrates viscoelastic structural properties and performed nondestructive tests to study its biomechanical behavior.

Three specimens, which were composed of the head without the cervical spine, were harvested from cadavers aged one, three, and eleven days old. The mandible was removed, but the skin of the scalp remained undisturbed. For compression testing, the foramen magnum was blocked with gauze to ensure the intracranial contents remained in place during the experiment. The specimens were exposed to compression between two parallel plates at the anterior- and posterior-most or lateral-most of the head by a hydraulic actuator. A 0.5 N preload was applied to position the samples, but the maximum deformation for the entire experimental procedure was kept under 5% of the gauge length of the head to prevent failure. Before the tests were performed, preconditioning was conducted for 60 cycles at 1 Hz with a peak amplitude of 50% of the maximum displacement (as determined by individual gauge length). The specimens were tested at four loading rates, as seen in Figure 8, and in two directions (anterior-posterior and lateral right-left), and the force and deflection were recorded. The force-deflection curves showed an initial toe region; therefore, linear regression was used on the data from 50% to 100% maximum deflection to determine the stiffness. The stiffness was found to be significantly dependent ($p < 0.01$) on loading rate in that the quasi-static rate showed a lower stiffness than the other rates, which were not significantly different from one another. There was no statistical difference in terms of the direction of compression. Stiffness data are shown in Figure 8, and a dependence on loading rate indicated a viscoelastic response according to the authors, which was confirmed through impact testing (described below) and analytical modeling (Figure 9).
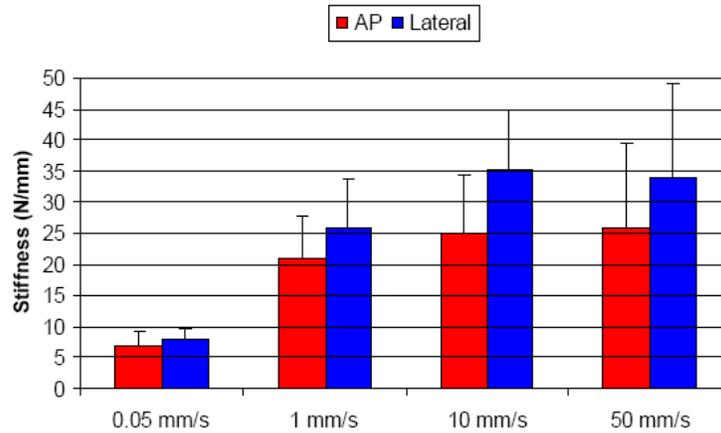
Figure 8 Intact infant head stiffness in two directions from Prange's data
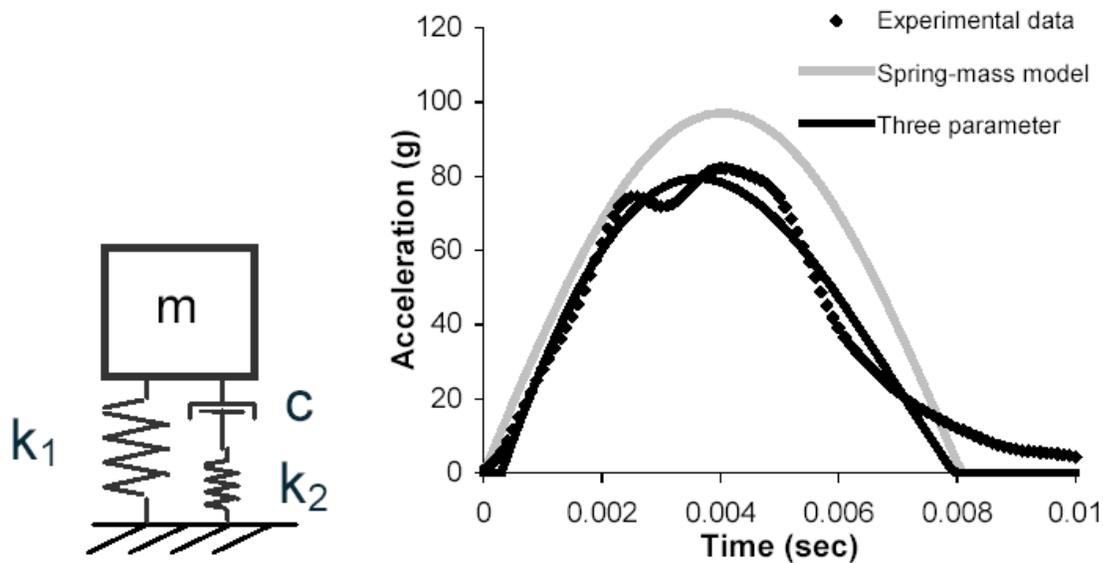
Figure 9 Prange's analytical model results for a 15-cm drop

The specimens in this study were also tested in impact. Before this part of the experimental protocol was performed, any void areas of the head were filled with water, and the foramen magnum was sealed with polymethylmethacrylate. The specimen was held at a certain drop height and orientation, and released by burning through the suspending string in order to limit initial translation or rotation. The drop heights were

estimated to be 15 or 30 cm, as measured by a ruler. The orientations were chosen so that the impacts occurred in five locations: vertex, occiput, forehead, right parietal, and left parietal. Therefore, each specimen underwent ten nondestructive drops. The resulting peak accelerations can be seen in Figure 10. The peak acceleration was not significantly affected by impact location. Figure 11 demonstrates a typical time history for the drop tests, and shows that the shape of the curve can appear different for different conditions, but this was not statistically significant across the tests. Acceleration pulse durations were similar for the two drop heights, as calculated by dividing force plate data by head mass.
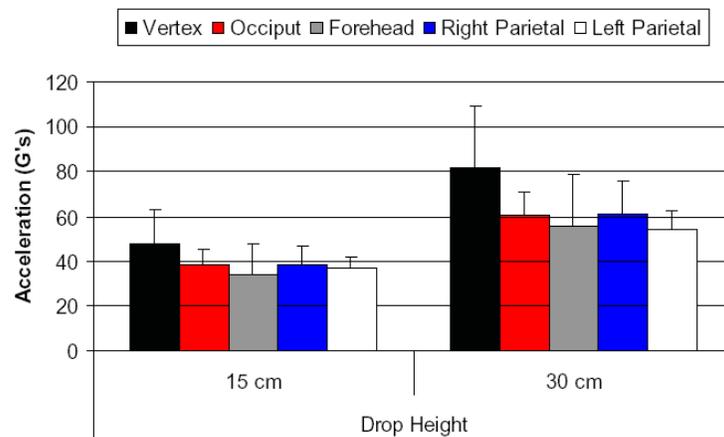
Figure 10 Peak accelerations for dropped intact infant heads
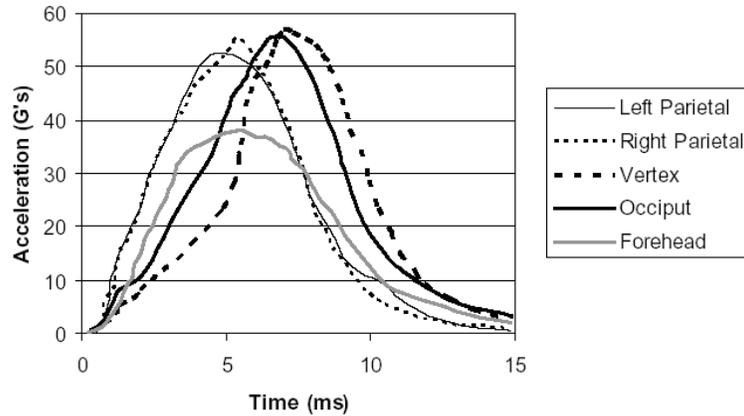
Figure 11 Acceleration time histories for 30-cm drop

Biomechanics of skull fracture

Skull fracture in the adult skull has been studied by many researchers, and failure stresses and strains reported. According to a review conducted by Ommaya et al. (Ommaya, Goldsmith et al. 2002), the adult skull fractures at tensile strains of 2%, and the diploe can be crushed under radial loading. Ommaya's review also indicated that adult resistance to skull fracture is eleven times greater than newborns based on failure stress, but it was unclear from where these data were obtained.

Fracture patterns in the adult skull have been described as well. Yoganandan et al. (Yoganandan, Pintar et al. 1995) reported complex fracture patterns, dependent on impact location. Fracture widths were narrower at the impact location, echoing results obtained by Gurdjian using the stress-coat technique (Gurdjian and Lissner 1945). A review of temporoparietal skull fracture by Yoganandan and Pintar (Yoganandan and Pintar 2004) indicated that the parietal bone fractured in a similar manner to the frontal and occipital bones, due to their similar material construction. However, it was noted

that the tolerances are generally slightly lower for lateral impact. This may be due to anatomical considerations.

Information on fracture of the infant skull is generally obtained from pathologists or forensic anthropologists in case reports. It has been observed that fracture lines in the infant skull follow along the spiculae emanating from centers of ossification (Holck 2005). Little data have been compiled about infant skull fracture trends beyond the common observations with child abuse outlined in Chapter 1. The role of the sutures in infant skull fracture is still unclear.

To the best of the author's knowledge, few researchers (Weber 1984; Weber 1985; Holck 2005) have studied skull fracture experimentally using infant cadaveric specimens. These studies involved infant subjects up to 9 months old who died of pathological causes and were checked for previous fractures. In the first study, the subjects were dropped from 82 cm onto three hard surfaces: stone (n=5), thin carpet (n=5), and linoleum (n=5). The second study involved a similar protocol, but two softer impact surfaces were utilized: 2-cm thick rubber mat (n=10) and 8-cm folded blanket (n=25). Although no details were provided for the drop method beyond the original position being a horizontal orientation, the impacts were described as parieto-occipital impacts. It is not clear from the publication or the results if a consistent impact side was used. Autopsies were performed to examine the subjects for fracture, and the fracture patterns sketched, as shown in Figure 12 and Figure 13. The subject-specific age, gender, head circumference and weight are given in the figures.
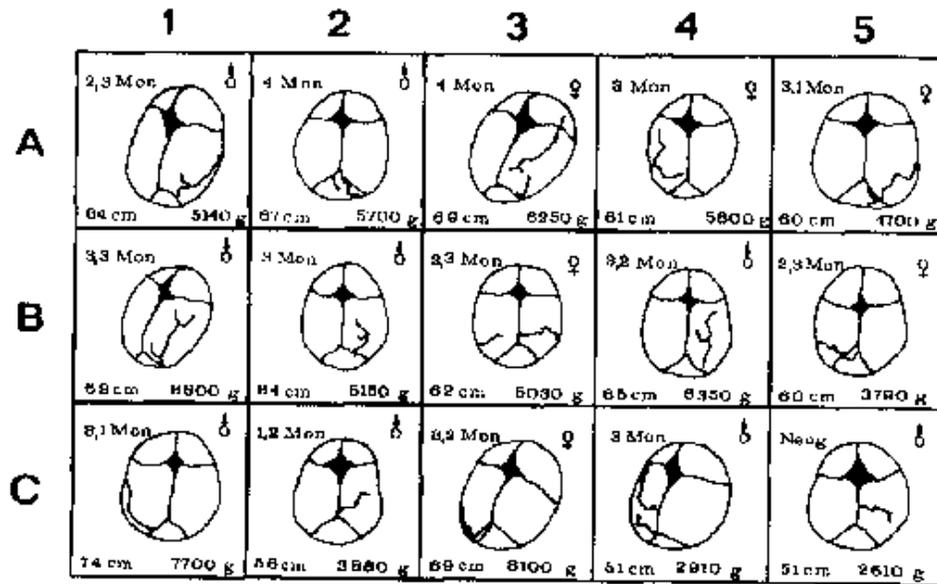
Figure 12 Skull fracture patterns from 82-cm drops with parieto-occiptal impact onto three hard surfaces: (A) stone, (B) carpet, (C) linoleum taken from Weber 1984
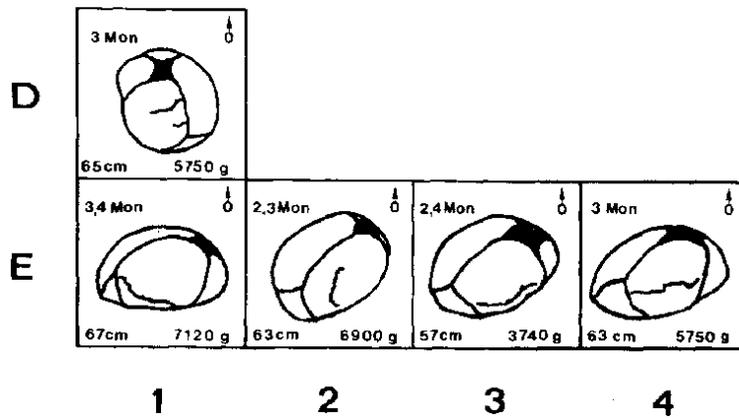
Figure 13 Skull fracture patterns from 82-cm drops with parieto-occipital impact onto two softer surfaces: (D) mat, (E) blanket taken from Weber 1985

For impacts onto hard surfaces, all subjects sustained linear fractures, and in three subjects, the fracture lines crossed sutures. For impacts onto soft surfaces, most subjects did not sustain fracture. Only one of ten subjects fractured on the rubber mat, and four of twenty-five on the blanket. The fractures seen were similar to the first study,

but none crossed a suture line. For the impacts onto softer surfaces, bone thickness around the fracture site was measured and bone translucency observed. A relevant finding was that the fractures occurred along lines of bone translucency, where the bone was 0.1-0.4 mm in thickness. These studies seemed to indicate that the likelihood of fracture or likelihood of the fracture to cross the suture line was not dictated by age or impact energy, within these small ranges, and the crack initiation point remains unknown.

Although experimental studies are rare, recent advances in computational technology have allowed researchers to make some observations on infant skull deformation and fracture biomechanics. These models, while impossible to fully validate due to a lack of experimental data, can provide insight into the biomechanics on at least a qualitative level.

Infant Head Finite Element Models

Several finite element models developed to study infant skull or brain biomechanics have been published in the literature. A majority of these are impact models, although there are also some models used to study fetal head molding during birth. Key parameters of the impact models are listed in Appendix 1, and the published details of each model and results are described below.

Idealized 3-month-old: skull deformation

To study the deformations of the immature skull, Kurtz et al (1998) created an idealized partial infant head model representing a 3-month-old. Bone was modeled using shell elements, but the sutures were modeled as linear springs, supporting tension and not bending. The idealized brain included a separate dura (shells) and

continuum cerebral spinal fluid (CSF)/brain (solids). Frictionless contact was used at the skull-dura interface. The authors modeled the bone using an isotropic, deviatoric rate-independent elastic-plastic model with a von Mises yield criterion, allowing compressibility during elastic deformations but no volume change during plastic deformations. The brain was modeled as a linear viscoelastic solid. Material properties for the bone and suture were derived from a single 3-month-old subject (Runge, Youssef et al. 1998). Elastic properties of the dura and foramen magnum were chosen to be comparatively small to account for the mechanical impedance of the spinal cord. A flat impactor was modeled to simulate lateral and posterior impacts of 1 kN at 45 degrees. The lateral load produced plastic deformations of the parietal region and strains up to 7%. The occipital impact predicted strains of 12.6%, which is higher than the maximum effective strain for infant bone, according to the material property study.

Idealized 1-month-old infant and adult: influence of skull material on brain response

Another simplified model was created by Margulies and Thibault (Margulies and Thibault 2000) to compare biomechanical response using infant and adult material properties of the skull and suture. The adult model had an elastic modulus of 10 GPa, while the infant model had moduli of 1.3 GPa for bone and 200 MPa for suture. A homogenous brain mass was included, but the brain tissue properties were not varied between the adult and infant. A half-sine load of 10 ms duration was applied to the parietal region at a 45-degree angle using a flat impactor at 1000 and 5000 N amplitudes, as shown in Figure 14. Skull deformations and the accompanying intracranial strains affecting the brain were noticeably affected by the change in elastic modulus from adult to infant. Peak intrusion was more than double for the infant as

compared to the adult, and the response of the brain showed diffuse bilateral strain distribution in the infant and focal unilateral distribution in the adult. This indicates that impacts causing focal brain injuries in adults possibly yield diffuse injuries in children, due to the more compliant braincase.
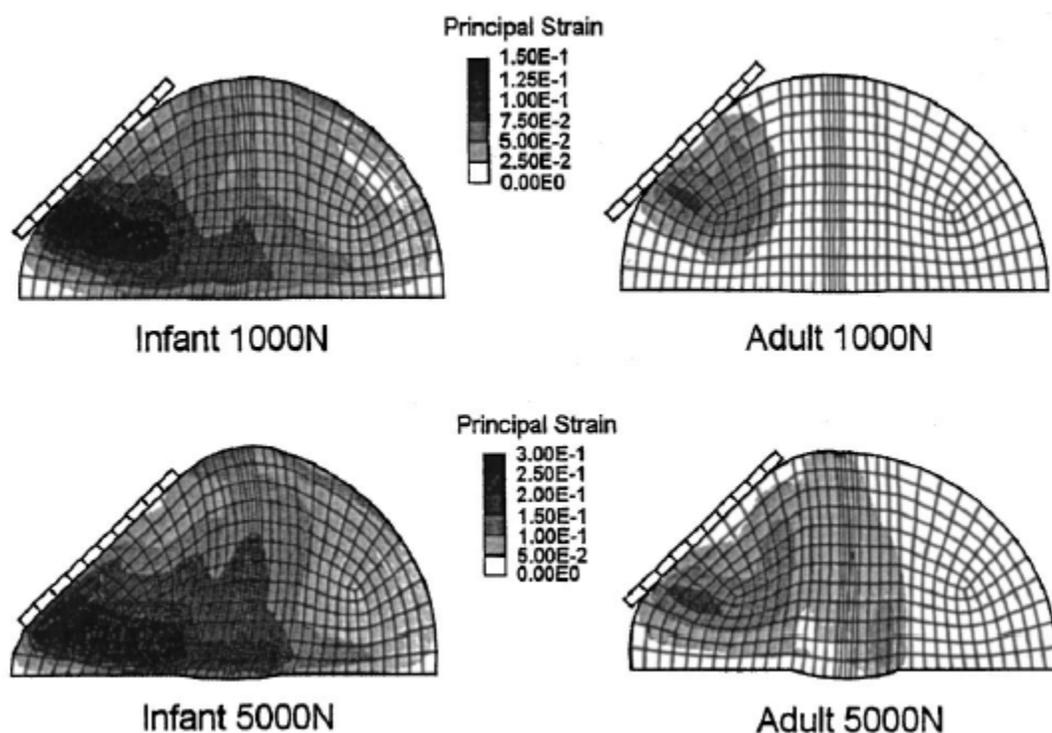
Figure 14 Strain distributions in adult and infant braincase models-boundary conditions were not published, but reported to be the same for each model (Image: Margulies and Thibault, 2000)

Detailed 6-month-old: comparison with CRABI dummy

Klinich et al. (Desantis Klinich, Hulbert et al. 2002) created an infant head model to study automotive impact and compare results with those obtained from a 6-month-old Child Restraint Air Bag Interaction (CRABI) dummy. The geometry for this model was based on manual processing of the CT scan of a 27-week-old subject. The skull and sutures were modeled using thick shells, and the average skull thickness measured

from each CT slice (no orientation stated) was used to determine the inner skull surface contour. Other components, including a homogeneous brain, were composed of solid elements. The elements of the skull were projected 0.5 mm inward to create a dural layer, and a second projection created the 1.5-mm CSF layer, with solid elements occupying the remainder of the cranial cavity to represent the brain. The face is modeled as rigid, using geometry from the Zygote infant model (Zygote Media Group, Inc., Linden, Utah). Immature porcine data (Thibault and Margulies 1998; Margulies and Thibault 2000) were used for material properties whenever possible. A series of parametric studies was performed to quantify the effects of using adult and/or estimated properties for the brain, CSF, dura, and scalp, and the effects were found to be minimal on the magnitude and pattern of stress distributions. Decreasing the bulk modulus of the brain increased the predicted stresses by more than 15% and increased head acceleration. Increasing the long-term shear modulus (G_∞) of the brain or Young's modulus (E) of the skull also increased head acceleration. The suture stiffness, however, did not have a significant effect on stress distributions.

Loading was applied using a rigid, flat impactor with a velocity equal to that measured on the child restraint system (CRS) during CRABI tests replicating real-world crashes. Symmetric loading to the back of head, which approximates real-world loading conditions during frontal impact, was used as an initial input. The results indicated high stresses in the occiput. Off-center loading conditions, representing three real-world cases, were then modeled. In automotive accidents, parietal fractures can be seen, and it was hypothesized that loading to the occiput caused outbending of the parietal bone plates, resulting in fracture. However, areas of highest stress occurred at the occiput,

and it was suggested that the most severe fracture would occur at the site of loading, while other remote fractures were possible. Logistic regression was performed to estimate tolerance values from the model and the injuries from the real-world cases (Figure 15). Drop tests were also simulated for comparison of acceleration time histories and deformation with experimental data using the CRABI dummy as the test subject. In this comparison, it was seen that the model predicted shorter duration, greater acceleration impacts for the same test conditions. However, the deformations predicted by the infant head model were smaller than those measured from the dummy model.
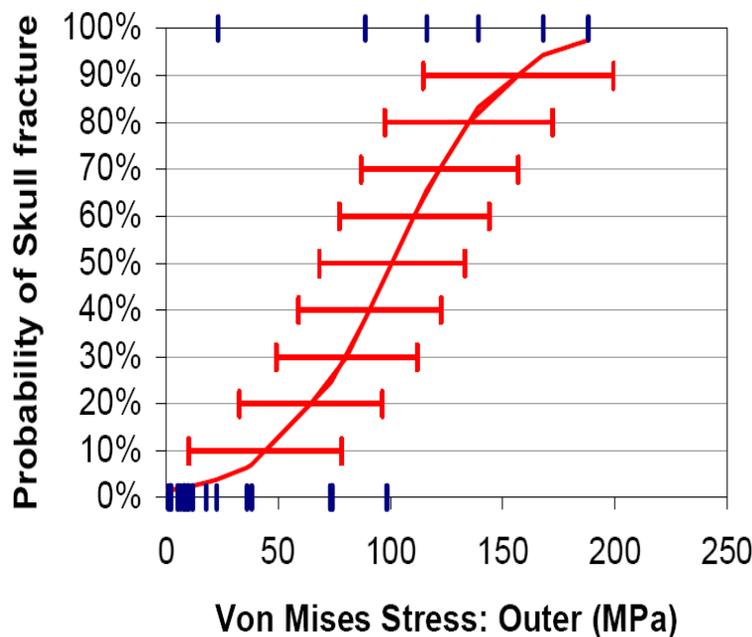
Figure 15 Probability of skull fracture predicted by the Klinich model (Image: DeSantis Klinich et al., 2002)

Detailed 6-month-old: investigation of SBS and comparison with scaled model

Roth et al. (2007) created a complete head model from CT data of a 6-month-old child to study Shaken Baby Syndrome (SBS). This model is the most detailed of all

currently published infant head models, including anatomical structures such as the skull, sutures and fontanelles, the scalp, and a layer of CSF between the skull and brain. The brain was not an idealized homogenous model (like many of the other pediatric head impact models), including structures such as the tentorium, falx, cerebrum, and cerebellum. The skull, sutures, fontanelles, falx, and tentorium were modeled using shell elements, while the cerebrum, cerebellum, CSF, and scalp were modeled with brick elements. Springs were added to represent the bridging veins, which may be of importance in SBS. The constitutive laws and material properties are listed in Appendix 1.

Both shaking and an impact to the occiput were simulated. The shaking pulse was a 400 ms sinusoid at 30 rad/s, for one cycle duration. Relative displacement in the sagittal plane was used to evaluate bridging vein strain during shaking. The impact was modeled using a 3 m/s initial velocity onto a rigid wall. The results showed that brain pressure and shear stress were lower during shaking than during impact, but bridging vein strain was equal for both cases. However, the maximum strain was reached late in the shaking event compared with immediately upon impact. Although no validation study was published for this model, the peak strain predicted for bridging vein strain was not dependent on loading mode and agreed with model predictions reported by other researchers (Lee and Haut 1989), according to the authors.

In a different publication in 2008, Roth et al. compared this infant head finite element model (Roth, Raul et al. 2007) directly to a geometrically scaled adult head model with infant material properties. The scale factor used was 0.775 in all directions, and the mass of the scaled model was 2.1 kg compared with 2.2 kg for the infant model.

Differences in inertial values were most prominent in the x-axis (anterior-posterior plane). Frontal, lateral, and occipital impacts against a rigid wall at 1 m/s were simulated. Comparisons between the scaled adult model and the infant model showed differing pressure and stress distributions and time histories for all cases, but it should be noted that the mesh densities were dissimilar, which would affect the model results. "Fracture prediction" from stress criteria resulted in differing locations for each simulation, with the child model predicting the more realistic crack pattern, based on one real-world case shown in Figure 16.
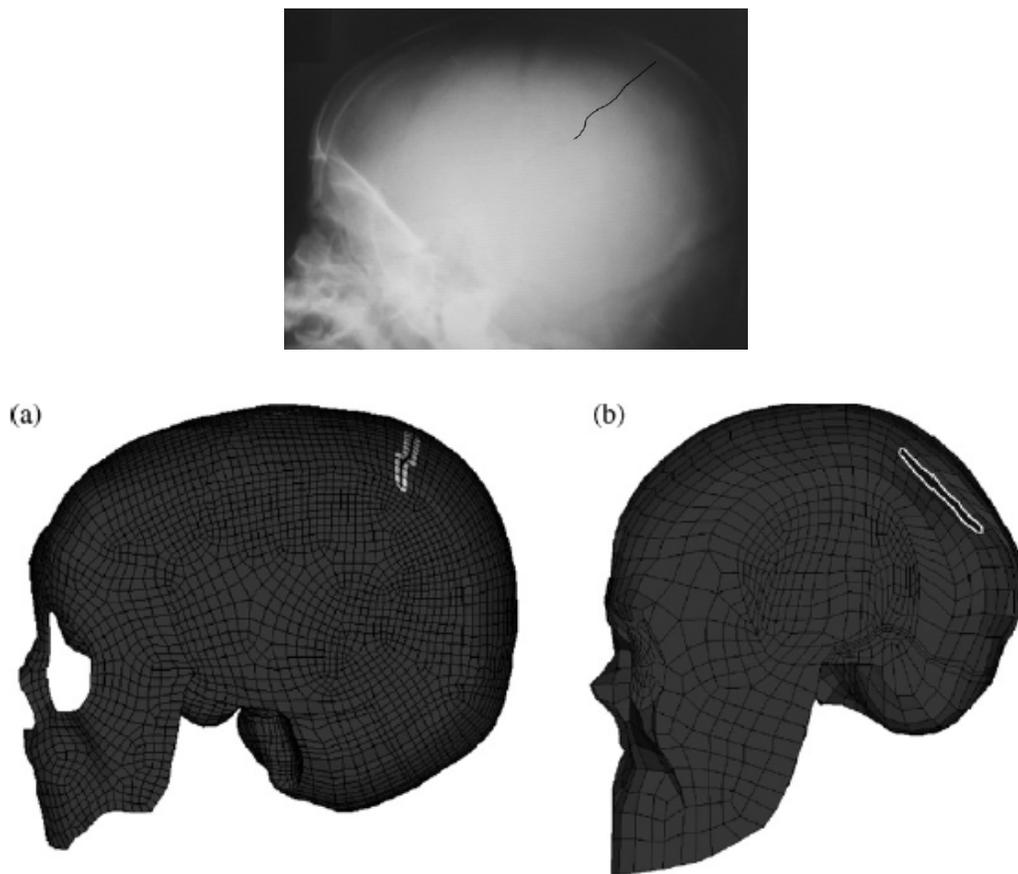
Figure 16 Fracture prediction from a real-world case (upper), showing better agreement with the infant model (lower, a) than with the scaled adult model (lower, b) (Image: Roth et al., 2007)

Detailed 6-week-old infant: skull biomechanics

Another detailed infant head model by Coats et al. (Coats, Margulies et al. 2007) was published in 2007. The geometry for this model was based on MRI and CT images of a 5-week-old, which were used to create closed boundary contours for the outer skull surface. The thickness of each skull plate was measured from CT, and the outer surface projected inward accordingly to create internal cranial structures. It is not clear whether each skull plate had a uniform thickness or if regional thickness variance was applied throughout each individual bone, although the skull was modeled using shell elements. The brain was modeled as homogenous and isotropic, since the model was developed with the intent of investigating skull injury. A scalp was created using solid elements with a thickness of 3.5 mm, a value found in the literature.

The material properties for this model were based mostly on experimental studies performed on piglets and humans. For the skull, the parietal bone was found to be stiffer than the occiput and was modeled accordingly. Based on the findings of McPherson and Kriewall (1980), a ratio of 4:1 was used to find the elastic modulus in the direction parallel to the bone fiber orientation, allowing for an orthotropic constitutive model to be employed. Frictional contact was used, with the suture represented by membrane elements, the nodes of which were tied to the skull element nodes. The foramen magnum was left open and allowed brain motion through its boundary.

A series of parametric studies was performed to investigate the effects of changing five parameters (brain stiffness, brain compressibility, suture thickness, suture width, and scalp inclusion) at two or three levels. Note that the levels did not correspond to normal anatomic ranges. The model used in the parametric studies

simulated a fall from a height of 0.3 m with the occiput impacting a rigid surface. For input, an initial velocity was calculated as 2.44 m/s using energy conservation, and the model outputs examined were peak contact force, contact duration, peak principal stress, and maximum contact area. The parametric study results showed that increasing brain stiffness or altering brain compressibility had an effect on peak stress and contact force parameters, as well as an effect on contact duration when compressibility was changed. Although suture thickness did not affect the results significantly, abnormally large suture width did affect peak principal stress in the skull, peak contact force, and contact duration. The authors note that this indicates a need for prudence when assigning brain properties, even for a skull fracture model. Eliminating the sutures entirely by assigning bone properties to suture elements did not significantly affect the maximum stress in the parietal region.

Validation for this model was attempted by simulating of Weber's infant cadaver study (Weber 1984). As mentioned previously, Weber dropped infant cadavers from a height of 82 cm onto different rigid surfaces, and observed the fracture lines. Coat's model, when given this input, predicted high stresses in the parietal-lambdoidal suture region where some of Weber's fractures occurred, but the length of the fracture was not considered. It is unclear as to how the impact orientation was determined for each case. As Weber's study did not provide quantitative data for validation, this must be considered a subjective validation. Validation of the braincase material properties was performed quantitatively through modeling of 3-point bending tests reported by the same authors.

The model was used to investigate fracture tolerance, based on material failure values found in the material property study. Fracture in the model was assigned through a 3x3 element array calculation of average stress to avoid localized peak values in an isolated element. Fracture was assumed to occur when the computed stress in those arrays exceeded the ultimate stress obtained from material failure tests using 0.5- to 2.5-month-old subjects. The mean ultimate stress values of 9.4 MPa for occipital and 27 MPa for parietal bones were considered to be a 50% risk of fracture (Figure 17). The left parietal bone had higher fracture risk because of natural anatomic convexity in the region of the parietal-occiptial impact simulated to emulate the Weber experiments. However, the model does not predict severity or type of fracture, as crack propagation algorithms are not included.
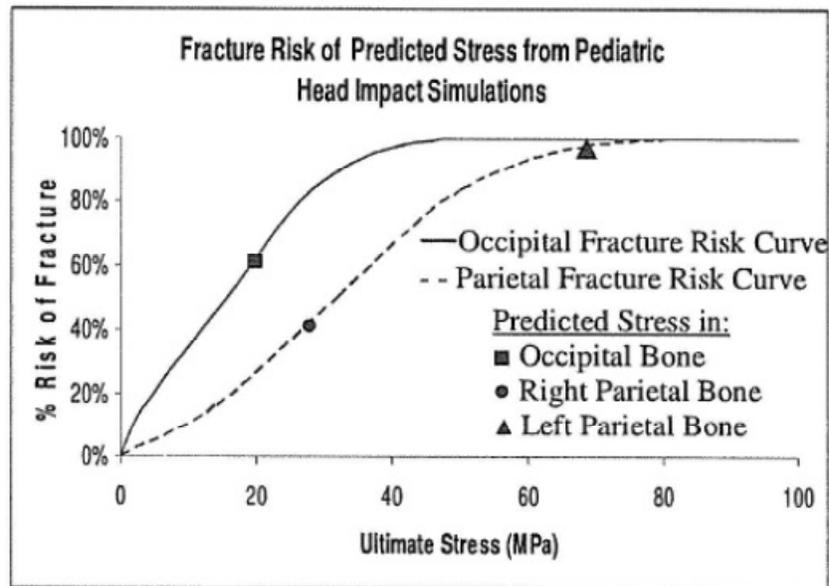
Figure 17 Probability of fracture predicted by the Coats model (Image: Coats et al., 2007)

Older pediatric model: skull biomechanics

A model focusing on craniofacial impact has also been developed (Zhang, Hou et al. 2007). CT scan images of a 7-year-old female were used to model frontal impact to the zygoma and to elucidate the role of the craniofacial sutures in pediatric facial injury biomechanics. The model predicted that the immature sutures acted to reduce stress transmission into the deep layer of the skull. However, the large stress gradient observed in the craniofacial sutures also made them vulnerable to injury due to high shear and tensile stresses.

Simplified newborn parietal bone: birth deformation

McPherson and Kriewall (McPherson and Kriewall 1980) used rudimentary finite element techniques to study fetal head molding during birth. In this process, the parietal bone undergoes most of the deformation, and a quantitative understanding of biomechanics of fetal molding was desired. Given that this model was developed nearly thirty years ago, it is expectedly limited by finite element and computing technology of the time, but the small strains and stresses justify the use of finite element theory, even at this elementary stage in its development.

The geometry for this model was taken from three orthogonal radiographs, and using orthographic projection, a rough 3D model of the left parietal bone was constructed (Figure 18). This model included 63 thin shell elements, with nodes chosen from anatomically relevant landmark points. The radial mesh mirrors radial bone fibers seen in fetal parietal bone, and bone thickness decreased in three concentric rings from eminence to margins (element thickness = 0.89, 0.74, and 0.61 mm). Boundary conditions attempted to eliminate possibility of overlapping parietal plates (i.e., the bone margins could not cross at the sagittal suture), as this does not occur during birth.

Material properties for the tangential modulus, E_1 = 3860 MPa, and the radial modulus, E_2 = 965 MPa, were taken from a previous study. Because the material was considered orthotropic but thin, plane stress was assumed, yielding ν_{12} = 0.08 calculated from orthotropic constitutive equations and a reported adult value of ν_{21} = 0.28. The loading profile was based on pressure transducer data during birth. Results showed bone deformation, as opposed to rigid body motion, with strains from -0.0133 to 0.01 at 50% dilation. The maximum membrane stress was predicted to be less than 5.5 MPa and bending stress less than 0.1 MPa. Validation was subjective, using kinematic trends, and the boundary conditions were not chosen properly, so parietal overlapping did occur during simulation.
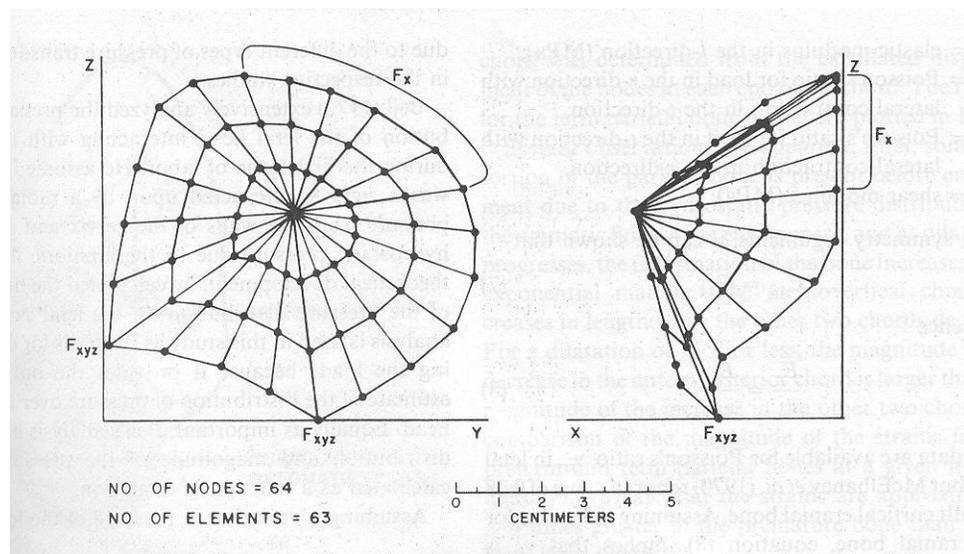

Figure 18 McPherson and Kriewall's infant parietal bone model (Image: McPherson and Kriewall, 1980)

Detailed newborn: skull biomechanics during birth

Lapeer and Prager used a static model to investigate pressure distribution on the fetal skull during the first stage of labor (Lapeer and Prager 2001). Geometry for this

model was obtained through laser scanning of an infant skull replica, although an earlier paper by the same authors showed a method for creating 3D geometry of the infant skull using a master and slave warping technique (Lapeer and Prager 2000). The resulting nonlinear model was meshed with 63,413 first-order triangular shell elements (Figure 19). Variable skull thickness was employed, using the same values and contours as McPherson and Kriewall, with 2 mm at the skull base and maxilla and 0.57 mm for suture and fontanelle. A slightly modified version of McPherson and Kriewall's material behavior profile was used, in which the Poisson's ratio was defined as 0.22, leading to slightly different parameter values in the in-plane orthotropic constitutive model. The suture material was based on fetal dura mater properties (Bylski, Kriewall et al. 1986): homogenous, isotropic, non-linear elastic, and incompressible hyperelastic. The Mooney Rivlin constitutive model was used with constants of c_1 = 1.18 MPa and c_2 = 0.295 MPa. Anisotropic and viscoelastic behavior was ignored, based on the findings of Melvin et al. (1970) that anatomical variation overshadows these effects. Adult properties were assumed for the skull base and maxilla.

Static radial pressures were applied based on measured normal birth pressures. The base of the skull and some facial nodes were constrained to prevent rigid body translation and rotation. Diametral strains of -2.84% to 1.63% compared favorably to published clinical experiments and global deformation shape was considered reasonable.
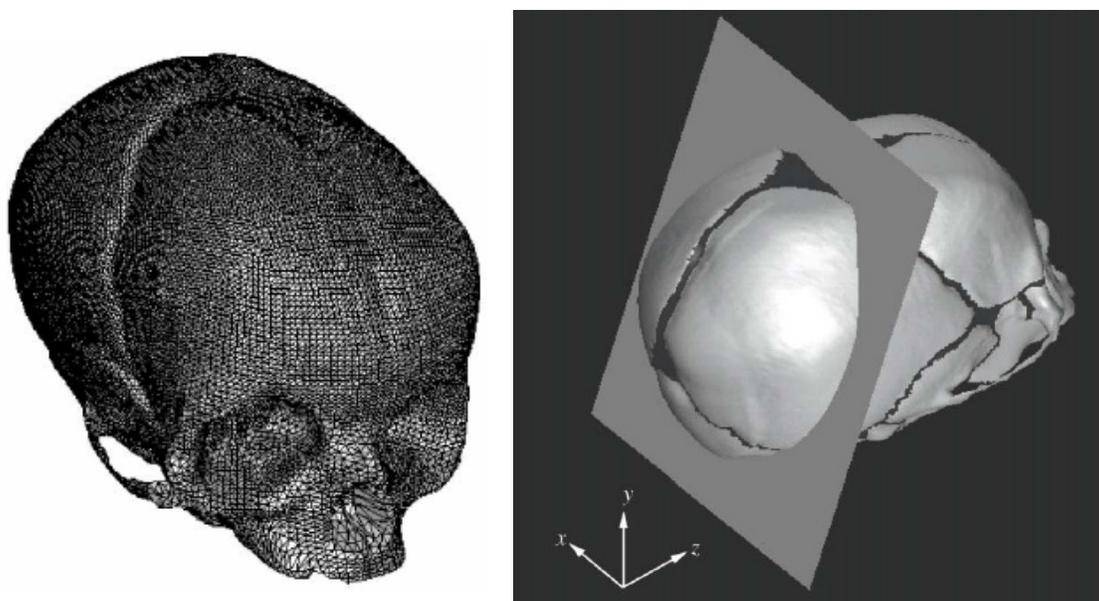
Figure 19 Lapeer's birth model (Image: Lapeer and Prager, 2001)

Summary

Infant skull biomechanics and, in particular, the influence of sutures on skull fracture, is not clearly understood. Although the infant head is undeniably more compliant than the adult head, due to the nature of the birth process, the role of this compliance and possible viscoelastic response warrants further study in regard to impact biomechanics. It has been postulated that outbending plays a significant role in infant skull fracture, although this has not been confirmed with physical experiments. Skull fracture patterns have rarely been investigated experimentally to elucidate further information on the biomechanics of fracture, and the fracture locations relative to the impact location are unknown, as are fracture initiation and termination locations. Through experimental analysis, it has been seen that fracture lines occur in areas of high transparency. Additional anecdotal evidence suggests that fracture lines follow the bony spiculae radiating from ossification centers of the infant skull bone plates, although

much more work is needed to confirm this experimentally. The scarcity of pediatric post-mortem subjects remains an obstacle to this field of research.

Although finite element models of the infant head have been developed, validation is difficult without controlled biomechanical studies. Disregarding the level of validation, analysis of skull fracture has been limited to stress tolerance criteria, and no attempts have been made to account for crack propagation or non-uniform skull thickness. Material models used in these models simplify the mechanics of the biological material behavior (e.g., using a linear material model to represent nonlinear behavior), and a complete dataset of material properties at any given age, much less throughout the stages of development, is not currently available. Further finite element models should incorporate some consideration for bone morphology and more accurate material models, as well as crack propagation algorithms.

CHAPTER 3

THEORY AND DEVELOPMENT OF PIGLET HEAD SURROGATE MODELS

Objective

The objective of this chapter is to develop a piglet surrogate model for use in predicting patterns of pediatric skull fracture. The literature will be reviewed to justify the use of a piglet surrogate, and to compare experimentally determined human infant material properties and biomechanical response with those found using the piglet surrogate. Mechanical factors, such as rate dependence and viscoelastic behavior, will be discussed in the selection of an appropriate constitutive model for the skull bones. The development of the finite element model will be outlined and preliminary, pre-validation results presented.

Review of the Literature

Pigs as surrogates

The piglet has long been used as an experimental surrogate for pediatric studies due to similar material properties and internal organ position (Prasad and Daniel 1984; Aerssens, Boonen et al. 1998; Kent, Stacey et al. 2006). In the case of the current study, piglets were chosen as a surrogate based on cranial vault shape and material property compatibility. In addition, the pig has been used to study brain injury because of similarities on the tissue level (Meaney 1995).

Dobbing (1964) proposed an age equivalence between human and pig based on chemical factors in brain development, suggesting one week of porcine life is equal to one month of human life. This has commonly been used for young children only, and it is not clear where the correlation dies off. In a study of pediatric brain material

properties, Thibault and Margulies (1998) used 2- to 3-day-old piglets to represent infants under one month of age and 1-month-old piglets to represent 4-year-old toddlers. However, an age-dependent brain property study by Prange et al. (1999) indicated that a one-year-old pig (which would be equivalent to a four-year-old child according to Dobbing's criterion) had brain properties very similar to that of an adult human. If Dobbing's equivalence is accurate for infants, it is clear that the relationship between porcine age and human age is nonlinear and should be used with caution.

For equivalence on a skeletal development basis, no historical literature explored the relationship. Margulies and Thibault (2000) found that the elastic and rupture moduli for a limited sample size of 2-3 day old piglet skull samples was consistent with human samples from birth to 6 months. A newer study by Baumer suggested that, based on piglet parietal bone bending data, 1 day in the piglet correlates with 1 month in the human for ages up to 10 months. However, neither of those studies evaluated structural morphological similarities, which can strongly affect the overall biomechanics of the skull. Further research is needed before an age equivalency can be proposed with any degree of confidence. At this time, while the piglet can be considered an appropriate surrogate for child head injury, translating the findings of such studies directly to the human should be done with caution. Instead trends seen in piglet studies can guide future studies of pediatric cadavers so that state-of-the-art computational models can be developed for each more complex research.

Experimentally-determined pediatric skull and suture material properties

In order to fully evaluate the biofidelity of piglets as an infant surrogate, it is paramount to understand the material behavior of the tissues in addition to the global

biomechanical response. Comparison of human data to piglet data can help to determine whether a direct age correlation is appropriate, or to begin to develop more realistic scaling laws that take into account developmental, as well as geometric changes that occur with age. This is currently a deficiency in adult to child scaling, due to the incomplete dataset available in the literature for children. Piglet, or other animal, surrogates can help fill this gap, although that is beyond the scope of this dissertation.

Human infant skull and suture material properties – A thorough review of pediatric material property experiments, conducted on human samples or animal surrogates, examined the critical shortages of such data evident in the literature (Franklyn et al. 2007). Kriewall et al. (1981) measured the ash content of fetal cranial bone in order to determine if the positive correlation found between elastic modulus and ash content in adult bone (Mather 1968; Currey 1969) was valid for infant bone. Their results showed a large spread in ash content data, reflecting the dynamic nature of mineralization and ossification in the developing fetus. Although a positive correlation was seen, a linear estimation yielded an r value of only 0.56. However, when examining the correlation between age and ash content, an r value of 0.82 was calculated. Kriewall et al. concluded that, for pediatric specimens, structural development is more likely to account for an increase in elastic modulus than ash content.

Figure 20 and Table 2 summarize the results from the infant skull bone studies, and a detailed description of each experiment can be found in the Franklyn et al. (2007) publication.
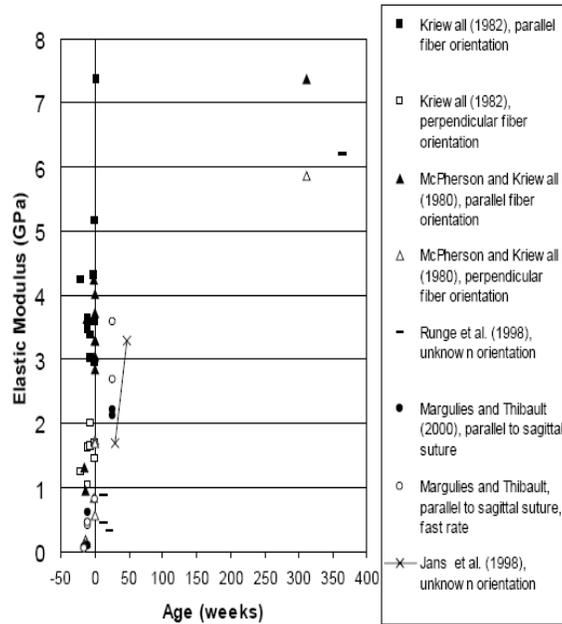
Figure 20 Graphical summary of infant elastic moduli, as reported in literature

Table 2 Summary of infant skull material property experiments

| Reference	Specimen Age	Test Type and Rate	Bone Sample	Sample Orientation	
(McPherson and Kriewall 1980)	24-40 weeks gestation	3-point bending 0.5 mm/min	Frontal and parietal	Parallel and perpendicular	Pre-term -> E = 1650 MPa (parallel), 145 MPa (perp.) Term -> E = 3880 MPa (parallel), 951 MPa (perp.)
(Kriewall, McPherson et al. 1981)	24-42 weeks gestation	3-point bending 0.5 mm/min	Frontal and parietal	Parallel	E = 3103 MPa (μ = 656)
(Kriewall 1982)	20-42 weeks gestation	3-point bending 0.5 mm/min	Parietal	Parallel and perpendicular	
(Runge, Youssef et al. 1998)*	3-15 months	3-point bending 18-1800 mm/min	Parietal and occipital	Unknown	E= 880 MPa, E = 47 MPa, σ_{yield} = 12 MPa, σ_{ult} = 18.5 MPa, ε_{ult} = 0.126
(Margulies and Thibault 2000)**	25 weeks gestation to 1 week	3-point bending 2.54 mm/min	Parietal	Perpendicular	E = 434.46 MPa, σ_{ult} = 10.34 MPa, U_0 = 0.0620 N/mm
		3-point bending 2540 mm/min	Parietal	Perpendicular	E = 261.9 MPa, σ_{ult} = 7.5 MPa, U_0 = 0.0031 N/mm
	6 months	3-point bending 2.54 mm/min	Parietal	Perpendicular	E = 2155.55 MPa, σ_{ult} = 86.7 MPa, U_0 = 0.1613 N/mm
		3-point bending 2540 mm/min	Parietal	Perpendicular	E = 3127.05 MPa, σ_{ult} = 71.7 MPa, U_0 = 0.4361 N/mm
(Jans, Van-Audekercke et al. 1998)	7-11 months	3-point bending 30 mm/min	Parasagittal	Unknown	E = 1.7-3.3 GPa, σ_{yield} = 115-235 MPa***

*Properties calculated using inverse finite element method

**Properties calculated using beam theory appropriate for small deformations and uniformity; results may have significant error

***Calculated using 3-layered skull assumption, with 2:1 ratio of cortical to diploë

McPherson and Kriewall (1980) and Kriewall (1982) both concluded that the elastic modulus of infant frontal and parietal bones was dependent on fiber orientation. Independent of gestational age, the moduli of samples with parallel orientation (with respect to the suture) were significantly higher than that of the perpendicular samples. However, subsequent researchers investigating infant skull bone material properties have not considered this in their study designs.

In a similar study, Kriewall et al. (1981) measured the ash content of fetal cranial bone in order to determine if the positive correlation found between elastic modulus and ash content in adult bone (Mather 1968; Currey 1969) was valid for infant bone. Their results showed a large spread in ash content data, reflecting the dynamic nature of mineralization and ossification in the developing fetus. Based on r-values, Kriewall concluded that, for pediatric specimens, structural development is more likely to account for an increase in elastic modulus than ash content.

Although suture could not be harvested from post mortem human subjects by Margulies and Thibault (2000) due to standard autopsy procedures, Runge et al. (1998) procured samples from surgical waste. Coronal, sagittal, and metopic suture were excised from 3- to 15-month-old patients and tested in tension at 18-1800 mm/s. These samples exhibited slightly nonlinear behavior (Figure 21) and were much stiffer than bone. When measuring the most linear portion of the suture curves, the authors estimated an average stiffness 189 N/mm for the 3-month-old subject.
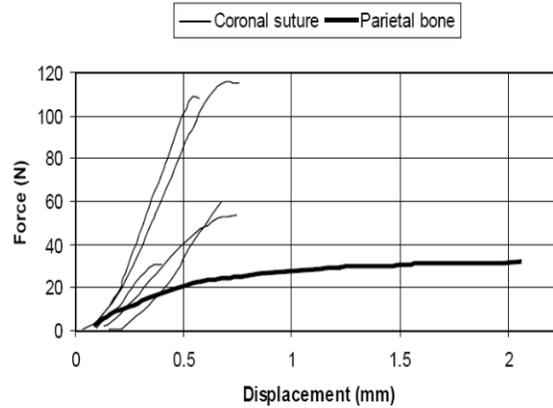
Figure 21 Force-displacement curves for infant at 30 mm/s, reproduced from Runge et al. (1998)

Piglet skull and suture material properties – To compare the properties of infant cranial bone with the bone and suture of the piglet, Margulies and Thibault (2000) employed 2- to 3-day-old piglets. Long, rectangular samples 3-5 mm by 20-25 mm were harvested parallel to the sagittal suture and spanning the coronal suture. Two types of test were conducted on the piglet samples: 3-point bending with an adjustable span and tension to failure. The 3-point bending tests were performed at the same displacement rate as the human sample tests (2.54 and 2540 mm/min), but the tensile tests were performed only at the lower rate due to excessive vibration in the servohydraulic testing machine.

The results of the bending tests at the low rate produced similar elastic moduli for both tests (within the standard error), but higher failure stress and failure strain energy than the tensile tests, as shown in Figure 22.
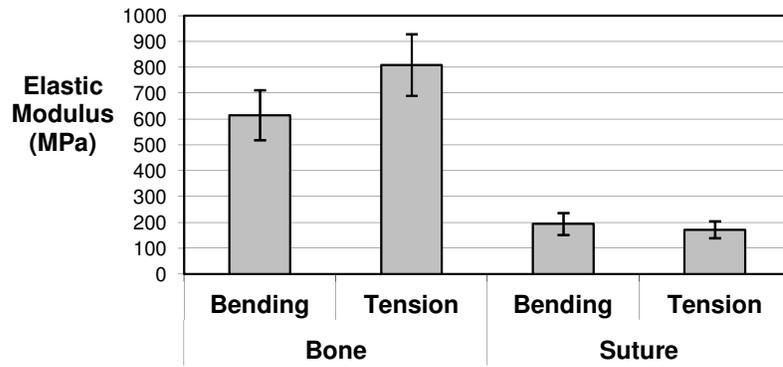
(A)
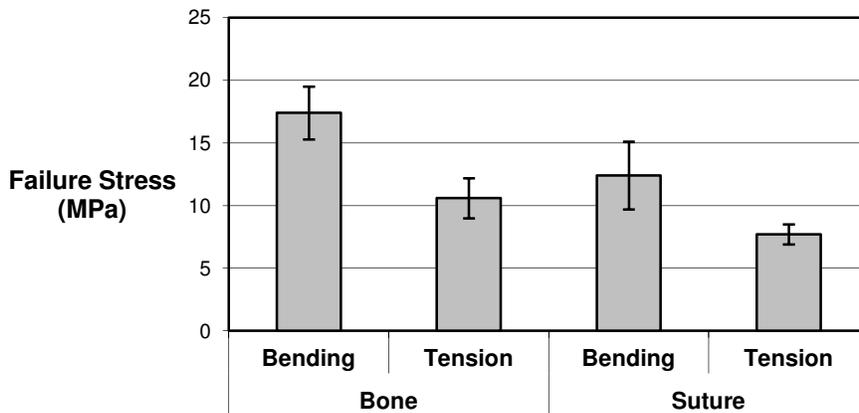
(B)
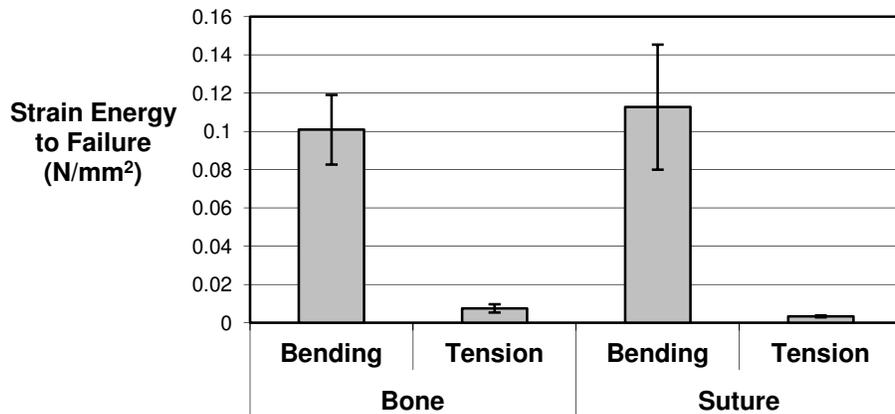
(C)

Figure 22 Comparison of bending and tension results, from Margulies and Thibault (1998)

Note that there was no statistically significant difference between bone and suture for failure stress or strain energy. However, based on the results of the tension tests, it was determined that bone is stiffer than suture, and suture yields and fails at higher strains than bone, as seen in Table 3. In this study, the elastic modulus and failure stress were found to be rate dependent for both bone and suture materials, but the strain energy to failure (U_0) was not.

Table 3 Porcine tension test results, from Margulies and Thibault (2000)

	σ_{yield} (MPa)	σ_{ult} (MPa)	ε_{yield} (mm/mm)*	ε_{ult} (mm/mm)*	E (MPa)*	U_0 (N/mm^2)
Bone	5.3 ± 0.9	10.6 ± 1.6	0.0079 ± 0.0010	0.0341 ± 0.0069	809.0 ± 118.9	0.0075 ± 0.0022
Suture	5.7 ± 0.9	7.7 ± 0.8	0.0422 ± 0.0040	0.0664 ± 0.0078	171.5 ± 32.5	0.0033 ± 0.0005

* Indicates statistical significance ($p < 0.05$)

Another study using 3- to 5-day-old piglet skull and suture samples was conducted at higher rates (Coats and Margulies 2006). The 3-point bending tests were performed using a specialized drop stand to achieve rates of 2.16 and 3.67 m/s (nominal speeds of 2.45 and 4.24 m/s lowered by frictional resistance). These loading rates were not consistent, due to the nature of drop stand procedures, and the impactor mass was not reported, though the mass will affect results significantly. The results are reported in Table 4 . In this study, bone exhibited a higher elastic modulus and ultimate stress than suture, but lower ultimate strain.

Table 4 High speed porcine bone and suture properties, as reported by Coats and Margulies (2006)

|		E (MPa)	σ_{ult} (MPa)	ε_{ult} (mm/mm)*
2.16 m/s	*Bone*	158.9 ± 15.7	10.8 ± 1.0	0.099 ± 0.010
	Suture	57.1 ± 8.2	6.0 ± 0.6	0.176 ± 0.018
3.67 m/s	*Bone*	165.1 ± 18.3	11.2 ± 1.2	0.104 ± 0.011
	Suture	83.8 ± 9.9	7.7 ± 0.8	0.141 ± 0.021

Comparing the results of the high speed study (Coats and Margulies 2006) with the lower speed study (Margulies and Thibault 2000), initiates questions about rate dependence in porcine bone and suture. Figure 23 graphically shows the rate dependence seen in the lower speed study, and a lack of rate dependence in the higher speed study, although direct comparison can be misleading due to differing test methodologies. Further research is needed into the rate dependence of developing bone, as it may behave differently than adult bone in any species.
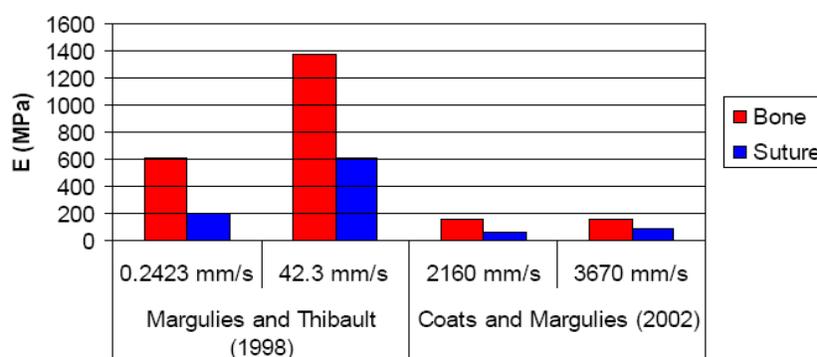
Figure 23 Rate dependent elastic moduli in piglet skull and suture

Older piglets were tested by Baumer et al. (2009), and these material property data were used in the current study in order to examine age related changes with the developed computational models. Bending tests were performed at a loading rate of 25 mm/s in order to identify material property behavior and failure parameters of small rectangular samples of piglet skull bone in piglets aged 7 to 21 days. Although other researchers have employed 3-point bending for this purpose, a 4-point bending apparatus (shown in Figure 24A) was chosen for this study in order to avoid direct loading to the suture (which can affect material property calculations). Two sample types were tested and shown in Figure 24B: pure bone and bone-suture-bone.
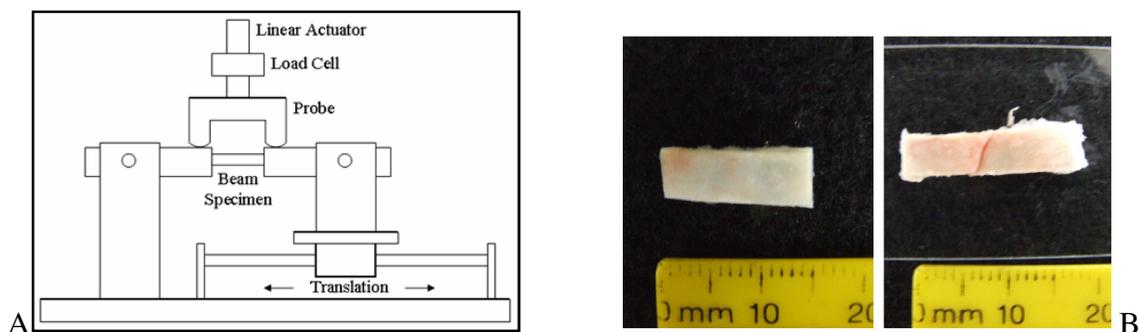
Figure 24 (A) Bending fixture used to determine elastic bone and suture properties and (B) described beam samples [graphic reproduced from Baumer (2009), photos provided by Timothy Baumer, Orthopaedics Biomechanics Laboratory, Michigan State University]

Strain (ε), elastic modulus (E) and internal energy (U) were calculated using the following beam theory equations:

$$\varepsilon = \frac{2y\alpha}{L} \qquad E = \frac{M}{\alpha}\frac{L}{2I_{avg}} \qquad U = \int_0^L \frac{\left(M^*\right)^2}{2EI_{avg}}dx$$

Note that these equations are appropriate for a beam of uniform thickness and homogeneous material, and the angle of deflection, α, is measured at the two impactor contact points. In this case, thickness was averaged from three equally spaced points along the beam, some inherent calculation error is expected. As per Currey (1999) and others, a bending test depicts two mechanical properties simultaneously: material and structural, and it is difficult to separate the two. In other words, it is difficult to determine to what extent factors such as porosity, mineral content, or microstructural orientation of the bone cells play a role in bone behavior and fracture.

Figure 25 illustrates the elasticity results graphically by age group, wherein differences between suture and bone moduli are only statistically significant after 14 days. A slight decreasing trend in bone modulus with age can be seen, but is not

statistically significant. Baumer compared this trend to post-natal human data published by Margulies and found that there was no significant change up to six months of age in infants when pre-natal specimens are excluded. An increase in bone porosity with age was noted and related to structural development of the diploë, but mineral content was not examined.
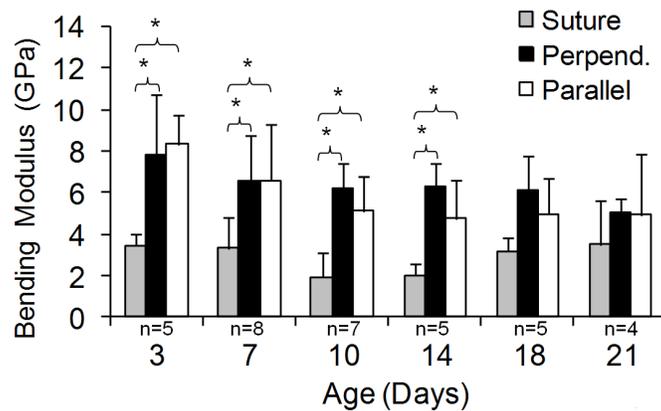
Figure 25 From Baumer's thesis (2009), indicating a significant difference in bending modulus between bone and suture specimens in the younger piglets, but not in the older age group

Other findings from these bending tests are that the orientation of the bone samples does not affect results significantly. This is consistent with some published human data, but not other infant and piglet data (such as Margulies and Thibault, 2000). However, the two sample types (parallel and perpendicular) were taken from the same regions in all piglet specimens. Regional differences were not considered, and also note that all bone samples were taken from the parietal bone, neglecting the possibility that different bone plates could have different properties which affect the overall biomechanics of head compliance and deformation.

Comparison of human data to piglet data – As seen in Chapter 2, there is wide variation in human infant skull material property data. In the parallel fiber orientation, at

quasi-static rates, the elastic modulus is reported to vary between approximately 1 and 5 GPa. In the perpendicular orientation, 100 MPa to 2 GPa is reported for low rates. The higher speed (42.3 mm/s) bending test data for piglets from Margulies and Thibault (2000) also fall within these ranges, although their neonate data were at the lower end of the range, along with the data from Runge et al.'s (1998) higher speed tests. The two studies with older infants (Jans et al. 1998; Margulies and Thibault 2000) matched better with the quasi-static perpendicular orientation data than with the quasi-static parallel orientation data, although Margulies and Thibault used parallel orientation and Jan's orientation is unknown. Because 8-10 GPa is normally considered appropriate for skull material in the adult, it is clear that the developing human skull has age-related differences in terms of material properties. At the current time, the change in material properties as any species matures has not been fully quantified or characterized from birth to adulthood, so it is difficult to determine a correlation metric. However, as mentioned previously, one possible correlation has been postulated from bending rigidity data (Baumer et al., 2009), though the authors also noted that the change in elastic modulus by age did not show statistical significance in the age range tested in their study. Further research is required before results from piglet surrogate tests can be directly translated to human.

The little amount of suture material property data available does not allow researchers to draw any conclusions in comparison. The human suture data published by Runge et al. (1998) indicates that human infant suture is stiffer than bone, but using the piglet surrogate, Margulies and Thibault (2000) found the opposite trend. Both studies elicit concern in their findings. Runge's study only reported data from one

subject, and used two different methods to calculate the properties for bone and suture. Margulies and Thibault tested both materials in both 3-point bending and tension, but found significant differences in their calculated material properties based on the test method. In addition, the beam theory equations used by Margulies and Thibault (2000) and Baumer et al. (2009) are appropriate for uniform specimens subjected to small displacements. In the Margulies and Thibault study, it is acknowledged by the authors that their suture samples exceeded the 5% strain maximum associated with these equations, but the amount of error may be significant and could not be calculated. Further research is needed on suture properties in both species to determine both appropriate modeling techniques and material properties.

Fracture mechanics and failure modes

In an engineering material, there are several modes of failure that can occur:

- Elastic instability - buckling
- Tensile instability - necking
- Large elastic deformation - jamming
- Gross plastic deformation – yielding
- Fracture

These can also occur in combination, and in order to properly model a structure's behavior, the combined failure mode should be understood. Modeling just one failure mode may not produce suitable results. In this work, focus will be on fracture, as the bending failure modes of partially ossified bone (as in developing pediatric subjects) have not been thoroughly investigated experimentally.

Fracture mechanics theory is clear that using a purely elastic assumption, stress at the crack tip is mathematically infinite (see Figure 26). As a practical concern, this is clearly not possible, and therefore any real-world elastic material displays a small plastic zone near the crack tip. For the purposes of finite element modeling, this is important in assigning a proper failure criterion. If this zone is relatively small compared to the entire crack length, then an elastic assumption may be employed. Two criteria can be used at the crack tip to determine whether or not propagation will occur in linear elastic fracture mechanics. K is a local criterion related to local stress at the crack tip, and G is a global criterion based on strain energy release. As the crack lengthens, this assumption becomes increasingly inaccurate and new fracture criteria will be needed which consider elasto-plastic fracture mechanics. Another consideration in biological mathematical modeling of fracture must be natural inhomogeneities, analogous to manufacturing flaws in man-made materials. These affect both crack initiation and propagation.
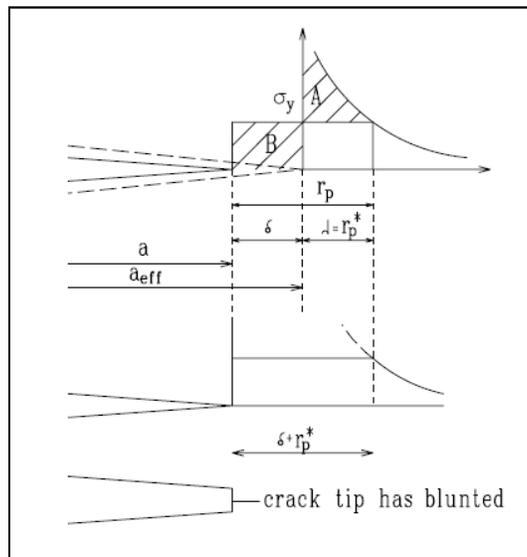
Figure 26 Graphical summary of fracture mechanics theory

From a biomechanics standpoint, the most common type of skull fracture is linear fracture. In these cases, the mechanism of injury is termed "outbending," as described by Gurdjian et al. (1970). The impacted area is deformed inward, while, due to the elastic nature of the skull, areas distal to the impact site bend outward. Bone can be considered transversely isotropic with weakness in tension, so fractures can occur in regions of outbending. Gurdjian hypothesized that linear skull fractures initiate at the point of outbending and propagate towards both the impact site and the area directly opposite the impact site.

In some types of impact, it has been shown that many seemingly important parameters may not affect resultant skull fracture force (Allsop, 1993; Nahum et al., 1968; Schneider and Nahum, 1972). These parameters include: onset loading rate, pulse duration, strain rate, bone mineral content, and state of preservation. However, bone thickness has been shown to affect fracture tolerance (Allsop, 1993; Melvin et al., 1969). Although no systematic studies have been performed to quantify the effect of local skull thickness on fracture pattern, there have been studies that suggest fracture lines follow areas of thinness or that skull thickness does affect fracture pattern (Willinger, 2000; Weber, 1985).

The basis of the finite element method is to describe a physical system by mathematical parameters and to approximate the behavior of the system through solving a series of partial differential equations using the framework of linear algebra. This method allows a researcher to depict a physical system using discretization, limiting the possible degrees-of-freedom in the mathematical model to a non-infinite, solvable set.

Skull fracture can be modeled using a threshold failure criterion (strain, stress, or strain energy are common). Once an element meets this threshold, it can be mathematically handled in different ways: removal of the element from the model or assignment of null stiffness. Due to the discretized nature of a finite element model, either one of these changes the structural stability of the model by removing that element's strength from the stiffness matrix, however, the mass is retained at the nodes in the case of element elimination so that the overall mass of the system is unaffected. The energy balance is also affected.

Experimental studies of skull bone have shown that architecture and bone thickness to be important parameters in fracture tolerance (Allsop, 1993; Melvin et al., 1969). Simplifications are made in finite element modeling to represent this composite structure as layers of 2D or 3D elements. Material assumptions are also made, as the bone is physically inhomogeneous, with anisotropic and nonlinear behavior. Generally, models of cortical bone assume isotropy and even linearity, as the degree of nonlinearity is relatively small. Failure thresholds reported in the literature are based on engineering stress or strain calculated using theoretical equations, not accounting for inter- or intra-specimen variation.

Bone behavior is viscoelastic, and its failure can be described using several criteria, most commonly maximum principal stress (Seely and Smith, 1966). In this case, elongation along the loaded axis is proportional to the maximum principal stress. The material has lower resistance against shear in this configuration and can fail along a non-orthogonal axis; as such, maximum shear strain becomes the primary failure mode. Therefore, strain is considered the better predictor of bone fracture, and material

property tests from the 1970's reported failure strains of 0.33-0.9% (Wood, 1970; Hubbard, 1971) for adult human skull bone. Piglet skulls have been tested by one group of researchers (Margulies and Thibault, 2000; Coats and Margulies, 2006) and 3.4% was reported for quasi-static rates, while 10% was reported for dynamic rates as detailed earlier in this chapter. Without further study, it is difficult to determine whether these discrepancies are related to species, age, bone architecture, loading rate, or test condition. Finite element models of the infant head generally have estimated failure strains around 3%, but the Coats model is much lower, although not under 1%. Additionally, because none of the published infant finite element models involved mesh convergence studies, failure strain estimated from model predictions is mesh-dependent and should not be applied to other models without due consideration. These models do not generally use element elimination to represent failure, instead predicting areas in which fracture is more likely based on strain contours. As stated in the review, pediatric finite element models have also used stress-based criteria to determine likely fracture sites. If bone is modeled as elastic, this assumption is valid, but further research may be needed when more complex constitutive equations are used to describe bone behavior.

Methods

Geometry and mesh generation

Baumer (2009) reported that the structural morphology of the piglet bone specimens tested experimentally showed a distinct, continuous trabecular layer in piglets over 14 days old. Additionally, while the bone stiffness increased linearly with age, the suture stiffness only increased statistically significantly after 14 days, which affects the global stiffness of the cranial vault. Because this is obviously not an

instantaneous occurrence, due in part to anatomical and developmental variation in piglet specimens, two models will be developed representing piglets with a buffer of seven days from this cutoff point (7 and 21 days of age).

The geometry necessary for FE model development was obtained through CT imaging and 3D reconstruction. A 0.5 mm resolution spiral CT scan (Siemens, Detroit Receiving Hospital, Detroit, Michigan) was performed axially on a 21-day-old intact piglet head and exported in DICOM format. This resolution was not sufficient for an accurate depiction of the thinner 7-day-old piglet head and a microCT (built in-house at Henry Ford Hospital, Detroit, Michigan) was employed for a second scan in order to capture multiple voxels through the skull thickness for an accurate reconstruction. One region of interest (a cross-section of the parietal bone) is shown in Figure 27 which shows that the skull thickness ranges from 1.6 to 3.4 mm at 21 days but 0.5 to 1.3 mm at 7 days. However, the 90 µm resolution microCT scan could not be performed on the entire piglet head, due to bore size and field-of-view limitations. Instead, a post-impact dried skull was imaged and reconstructed through post-processing. Given the nature of the physical reconstruction of the post-impacted dried skulls, glue introduced into the sutural space will make the sutures appear wider than they are in reality. Observation of fresh, intact pig skulls indicates that the suture width in a 7-day-old piglet does not seem to be significantly different from the 21-day-old. This phenomenon does not correlate with infants, and the implication thereof will be discussed in the conclusion of this dissertation.
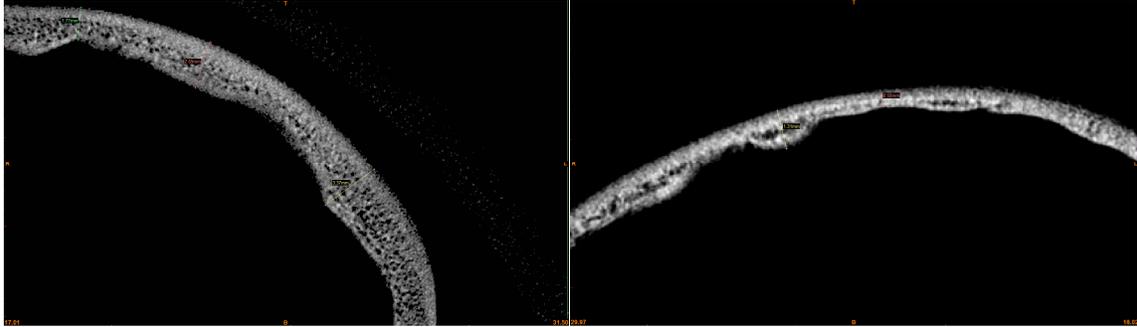
Figure 27 90 µm resolution cross-sections of the parietal bone (left = 21 days, right = 7 days)

For 3D reconstruction, the images were imported into Mimics 13 (Materialise, Leuven, Belgium). Thresholding, region-growing, and other segmentation techniques were applied to reconstruct the skull bones (see Figure 28). The inner and outer surfaces of the skull were converted to STL format, in which the surface is represented by connected 2D triangles in 3D space. The inner and outer surfaces were separated, and the foramen magnum and all other anatomical orifices were filled to preserve intracranial pressure in simulation. Manual smoothing algorithms were utilized to prepare the outer skull surface for meshing, balancing anatomical accuracy with curvatures suitable to minimizing warpage during meshing.

A   B
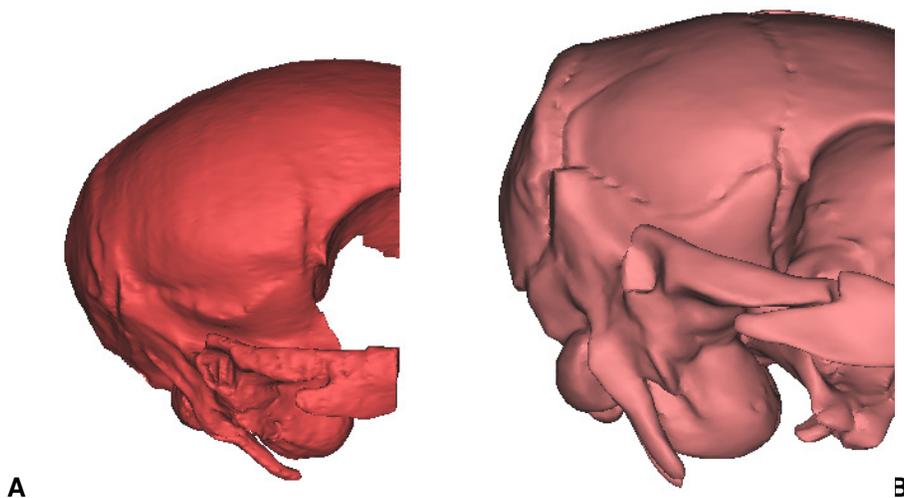
Figure 28 7-day-old (A) and 21-day-old (B) piglet skull 3D reconstructions

The final outer skull STL file was exported to Hypermesh 9.0 (Altair, Troy, Michigan), where the triangular surface mesh was manually converted into 4-node quadrilateral shell elements on the parietal bone, with care taken to preserve element quality. The Hughes-Liu shell element formulation was used in this model. Shell elements were chosen because they can support both bending and transverse shear, related to the hypothesized mechanism of injury in this case. Both fully and reduced integration schemes were investigated, but for this model, they were not found to show significant difference in results. The remaining skull bone plates- including the occiput, frontal bones, temporal bones, nasal bones, and maxilla- were meshed using automated optimization and mixed elements in Hypermesh. Through convergence testing, a mesh size of 0.5 mm was chosen. Elements were selected to represent the areas of sutural interdigitation, and the edges of these lines were smoothed manually. Summaries of the meshed models are shown in Table 5.

Table 5 Piglet skull and suture meshes

7-day-old (7DO)	21-day-old (21DO)
Total shell elements = 51,640 Total solid elements = 62,490 Average element size = 0.5 mm >10% warpage = 5% <0.6 Jacobian = 1% Initial timestep size = 3.58 e^{-6}	Total shell elements = 93,860 Total solid elements = 271,096 Average element size = 0.5 mm >10% warpage = 3% <0.6 Jacobian = 2% Initial timestep size = 3.53 e^{-6}

Material model theory and failure criterion

Based on the literature review and the data reported by Baumer et al. (2009), several constitutive models were considered. A typical force-displacement curve from Baumer's 4-point bending experiments is shown in Figure 29. From this graph, no plastic region is evident, though a toe region and an elastic behavior can be seen, as well as some evidence of strain softening. Based on published studies regarding the biomechanics of bone fracture, evidence of yielding and plastic behavior, as well as rate dependence, should be expected. It is unclear if the lack of a plastic region is an artifact of test methodology or a consequence of pediatric growth and development. Other researchers have observed that although the bone may appear brittle, energy absorption does occur through plastic flow beyond the elastic limit (Wainwright, 1979), so it is likely that the testing mode's inability to separate structural and material effects is the cause of this inconsistency, as described by Currey (1999).
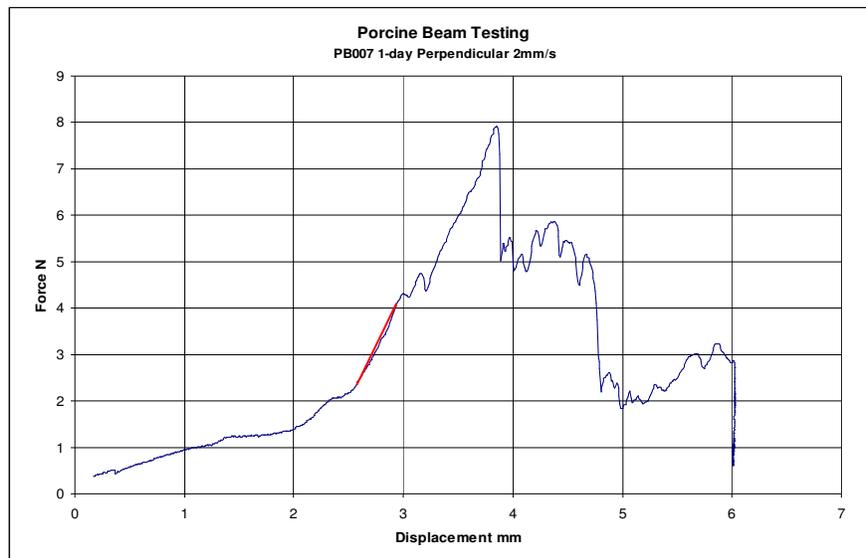
Figure 29 Force-displacement curve for typical beam specimen *[provided by Tim Baumer, Michigan State University]*

As discussed in Chapter 2, bone consists only partially of mineral components. Especially in a developing skull, there is a significant contribution to material response from collagen. If one makes the assumption that both of these major components display purely elastic behavior, but with different moduli and ultimate stress/strain, Figure 30 shows what the typical stress-strain curve would be expected to look like. After failure of the mineralized bone, the collagen matrix would be expected to support some loading before failure (Burstein, Zika et al. 1975). As this is not what happens, it should be understood that bone itself is not an elastic, brittle material.
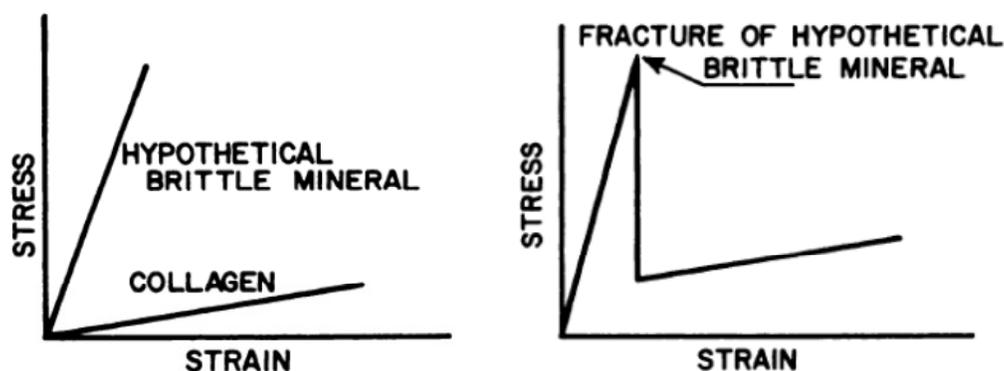
Figure 30 Hypothetical bone failure response *[Reproduced from Burstein et al. (1975)]*

The mineral content of the piglet bones was not measured in the MSU tests, but it can be assumed that the growth of the skull plates at these ages indicates some level of mineralization. In Burstein et al. (1975), as well as other published literature, cortical bone was shown to exhibit elastic-plastic properties, with failure occurring in the plastic region. Partial demineralization of the bone did not affect the general shape of the curve, but rather only the elastic modulus and yield stress. Even the ultimate strain remained unchanged until complete demineralization, at which point it increased significantly.

Two constitutive models were chosen based on the above information and the availability and compatibility of material models in LS-DYNA v971. Of the available material failure models that were compatible with shells, MAT24 was chosen to represent the elastic-plastic behavior of the bone without orthotropic effects. MAT3, a similar model, has been used to model failure in other biomechanical studies (Li et al., 2009; Guan et al., 2011). However, the failure algorithms in LS-DYNA do not allow for a separate tensile and compressive strain failure threshold, which was postulated to be relevant to the failure mode of the piglet head (i.e., outbending). Even in the absence of the outbending phenomenon, the mechanics of bending dictate that the material will be in compression on the outward bending surface and in tension on the inward bending surface, and separate criteria would still be relevant.

The observed fracture patterns in the experiments were seen to be at the bone plate margin (near the edges of the parietal bone), as opposed to under the impactor. It was hypothesized that this was a bending phenomenon, similar to the outbending that has been reported elsewhere. Bone is more resistant to fracture in compression, due to the effects of Wolff's law (which states that bone adapts to repeated or continuous loading so as to provide a stronger resistance), so failure is much more likely to occur due to tension. This may be relevant to the skull in that intracranial pressure and cerebral convolutions provide a constant force, though small, that the cranial skull bones must resist. In infants, these convolutions, which give the brain surface its characteristic uneven appearance, begin to develop around the age of five months (Hofman, 1989) and contribute to the shape of the inner skull surface. Bone deposition

and loading, especially during development, will affect the compression/tension failure thresholds regionally in the brain case.

There is an extension of the elastic-plastic model with failure (MAT24), which allows separate plastic stress-stress curves to be defined for tension and compression (MAT124). Although only one failure criterion value can be defined in LS-DYNA, changing the yield stress and/or tangent modulus can delay or prevent element elimination in areas experiencing compressive mean stress (e.g., in direct contact areas).   The plastic regions were defined artificially (see Figure 31) assigned to strengthen the bone in areas of compression (i.e., the impact point at the center of the parietal bone), as no data appropriate to regional dependency were generated as a part of the current study. The other bones were modeled as elastic without failure for simplicity.
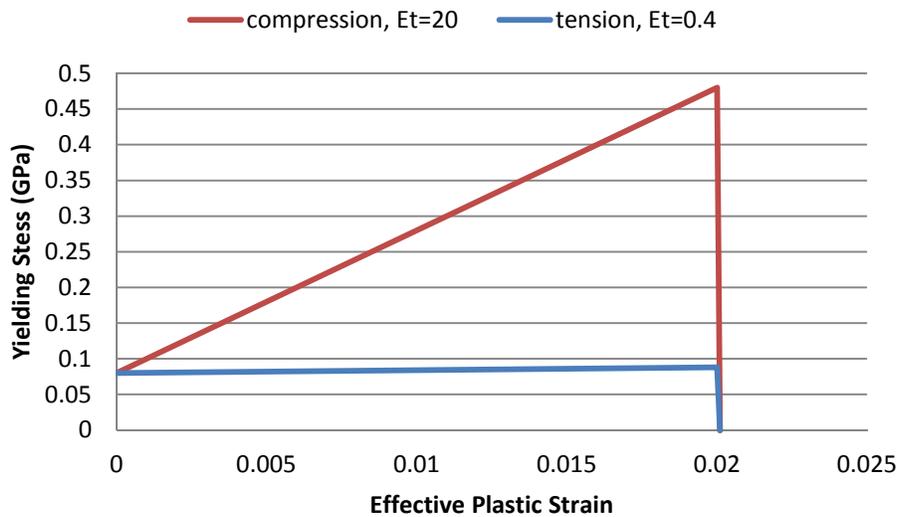
Figure 31 Plastic region behavior assigned in MAT124 to strengthen impact point

In this constitutive model, effective plastic strain is defined as the failure criterion. When a certain strain parameter reaches its threshold, the element is deleted from the

simulation, with the mass retained at the nodes. The ε_p of each element at each time step is calculated based on the following, explained more fully in the LS-DYNA user manual:

$$E_p = \frac{E_t E}{E - E_t} \qquad \Delta\varepsilon^p_{eff} = \frac{\left(\frac{3}{2}s^*_{ij}\, s^*_{ij}\right)^{1/2} - \sigma_y}{3G + E_P} \qquad \varepsilon^p_{eff} = \int_0^t \left(\frac{2}{3}\dot{\varepsilon}^p_{ij}\, \dot{\varepsilon}^p_{ij}\right)^{1/2} dt$$

It can be seen that the selection of tangent modulus and yield stress contributes greatly to the numerical development of plastic strain within the shell elements. One reason that the numerically defined failure strain differs from the experiments is that microcracks and other incomplete fractures are not considered. Additionally, while crack propagation is determined by strain energy vectors, these are not be well-defined in the context of MAT124.

Another material model was also utilized to investigate the efficacy of an energy-based criterion. MAT105 is an elastic viscoplastic material model combined with continuum damage mechanics to define element deletion thresholds (Berstad et al., 1999). An effective plastic strain is defined at which material softening begins, the so-called 'damage threshold' r_d. Critical damage progression is defined through the strain energy release rate (a function of Von Mises stress) as:

$$\dot{D} = \begin{cases} 0 & \text{for} & r \leq r_D \\[2mm] \dfrac{Y}{S(1-D)}\dot{r} & \text{for} & r > r_D \quad \text{and} \quad \sigma_1 > 0 \end{cases}$$

$$Y = \frac{1}{2}\mathbf{e_e} : \mathbf{C} : \mathbf{e_e} = \frac{\sigma^2_{vm} R_v}{2E(1-D)^2} \qquad R_v = \frac{2}{3}(1+v) + 3(1-2v)\left(\frac{\sigma_H}{\sigma_{vm}}\right)^2$$

The value of S is a damage material constant with a default value of 1/200 of the initial yield stress.

The constitutive equations defining element deletion in this material model are obviously more complex than the effective plastic strain threshold in MAT124. In addition to the continuum mechanics damage criterion, elements assigned MAT105 can also be given an effective plastic strain threshold, if the critical damage value is not reached. In this study, that option was not utilized in order to avoid the appearance of confounding effects during failure criteria evaluation.

Boundary conditions

Data generated from experimental tests conducted at the Orthopaedic Biomechanics Laboratory (OBL) at Michigan State University (MSU), and published in Baumer et al. (2010), was used for model validation. More details are available in the literature, but briefly, a drop stand was used to produce non-catastrophic failure leading to linear skull fractures. The drop stand developed at OBL for blunt force impact studies on *in vivo* articular cartilage (Haut et al., 1995) was used to control the impactor in this series of experiments (Figure 32). The impactor was fixed to the carriage of the drop stand, which traveled vertically along a stainless steel shaft via high precision roller bearings. The piglet head was potted in air-hardening epoxy (Fibre Strand, Martin Senour Corp., Cleveland, OH) and oriented in such a way that the center of the parietal bone is in the line of impact. In order to assure a single impact, an op-amp comparator circuit initializes an electromagnetic solenoid to catch the rebounding impactor when the load returns to zero after a load spike. A load cell underneath the intact head recorded global impact force.
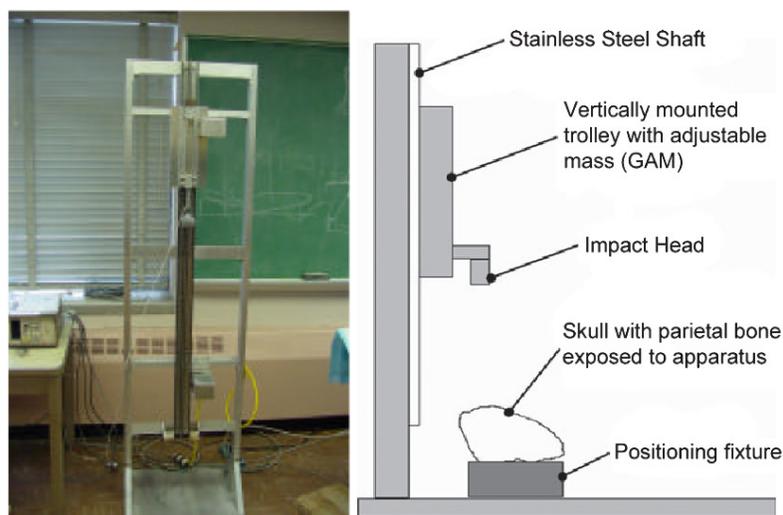
Figure 32 OBL Drop Stand *[images provided by Timothy Baumer, Orthopaedic Biomechanics Laboratory, Michigan State University]*

The piglet skull model was fixed in six degrees-of-freedom opposite the impact site. A layer of solid elements representing the compliant skin between the relatively rigid potting material and the flexible skull was incorporated to allow impact energy absorption consistent with the experiment. The aluminum (elastic, E = 70 GPa) impactor was modeled with a 5 mm thick layer of brick elements on the impactor surface to represent the skin of the pig (elastic, E = 100 MPa). Using this technique simplifies numerical contact interfaces that must be utilized in FEM. Validation of contact area for a given impact energy was necessary to ensure reasonable computational models for fracture pattern prediction.

The center of impact was located at the center of the parietal bone plate (Figure 33). Based on the drop heights reported by Baumer (2009), impact velocity for each piglet model was calculated using the following basic physics equation and reported in Table 6:

$$v = \sqrt{2gh}$$

Table 6 Loading conditions

	Impactor Mass (kg)	Drop Height (m)	Impact Velocity (m/s)	Impact Energy (J)
7DO	1.7	0.20	2.0	3.3
21DO	1.9	0.60	3.4	11.2
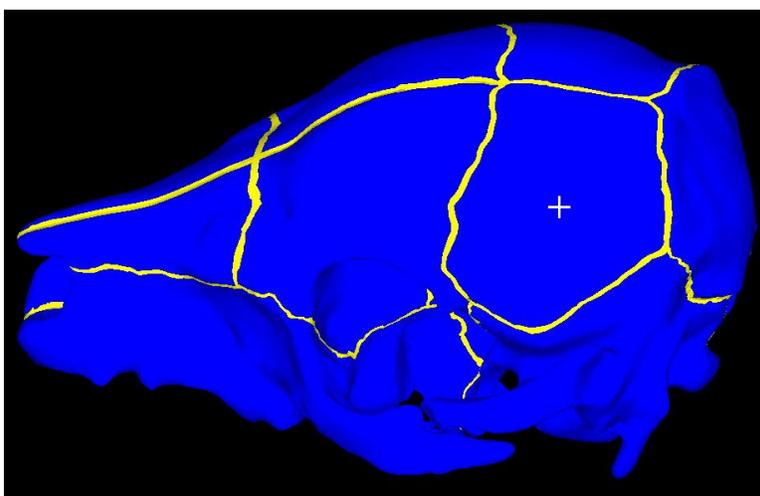
Figure 33 Impact point at center of parietal bone marked by white cross

Results

Convergence study

In order to confirm that the use of thin shell elements to support the bending load modality in this study would be appropriate, a simple mechanics problem was modeled to investigate the convergence of thin shells with varying edge length to thickness ratios. A simply supported, 10-cmx10-cm 2-mm thick square plate was subjected to a 10 N static load and solved using implicit methods in LS-DYNA. The edge length of the uniform, quadrilateral mesh was varied from 5 to 0.3125 mm by a factor of 2. The results are shown in Figure 34, convergence on the theoretical solution. An element size of 0.5 mm, with a thickness four times greater was well within acceptable

convergence range, indicating that thin shells are appropriate for modeling even relatively thick piglet skull bone plates.
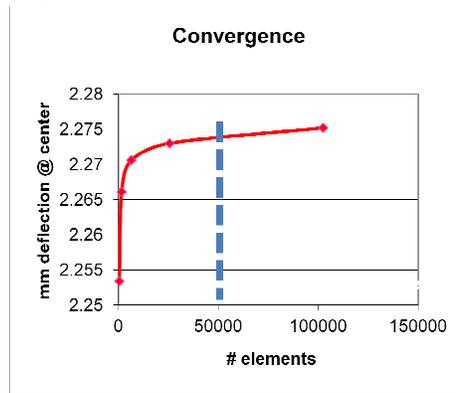
Figure 34 Convergence of a simplified plate problem with the theoretical solution-the dashed line represents a 1:4 edge length to thickness ratio with 0.5-mm edge length

Simulated fracture prediction

Fracture patterns – The laboratory tests produced highly consistent fracture patterns within the age groups tested in high energy impacts, as shown in Figure 35. These data use a geographical information systems (GIS) technique to map the fracture lines from several piglets to a representative geometry for comparison. High-speed video observation indicated that the fractures initiated remotely from the impact site and propagated towards the center of the parietal bone. Despite this, Figure 36 shows that the fracture lengths display a wide variance, with no trend by age and cannot be used reliably for comparison with fracture prediction models.

Younger age group (2-9 days)

fracture
frequency

☐	0 - 1
▨	2 - 2
▨	3 - 4
▨	5

Older age group (18-28 days)
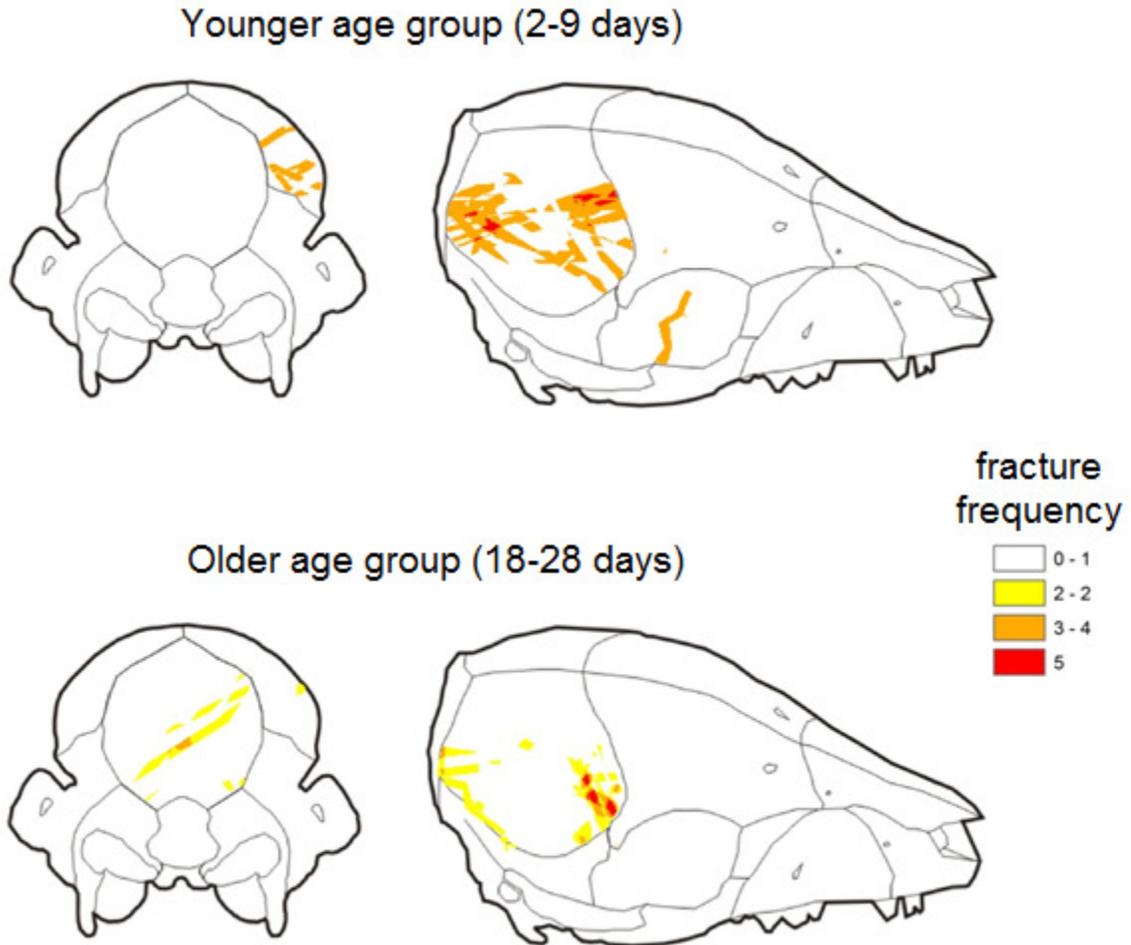
Figure 35 Accumulated GIS fracture location data showing likely areas of fracture [provided by Nicholas V. Passalacqua, Department of Anthropology, Michigan State University]
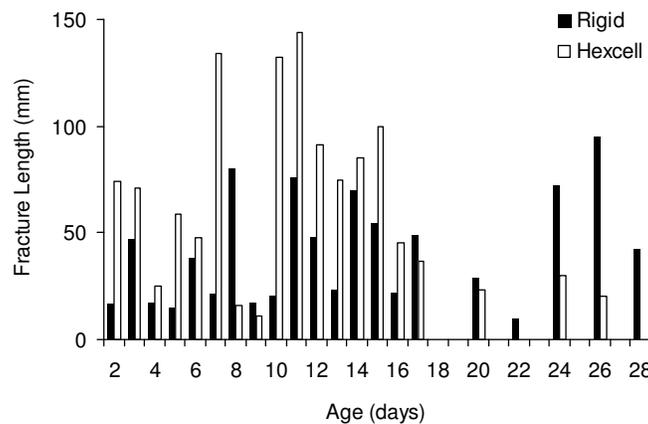
Figure 36 Characteristic fracture lengths reported by and reproduced from Baumer et al. (2010) – note very large variance and lack of distinguishable trend

Failure criterion – With these initiation points in mind, the two failure criteria, strain and strain energy, were compared in 21-day-old pilot models. These models were given similar elastic governing behavior and impact conditions, but the plastic behavior and failure thresholds were necessarily different and were not selected to produce optimal fracture patterns at this stage. (This is explored further in Chapter 4.) For the pilot models, plastic behavior was dictated by the values in Table 7 in order to encourage element elimination for comparison of moderate fracture patterns, more severe than those described above in order to fully investigate propagation.

Table 7 Plastic behavior in 21-day-old pilot models

	MAT 105 (BOTH)	**MAT 124 (TENSION)**	**MAT124 (COMPRESSION)**
E_t	1 GPa	400 MPa	20 GPa
σ_y	100 MPa	80 MPa	80 MPa
ε_y	0.8%	--	--

Simulation results are shown in Figure 37. It is evident that the artificial strengthening of the bone area under the impact center does not prevent fractures from occurring in the center of the parietal bone. The strain energy-based criterion predicts a less diffuse fracture pattern, more in agreement with the laboratory tests. Further investigation was indicated to determine appropriate parametric values for material behavior and failure, which were performed iteratively and reported in Chapter 4, using only the elastic-viscoplastic constitutive model.

A
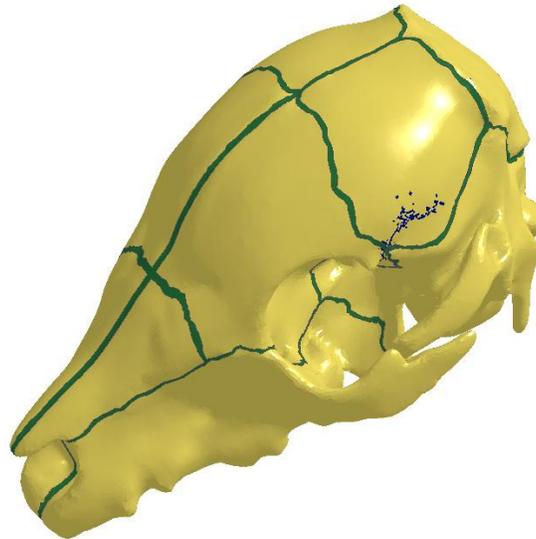
B

Figure 37 Initial fracture patterns at 1.5 ms for strain-based (A) and strain energy-based (B) failure criteria, initiating at a similar point at the junction of the squamosal and coronal sutures

Further results are shown in Appendix 2 for, comparing the biomechanical response of the 7- and 21-day-old MAT105 pilot models. Stress and strain contours at peak deflection show higher sensitivity to biomechanical response criteria not considered for failure thresholds in LS-DYNA. This will be incorporated with the findings of the parametric studies and discussed in more detail in the conclusions of Chapter 5.

Validation

To ensure that the computational models using MAT 105 produced global behavior consistent with the experimental subjects, the following criteria were obtained from Baumer et al. (2009). For this dissertation work, only rigid impacts were considered; the average contact area for a 7-day-old piglet was 120 mm^2 with 610 N contact force, and the average contact area for a 21-day-old piglet was 215 mm^2 with 955 N impact force, as seen in Figure 38. Peak displacements were calculated by integrating acceleration curves from the impactor and were not measured locally. The resulting data had a very large deviance, and given that they were global measurements, were not considered appropriate for validation in this study. For reference, the deflection ranges were on the order of 4 to 17 mm for rigid impacts in piglets from 2 to 28 days of age.
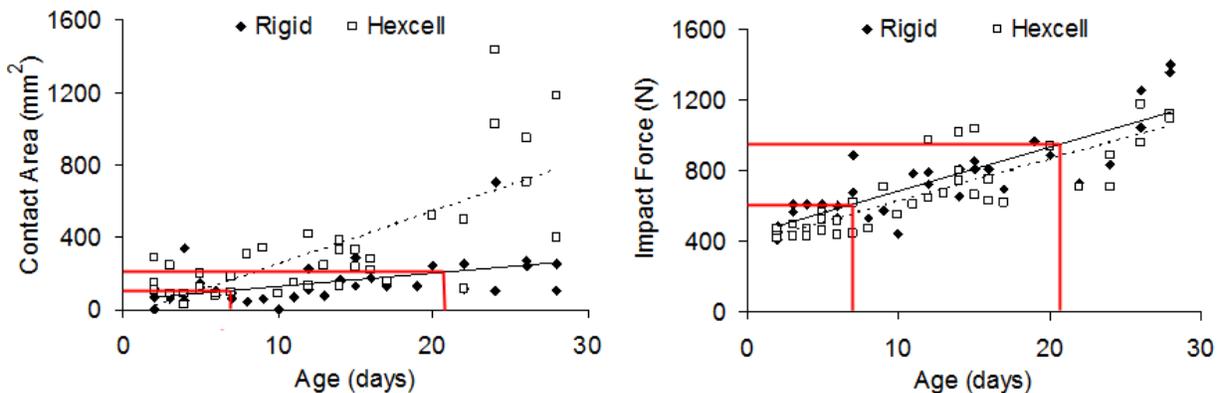
Figure 38 Contact area and impact force with red lines showing validation data for the 7- and 21-day-old models [reproduced from Baumer et al. (2010)]

For the 7-day-old model, the validation results are shown in Figure 39. As in the experiment, the impactor rebounds, as shown in Figure 39A. The peak displacement is less than those reported by Baumer (2009), which will be discussed later. The energy

balance, shown in Figure 39B, shows no sign of hourglass energy loss, although a slight decrease in total energy due to element deletion is evident. Contact area was calculated by creating a bi-color representation of the indented region of the impactor shown in Figure 39C at peak parietal deflection and using a histogram to determine the percentage of area contacted. This calculation yielded good agreement at 125 mm^2, within 4% of the target value. Contact force was over-estimated by the solver, a known problem in LS-DYNA, which can be exacerbated by additional contact definitions needed to account for voids left by deleted elements, so this parameter was disregarded in favor of fracture pattern analysis.

A

B

C
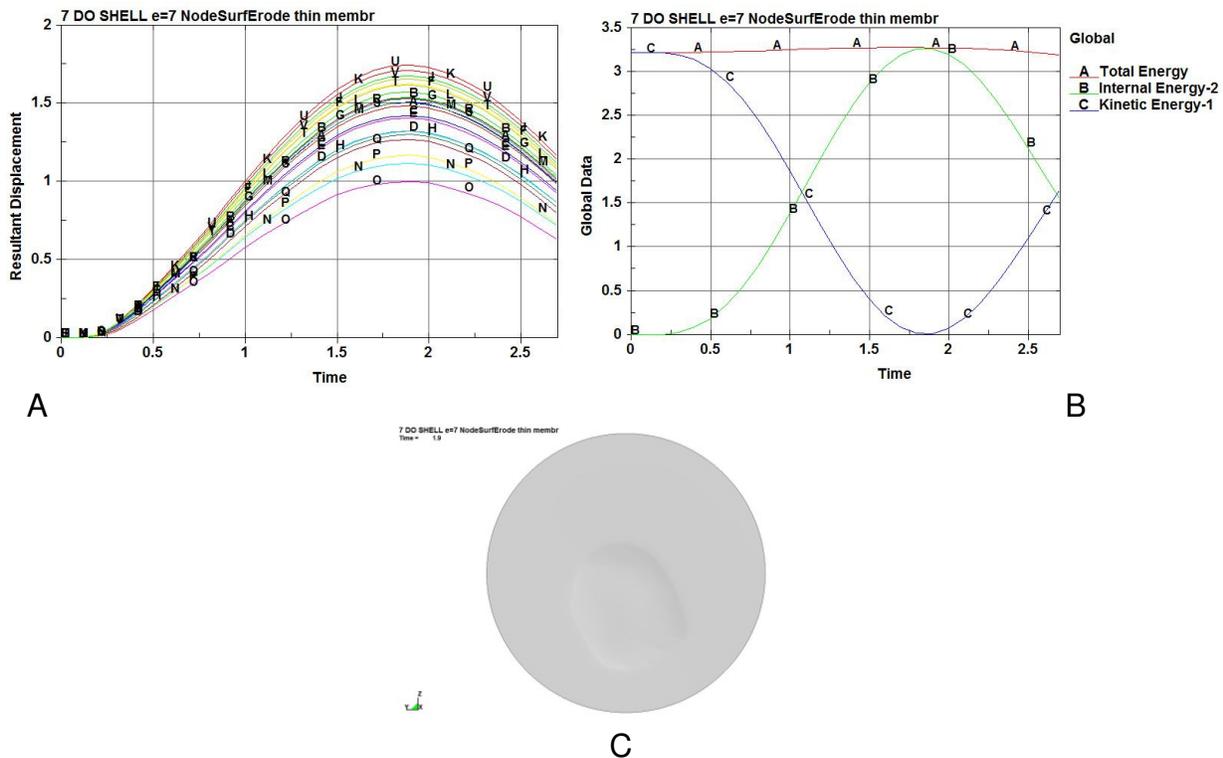
Figure 39 Validation criteria for the 7-day-old model baseline simulation, where (A) shows peak parietal bone displacement in mm vs. time in ms, (B) shows global energy output in J vs. ms time, and (C) shows the contact area indentation

The 21-day-old model showed a higher peak deflection (Figure 40A), due to a combination of increased impact energy and decreased bone stiffness. The energy balance remained constant overall (Figure 40B), indicating that energy loss in the 7-day-old model was due to effects other than element elimination. The contact area did not match as well for the 21-day-old model, with 280 mm^2 predicted by the simulation, an over-prediction of 30%. This is probably due to the engagement of the occipital ridge, which is more prominent in the 21-day-old piglet than in the 7-day-old piglet. It is unclear whether this was also a factor in the laboratory tests or was possibly not within the scope of measurement. Further investigations into impactor orientation are reported in Chapter 4 and highlight the importance of this finding.

A

B

C
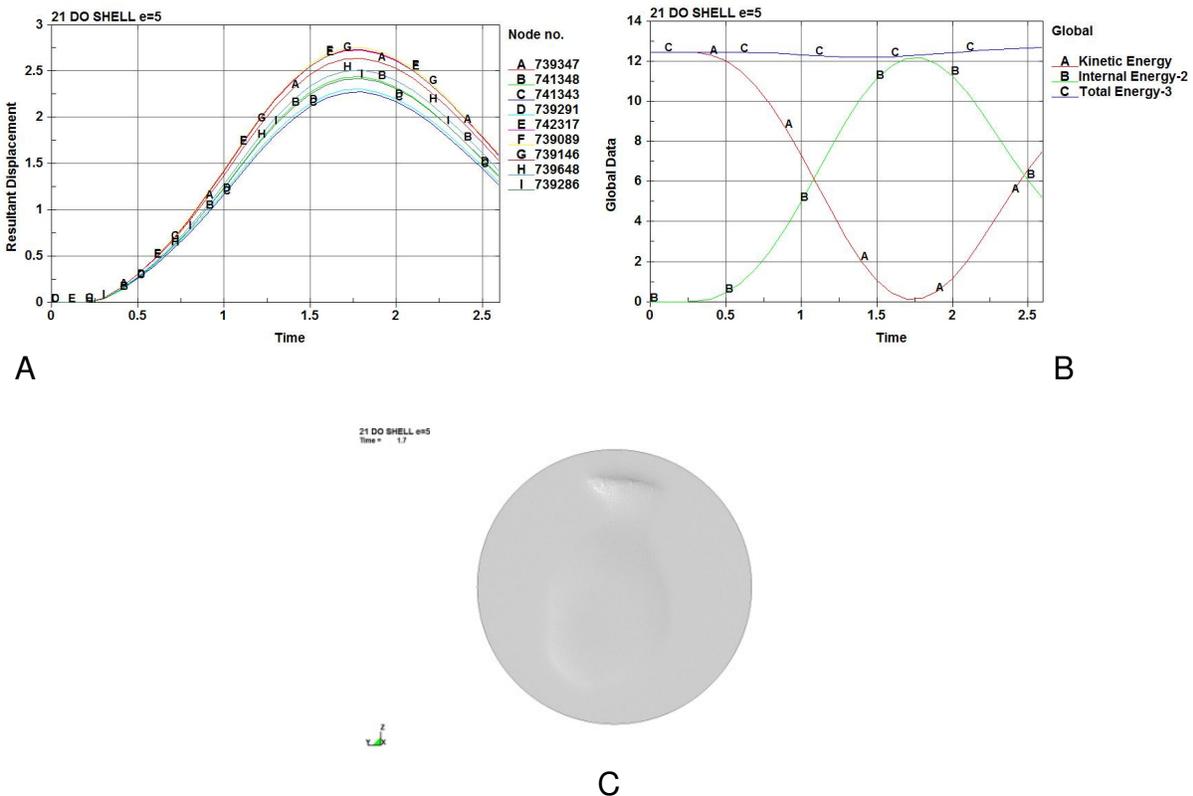
Figure 40 Validation criteria for the 21-day-old model baseline simulation, where (A) shows peak parietal bone displacement in mm vs. time in ms, (B) shows global energy output in J vs. ms time, and (C) shows the contact area indentation

Discussion

The computational models developed in this study required a solution time of approximately 30 hours on 16 AMD Opteron CPUs with 2.4 GHz clock speed. The computational resources needed were dictated by several model factors, including the skin soft tissue calculations, contact definitions for the void left by deleted elements, and the small element size. Although a convergence study was performed to determine the suitably of Hughes-Liu shell formulation, the effect of element size on failure was not considered. Because of the nature of the element deletion technique, simulated fracture lines appear wider in the computational model than in the physical experiments. Given the overall agreement with global biomechanics data, it can be assumed that the effects are negligible; however, further sensitivity studies of the complete skull model would be appropriate before deployment for forensic analysis when computational resources are sufficient for the task. The current element size of 0.5 mm was chosen based on current computational limitations and confirmed to be globally appropriate, but confirmation of failure convergence would be ideal.

A comparison of the 7- and 21-day-old models in terms of fracture initiation site can be seen in Figure 41. This may be an effect of the overall skull compliance, in particular, the relative compliance of the suture relative to the bone. In the 7-day-old model, the bone was assigned an elastic modulus of 7 GPa, more than twice the 3 GPa of the sutures. For the 21-day-old model, the bone elastic modulus was 5 GPa. Although Baumer et al. (2009) reported this was not a statistically significant difference by age, these values were chosen to investigate the overall effects. The biomechanical parameters used for validation were not affected adversely, leading to the conclusion

that the global deformation of the skull was reasonable for both ages. However, when the plasticity and failure material parameters were kept identical (as in the models of Figure 41), fracture initiation sites in the 7-day-old model seemed to occur more remotely from the bone margin and were not as accurate. Whether this is a geometric or material effect is unclear.

Figure 41 Fracture initiation sites in the 7-day-old model (A) and the 21-day-old model (B)

Despite these fracture initiation results, the current failure algorithms/criteria available in the commercial software code LS-DYNA is not complex enough to replicate fracture patterns as accurately as required. As the fracture progresses, the results become more inaccurate. Sensitivity and robustness studies are needed to determine whether the use of MAT105 for bone fracture modeling is appropriate. These studies are reported in Chapter4.

As mentioned previously, the failure thresholds determined by these models cannot be directly translated from experiment to computational model. Besides the macro versus micro-structure argument, there are also numerical considerations. The failure strain defined within the model is calculated per element. Therefore, model results pertaining to element elimination are necessarily mesh dependent. Another issue is that contact force may have numerical artifact in the LS-DYNA solver and may be affecting the calculation of the failure threshold values. The failure criterion used in this study may not be appropriate to other models, which must be considered when translating the results to human models in the future.

Additionally, material property data available is insufficient for a complete understanding of the fracture behavior of pediatric bone tissue, which makes it difficult to employ user-defined crack initiation and propagation algorithms. The data produced by Baumer (2009) reports only elastic behavior, which may be due to the use of a bending load modality (Currey, 1999), and does not identify the location of crack initiation in either the material tests or the impact tests. Further research is needed by experimentalists if complex failure finite element models appropriate for mature and developing bone are to be developed.

Conclusion

Fracture initiation sites can be predicted by current finite element modeling techniques, but further refinement of the constitutive models to include fracture mechanics theory and crack propagation algorithms are needed in commercial software packages such as LS-DYNA. The reliability of such models must be quantified in order to offer useful predictive ability.

Despite the amount of data available for piglet skull bone material, more experimental studies are necessary to understand the plastic behavior of the bone, especially in the context of mineralization and ossification. The ossification center of the parietal bone seems to indicate that the material properties of a growing bone are region-dependent, and this may affect simulations significantly, especially when relying on a simplified method of representing bone architecture. Structural concerns remain a limitation of using shell elements to simulate bending. Further analysis is needed.

CHAPTER 4

**PARAMETRIC STUDIES AND SENSITIVITY OF THE
PIGLET SKULL FRACTURE MODEL**

Objective

The objective of this chapter is to exercise the piglet head finite element models for the purpose of determining which input parameters most affect the resulting fracture pattern and severity. Through systematic validation and parametric study, the biomechanical fidelity of the model can be ascertained, even quantified, to lend confidence to simulation predictions and identifying sensitive parameters. Design of Computer Experiments (DOCE) can provide insight into pediatric skull fracture biomechanics across species and generate guidance for translation of the piglet head model's findings to forensic applications and future experimental/computational work.

Introduction

The development of a validated piglet skull fracture model is an intermediate step towards the development of pediatric skull models that can be used in forensic studies. The modeling techniques used to develop the piglet head models in this study have not been used in blunt impact models of this scale, particularly for the head. Parametric studies can be used in iterative simulations to explore a variety of biomechanical input conditions. These conditions can include both model parameters and loading conditions, and both have been exercised in this study to investigate model sensitivity and robustness. Three hypotheses are considered in this chapter:

1) Injury mechanism hypothesis – fracture lines follow areas of bone translucency and thinness

2) Failure threshold hypothesis – Critical damage value in MAT105 constitutive model is sufficiently mathematically sensitive

3) Local geometry hypothesis – orientation of the impactor affects fracture pattern due to local geometry

Methods

Injury mechanism hypothesis

The original hypothesis for injury mechanism involved fracture lines following regions of translucency corresponding to local thin areas on the bone plate. In order to determine if regional variations in thickness of the parietal bone explain inter-subject variability in fracture pattern results, the following procedure was developed to allow variable element thickness in the parietal bone of the computational model.

The thickness of each cranial bone was calculated through an in-house program coded in Python 2.4, which projected the quadrilateral mesh for each bone plate onto the unsmoothed inner surface STL, in a direction normal to the elemental surface. Figure 42 graphically describes the procedure. This determined an accurate thickness value at discrete local points corresponding to nodal positions of the mesh. The thickness values of the four nodes which defined each quadrilateral element were averaged to define element thickness, and the frequencies of each thickness value (in increments of 0.1 mm) were plotted on a histogram. Only parietal bone regional effects were considered, and the shell elements were assigned one of ten thickness values based this histogram frequency to investigate the effect of the uneven inner skull surface on fracture pattern.
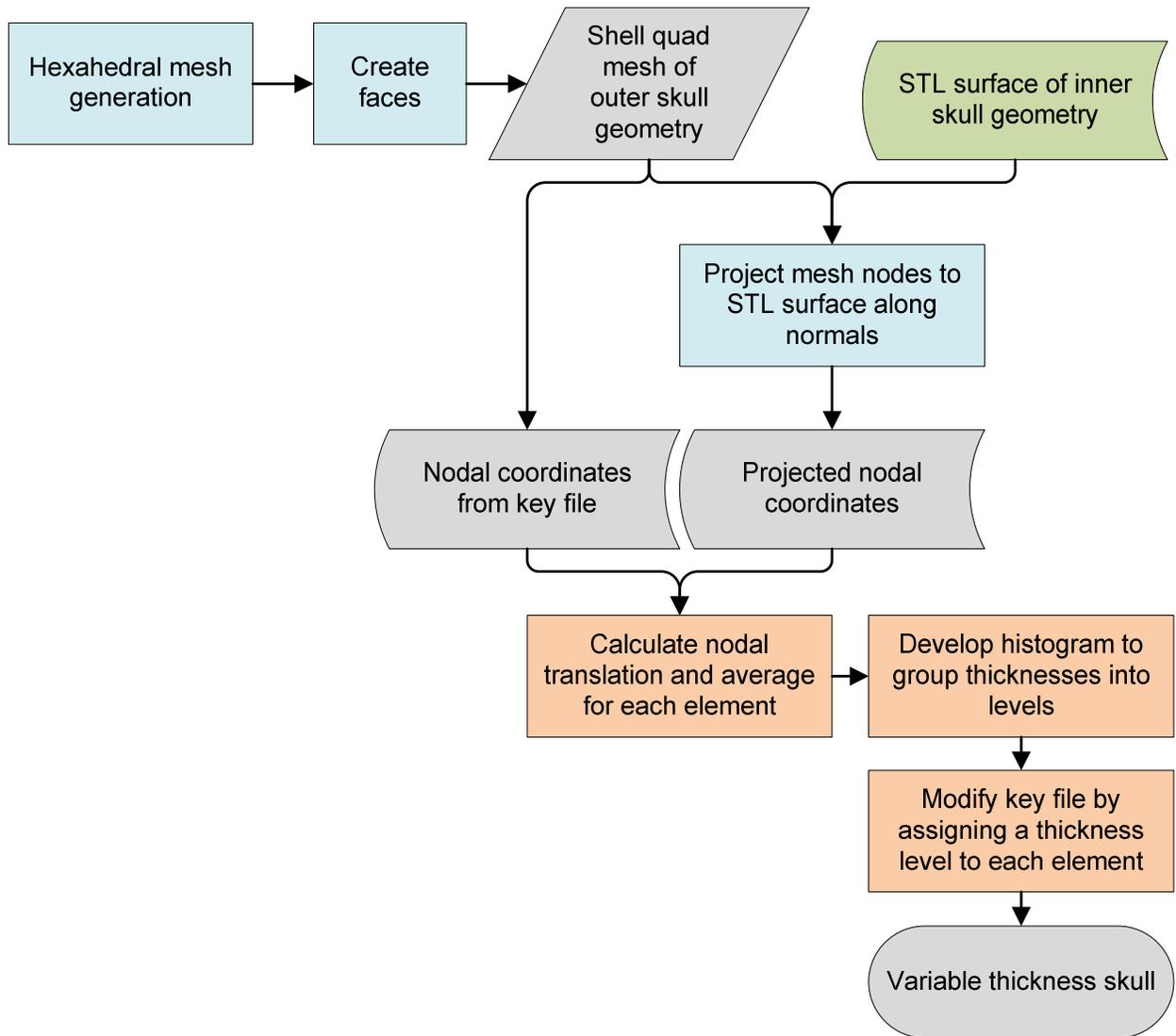
Figure 42 Flowchart describing Python algorithm (blue boxes are performed in Hexmorpher, green in Mimics, gray in Hypermesh, orange in Python scripting)

Failure threshold hypothesis

Design of Computer Experiments (DOCE) was utilized to test the hypothesis that once an appropriate failure criterion was established, the threshold parameter was sensitive enough to differentiate between failure and non-failure loading. Several parameters from the constitutive model were chosen for analysis using a full factorial

design (as shown in Table 8) for the 21-day-old model only, to remove the confounding effects of differing geometry and mesh pattern.

Table 8 Full factorial DOCE matrix

ID	BONE		
	DC	E (GPa)	EPSD (10^{-2}%)
0	0.001	8	0.01
1	0.001	8	0.015
2	0.001	8	0.02
3	0.001	10	0.01
4	0.001	10	0.015
5	0.001	10	0.02
6	0.001	12	0.01
7	0.001	12	0.015
8	0.001	12	0.02
9	0.002	8	0.01
10	0.002	8	0.015
11	0.002	8	0.02
12	0.002	10	0.01
13	0.002	10	0.015
14	0.002	10	0.02
15	0.002	12	0.01
16	0.002	12	0.015
17	0.002	12	0.02
18	0.003	8	0.01
19	0.003	8	0.015
20	0.003	8	0.02
21	0.003	10	0.01
22	0.003	10	0.015
23	0.003	10	0.02
24	0.003	12	0.01
25	0.003	12	0.015
26	0.003	12	0.02

The failure parameters considered were D_C, the critical damage value at which elements were deleted, and EPSD, the value of plastic strain at which material softening began. Because the results of the validated models reported in Chapter 3 showed fractures more severe than those produced in the laboratory study, the strain softening parameter was increased to delay the onset of fracture initiation and reduce fracture

lengths. Additionally, the bone stiffness, initially predominately determined by the elastic modulus, E, was varied. The ranges for this parameter were chosen to be at the upper end of the data reported by Baumer et al. (2009) in order to exaggerate the influence of the stiffness differences between bone and suture, highlighting the effects of the bending mode of loading.

Local geometry hypothesis

It was hypothesized that local geometric variations effect fracture pattern, especially based on results seen from the engagement of the parietal-occipital boundary and the bone thickness in that area. Although Baumer (2009) noted that the impact direction in the drop stand experiments was normal to the parietal bone surface, this is difficult to quantify visually and some variation should be expected. For this parametric study, the assumption was made that the determination of the parietal bone midpoint (i.e., the impact point) exhibited much less variation and therefore was kept constant in the simulations.

The impactor was rotated around the impact point in four directions, as shown in Figure 43. For each direction, two levels were considered: 1 degree of rotation and 5 degrees of rotation. This was done to investigate what amount of variance resulted in visually observable differences in fracture pattern. Again, only the 21-day-old model was utilized, because the effects were expected to be greater (especially in the negative y direction) due to the more pronounced occipital ridge. The predicted fracture patterns were compared to the baseline model (run ID #20 from the DOCE shown in Table 8).

78
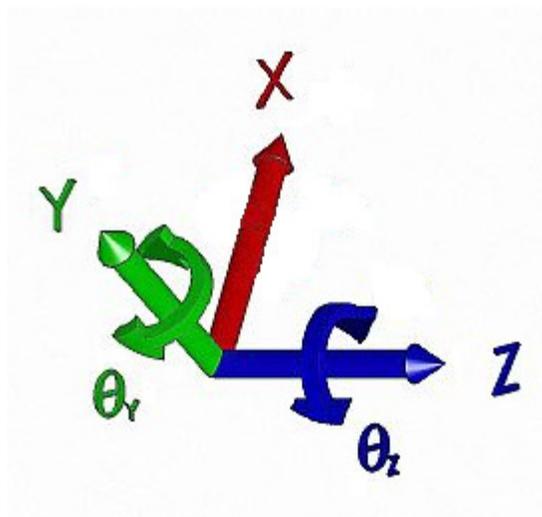
Positive y (+θ_y) anterior	towards coronal suture
Negative y (-θ_y) posterior	towards lamboidal suture
Positive z (+θ_y) inferior	towards squamosal suture
Negative z (-θ_y) superior	towards sagittal suture

Figure 43 Orientation directions along –x impact path

Results

Injury mechanism hypothesis

Porosity – Although predominately material concerns were addressed in this chapter, the issue of porosity and its effect on the beam testing results were considered. In the laboratory-produced impacts, areas of translucency seemed to correlate with fracture likelihood near the bone margins. This has been noted in other studies, such as Weber's, as well. To investigate whether this phenomenon might improve fracture initiation site predictions in the computational model, 17-µm resolution microCT images were procured of dry parietal bone plates. Figure 44 shows the areas of low density or high porosity for each of the piglet ages modeled. No pattern emerges that indicates areas of translucency alone can account for fracture pattern susceptibility leading to the radial fracture patterns seen in the laboratory study.
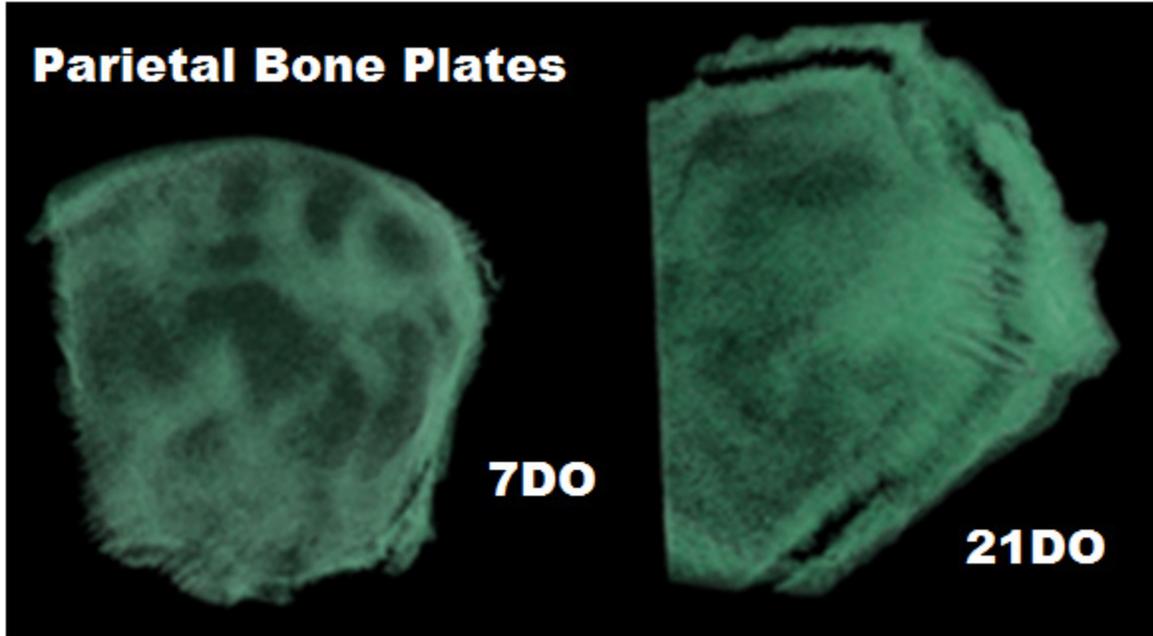
Figure 44 Areas low density appear dark, indicate porous and/or thin local

variation

Bone thickness – Utilizing the method shown in Figure 42, element thicknesses were plotted as the histogram shown in Figure 45. The average element thickness was calcualted as 3.3 mm, with a median of 2.8 mm.
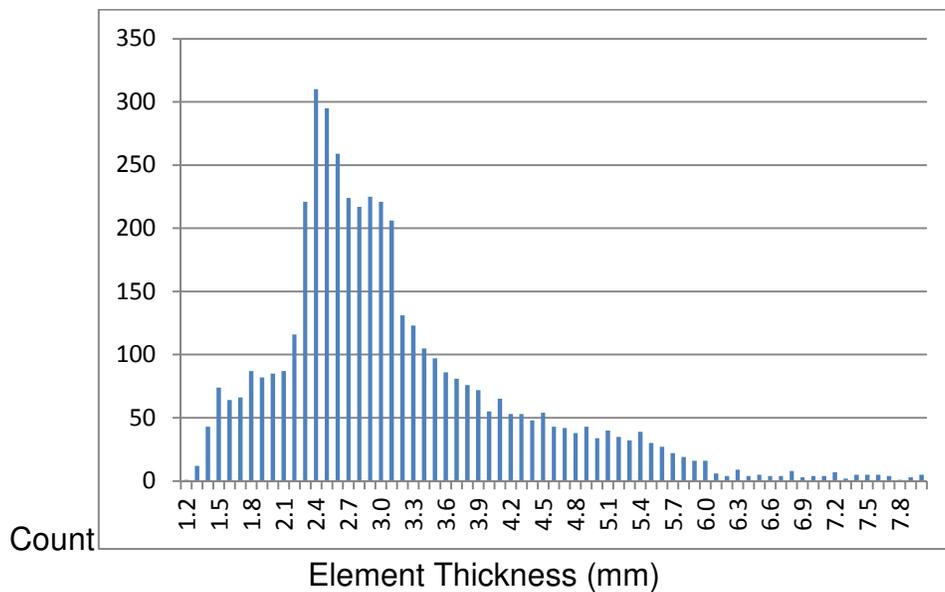
Figure 45 Parietal bone thickness histogram for the 21-day-old piglet head

Element thicknesses were assigned to the computational model, and a contour plot showing the regions of thickness is shown in Figure 46A. The resolution of the element thickness is limited by mesh size, at 0.5 mm edge length, and it can be seen that the change in thickness is gradual (i.e., a very thin element will not be found adjacent to a very thick element). Results indicate that neither fracture initiation nor propagation were positively affected by these local thickness variations, as shown in Figure 46B. In fact, many of the deleted elements are located in areas where the thickness is greatest.

In order to determine whether further mesh refinement allowing higher resolution in local thickness variation would be able to account for bone thickness effects on fracture pattern (should they exist), an artificially-induced fracture was created, as shown in Figure 47. In Figure 47A, the areas in which fracture initiation occurs (outlined in black on the parietal bone inferior aspect) were given 1/6 the thickness of the surrounding bone. The resulting fracture pattern predicted by simulation is very similar to the laboratory-produced fractures. However, when the thickness ratios are less (such as 2/3 as shown in Figure 47B), the effects are no longer observable. The results here are inconclusive, but further mesh refinement is computationally prohibitive in this macro-level model.

Time =   0
Contours of Shell Thickness
min=1.25, at elem# 903954
max=8, at elem# 908081

Fringe Levels

8.000e+00
7.650e+00
7.300e+00
6.950e+00
6.600e+00
6.250e+00
5.900e+00
5.550e+00
5.200e+00
4.850e+00
4.500e+00
4.150e+00
3.800e+00
3.450e+00
3.100e+00
2.750e+00
2.400e+00
2.050e+00
1.700e+00
1.350e+00
1.000e+00
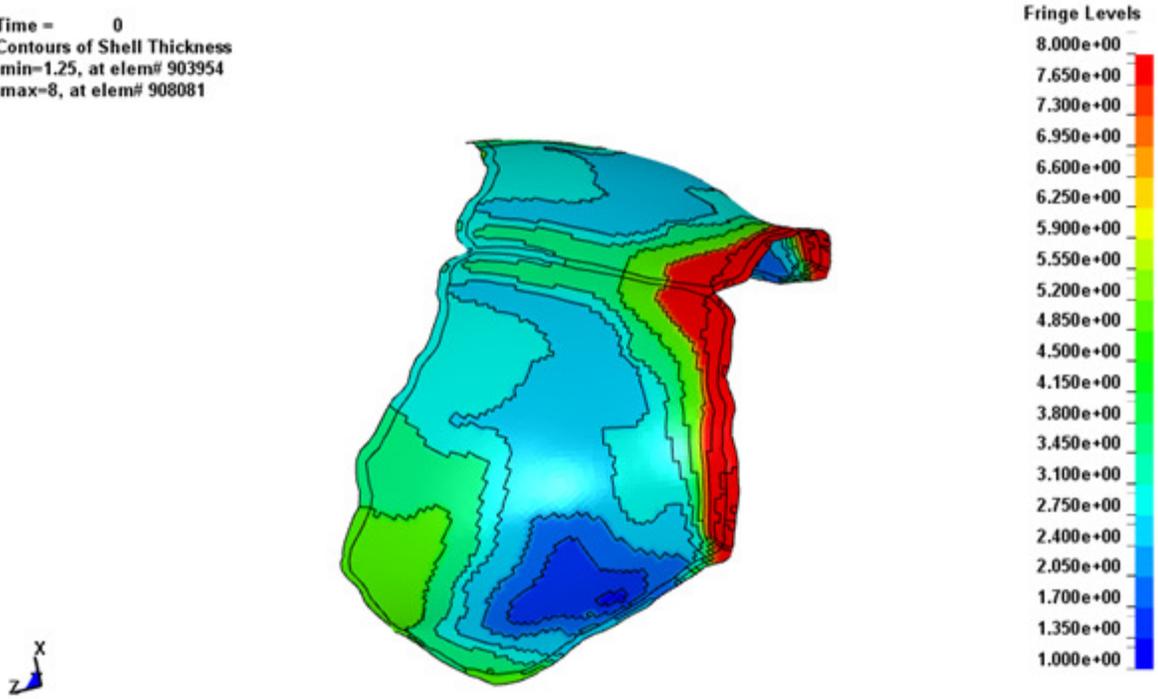
A
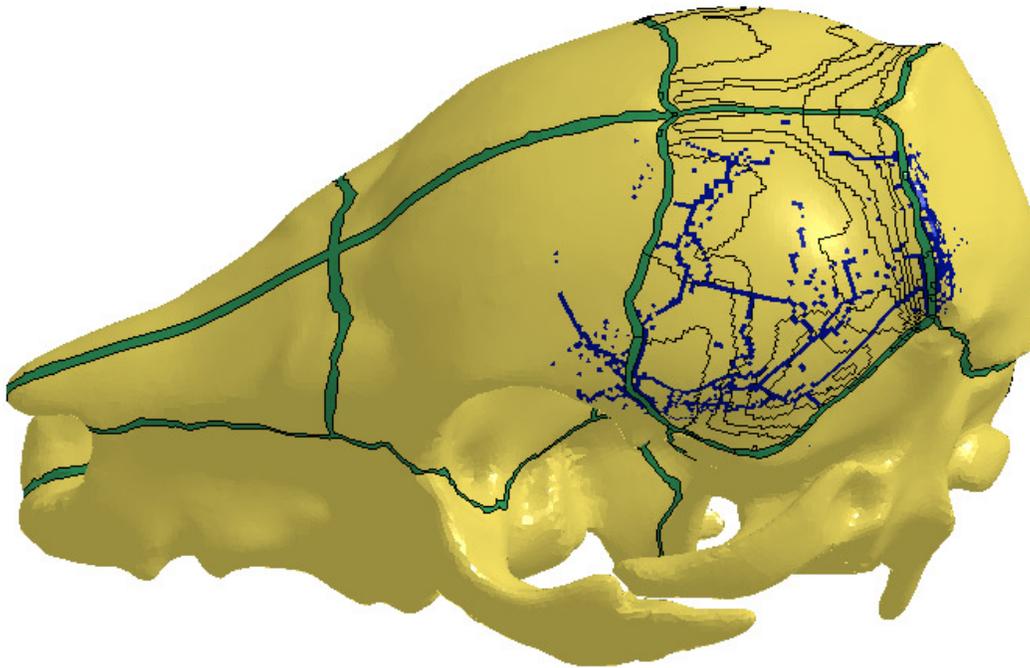
B

Figure 46 (A) Variable thickness assignment of the parietal bone at 10 levels (fringe level unit = mm) and (B) fracture predictions showing no effects of the bone thickness variations

A   B
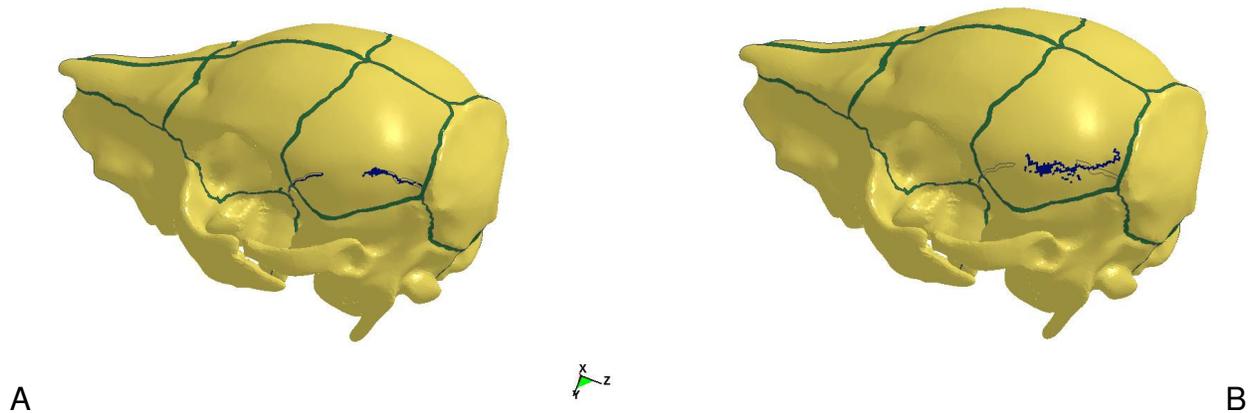
Figure 47 Artificially-created fracture lines (A) with a 1:6 thickness ratio and a more physiologically realistic 2:3 thickness ratio (B) showing the lack of discernable effect

Failure threshold hypothesis

The full factorial DOCE parametric study did indicate that the failure criteria D_C and EPSD had an effect on fracture pattern (see Table 9 and Appendix 3). However, trends were much clearer in the strain softening value, possibly indicating a higher sensitivity to this input parameter. The overall shape of the fracture pattern seemed to be dictated by the bone stiffness, while fracture length and severity were dominated by the failure thresholds.

Sensitivity to the failure parameters may not be sufficient to model mild fractures. The differences in material input between fracture and no fracture simulations were often very small, and further refinement within the ranges of this DOCE did not improve the results. Using this constitutive model and its strain energy-based criterion, once fracture begins, it becomes catastrophic quickly. Given the equations shown in Chapter 3 in which it be seen that the rate of damage accumulation is non-linearly inversely proportional to the instantaneous value of the damage parameter, D, this was not an expected result.

Table 9 DOCE summarized results (also see Appendix 3)

| | INPUT | | | | OUTPUT | | |
ID	DC	E	EPSD		FX	PATTERN	SEVERITY
0	0.001	8	0.01		Y	circular	moderate
1	0.001	8	0.015		Y	circular	severe
2	0.001	8	0.02		N	none	none
3	0.001	10	0.01		Y	circular	severe
4	0.001	10	0.015		Y	circular	moderate
5	0.001	10	0.02		Y	circular	moderate
6	0.001	12	0.01		Y	y-shaped	moderate
7	0.001	12	0.015		Y	linear	moderate
8	0.001	12	0.02		Y	y-shaped	mild
9	0.002	8	0.01		Y	u-shaped	mild
10	0.002	8	0.015		Y	u-shaped	moderate
11	0.002	8	0.02		Y	y-shaped	mild
12	0.002	10	0.01		Y	circular	severe
13	0.002	10	0.015		Y	circular	severe
14	0.002	10	0.02		N	none	none
15	0.002	12	0.01		Y	circular	severe
16	0.002	12	0.015		Y	circular	moderate
17	0.002	12	0.02		Y	y-shaped	moderate
18	0.003	8	0.01		Y	u-shaped	moderate
19	0.003	8	0.015		Y	circular	moderate
20	0.003	8	0.02		Y	linear	mild
21	0.003	10	0.01		Y	u-shaped	mild
22	0.003	10	0.015		Y	circular	severe
23	0.003	10	0.02		N	none	none
24	0.003	12	0.01		Y	y-shaped	severe
25	0.003	12	0.015		Y	y-shaped	moderate
26	0.003	12	0.02		Y	linear	mild

Local geometry hypothesis

Fracture patterns from the impactor orientation study are reported in Table 10. Again, no clear trends are seen; however, the model seems to be most sensitive to changes in which the impactor is rotated towards the squamosal-coronal suture junction, one of the identifiable fracture initiation points from the experimental study. The degree of rotation has some effect due to the curvature of the bone, and it is apparent

that the robustness of this fracture model is insufficient for ambiguous impact conditions.

Table 10 Impactor orientation effects
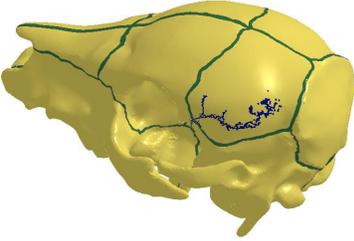
BASELINE		
@1.7 ms	1-degree Rotation	5-degree Rotation
Positive y (anterior)	@ 2 ms	@1.3 ms
Negative y (posterior)	after rebound	after rebound
Positive z (inferior)	after rebound	@1.9 ms
Negative z (superior)	after rebound	after rebound
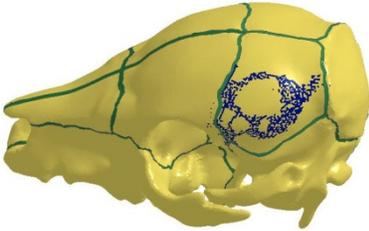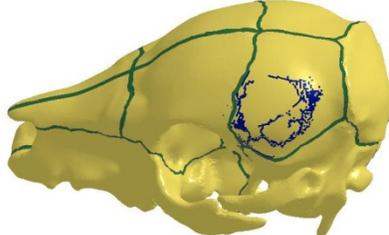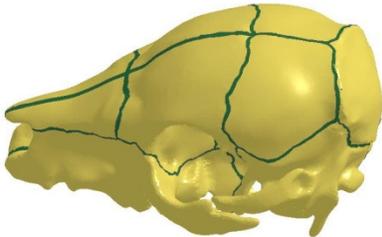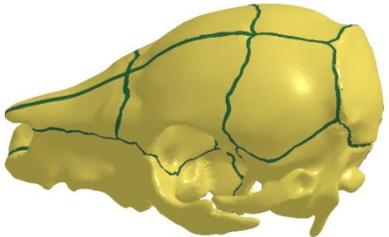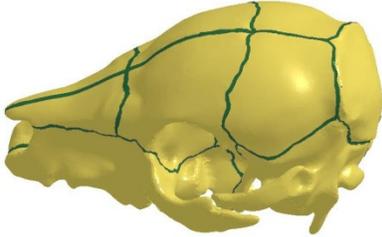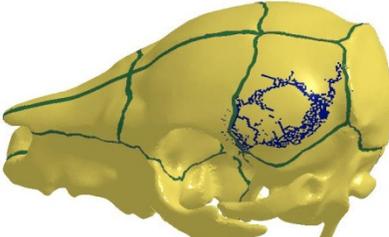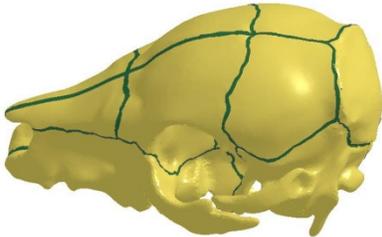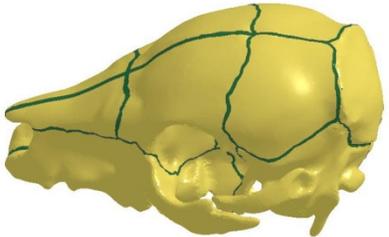
Discussion

The original hypothesis of this study, that bone translucency is the predominant structural factor in skull fracture, seemed to be false, but could not be definitively proven. It was shown that bone thickness or porosity alone were not enough to explain the linear fracture path observed in outbending. Higher resolution of local thickness variation may show greater effect; however, this is limited by computational resources and would be difficult to translate into forensic applications due to that fact.

The usefulness of computational models is limited by their sensitivity and robustness. In this study, it was seen that the failure algorithms in MAT105 in LS-DYNA may not be sufficient for the purpose of modeling mild linear fractures in bone. The all-or-nothing type of response is likely due to the lack of crack propagation algorithms in the LS-DYNA material model. Fracture mechanics theory is well-understood as the development of strain energy at the crack tip; and by applying a strain energy threshold to discrete elements instead, fracture predictions in the computational model are not dictated by the crack tip energy, possibly affecting propagation accuracy even when the alternate failure criterion is valid.

Further tensile tests of developing bone and suture are needed to characterize strain softening effects, which seem to have a profound effect on fracture. Additionally, rate effects have not been considered, and given the amount of collagen and unossified/mineralized bone in pediatric tissue, these effects may be significant. However, this is beyond the scope of this study and would not be expected to overcome the deficiencies in the failure model.

The robustness of the computational model to changes in impactor orientation was poor, as hypothesized. Due to the curvature of the bone plate, there may be a "sweet spot" at which fracture is more likely, and it is postulated that this could be related to structural effects at the ossification center. Further research is needed. A smaller scale computational model (e.g., the parietal bone plate alone) would allow for more in depth validation due to more controlled boundary conditions and higher resolution due to size. Structural effects could be considered at that level, then applied to the maco-level blunt impact models like those seen here.

Statistical significance – Due to the lack of trends seen in these parametric studies, meaningful statistical analysis was not possible.

Conclusion

The development of piglet head models with elastic-plastic bone behavior and failure is of limited relevance without systematic validation. Although the spread of data in the experimental studies can be explained by anatomic variation among piglet subjects, the model is deterministic, representative of only a single case. As with any computational model, some degree of approximation is involved in both model development and solution. The uncertainty of parameters in the model can be exercised with parametric studies and statistical analysis in order to determine quantitatively their relative effect on model-predicted responses, but further experimental research is needed in order to fully understand and quantify the behavior of bone and suture, especially in terms of fracture.

The parametric studies reported here highlight the ability of computational models to iteratively investigate a phenomenon, but confounding unknowns may have

limited the application of these model results to real-world impact scenarios. One can conclude from the results, however, that caution should be exercised when evaluating the predictions of computational simulations in a forensic arena, as the robustness of the results directly related to input parameters, which must be estimated in some cases. It is suggested that, for any forensic modeling application, a parametric study should be employed to visually illustrate the possible range of results given expected input variance.

CHAPTER 5

CONCLUSIONS

Summary

In this study, two piglet head computational models were developed and validated based on laboratory-produced experimental data. These models employed finite element techniques and constitutive models incorporating failure criteria, and element deletion was utilized to simulate fracture patterns due to blunt impact. Parametric studies were used to exercise the model sensitivity to the selected stress-based failure criterion. A Design of Computer Experiments approach was used to statistically evaluate the repeatability of the fracture pattern results when slight changes are made to the input conditions, such as impactor orientation. It was found that the commercial finite element solver code chosen for this study (LS-DYNA), the available material models do not include sufficient continuum fracture mechanics theory to simulation crack propagation reliably. In concert with technical improvements to the constitutive models, further age- and species-specific biomaterials research is required to differentiate between stages of bone development and incorporate structural morphology. At that point, computational models could be used to determine regional effects of growth and development, as well as failure mode behavior for biomechanical and forensic analyses.

Limitations of the Computational Models

Limitations of this work include the absence of experimentally-determined plasticity behavior for piglet bone, simplifications in the modeling of suture biomechanics, and lack of crack tip propagation algorithms. In studies such as Guan et

al. (2011), large variations were seen in the plastic behavior of bone samples when material properties were reverse-engineered using optimization-based methods. This indicates that local morphological effects may be more noticeable in plasticity versus elasticity. Given that pediatric bone is in a state of flux during development, these local differences are possibly more pronounced, suggesting that this is a very important factor in modeling pediatric bone tissue. Additionally, more rigorous validation and sensitivity studies would be ideal, if more data were available, especially in regard to the sutures.

Failure criteria available in LS-DYNA do not include crack propagation algorithms, although the mathematical theory is well-known. In terms of skull fracture specifically, there is a need to examine appropriate failure criteria for both initiation and propagation. In Appendix 2, several stress-strain contours at the time of peak deflection are reported for the validated piglet skull models. Stress-based criterion, as used by previous pediatric finite element head models, show stress concentrations developing in response to both inbending and outbending. If this is to be used as a failure criterion, it is paramount to be able to assign different thresholds in tension and compression. For strain-based criteria, plastic strain initially develops largely in areas of outbending, but as elements are deleted, the local plastic strain response does not match fracture lines. Principal strains show the same type of response. Although not available as a failure criterion for any current LS-DYNA material model, Green's strain shows no concentration under the impactor, even at peak deflection, and warrants further investigation for computational studies of outbending-induced skull fracture. The strain energy-based criterion used in MAT105 is driven by several factors, such as Von Mises

90

stress and the triaxiality function. It is difficult to determine to which factor this criterion is most sensitive. However, with element elimination, the direction of fracture propagation (from the bone margin towards the center of impact) matches well with the experimental study.

In this study, the two computational models were developed from age-matched, subject-specific geometries. Unfortunately, micro-level skull morphology (such as the growth of a fluid-filled spongy bone layer in the 21-day-old model) could be not incorporated at this time. The major behavior differences between the two models were driven by the ratio of bone strength to suture strength, which was higher for the younger piglet. Tissue-level validation in future computational models of this type would be appropriate and allow for accurate prediction of fracture pattern instead of initiation site only.

Closing Remarks and Future Work

The use of computational modeling in this work allows for the minimization of anatomical variability inherent in laboratory tests such as age and level of biological development, as well as local skull curvature and thickness variations. With proper validation, confidence in model predictions for specific impact events should be high, although these computational models may not perform well in all impact scenarios in terms of quantitative biomechanical responses for validation or fracture pattern. The development of these models was specific to parietal fracture through direct impact. However, the comparison of the two model geometries, representing different levels of development within a pediatric population, indicate that age-related changes can have significant biomechanical effect that can be replicated even with limited data.

Models developed in this work do not include the intracranial contents, because focus was placed on skull fracture. Gurdjian and Lissner (1945) showed experimentally that the intracranial contents did not affect fracture patterns, though the overall biomechanics and tolerance may be affected. Some finite element models of the infant head in literature showed that the brain stiffness affected skull response, but none of these studies utilized failure modeling techniques or concentrated on replicating skull fracture patterns. In future work, a brain model should be developed to investigate concomitant skull fracture and brain injury, as well as to better understand the role of suture flexure in pediatric closed head injuries.

Although a direct age correlation relationship between piglets and children is not known for the skull as a whole, the same basic biomechanical principles apply. The long-term goals of this project involve translating the methods presented here into an infant head model and developing a tool for the forensic practitioner. Currently, the incompleteness of an age-matched material behavior dataset for pediatric subjects is a major obstacle to this endeavor. More research is needed in this area. Additionally, although some anatomical effects can be accounted for by using subject-specific geometries, structural effects on the micro level may pose more difficulty. Limiting the first attempts to infants of less than three months of age, before the diploë layer begins to develop would be a good first step in adapting the techniques presented here into human use. Once suture behavior is more clearly understood, this skull fracture model could be incorporated with a brain injury model to give a much clearer picture of head injury biomechanics in the pediatric population.

APPENDIX 1

SUMMARY OF PEDIATRIC HEAD IMPACT MODELS IN THE LITERATURE

Simplified

Author	Kurtz, et al. (1998)	Margulies and Thibault (2000)
Figure		
Software	LS-DYNA3D	ANSYS/LS-DYNA3D
Geometry	Idealized	Idealized
Age	3 months	1 month
Elements	• 25,279 eight-node hexagonal solids for the indentor, brain, and CSF • 5,514 four-node quadrilateral shells for the bone, foramen magnum, and dura • 137 two-node, 1D springs	12,772 total elements
Materials	**Elasto-plastic bone:** E = 880 MPa σ_y = 12 MPa σ_t = 47 MPa v = 0.28 **Suture (springs):** K = 189 N/mm **Linear viscoelastic brain (from porcine):** G_0 = 5.99e-3 MPa G = 2.32e-3 MPa β = 9.43e-2 s K = 2110 MPa **Dura and foramen magnum:** E = 100 MPa	**Bone:** E = 1300 MPa ρ = 2150 kg/m^3 v = 0.28 **Suture:** E = 200 MPa ρ = 1130 kg/m^3 v = 0.28 **Linear viscoelastic brain (from porcine):** G_0 = 5.99e-3 MPa G = 2.32e-3 MPa β = 9.43e-2 s K = 2110 MPa **Dura and foramen magnum:** E = 100 MPa

Complex, without face

Author	Coats, et al. (2008)	Zhang, et al. (2007)
Figure		
Software	ABAQUS/Explicit	MSC Patran
Geometry	CT and MRI from 5 week old subject; suture geometry idealized	CT from 7 year old subject, craniofacial sutures reconstructed
Age	1.5 months	7 years
Elements	• 11,066 ten-node tetrahedral solids for brain • 18,706 8-node hexagonal continuum shells for skull • 2,485 4-node membrane elements for sutures • 624 8-node hexagonal solids for scalp	• 57,481 nodes • 52,901 elements
Materials	**Nonlinear isotropic viscoelastic hyperelastic (Odgen) brain (µ and α scaled from adult, using porcine ratios):** µ = 559 Pa α = 0.00845 ρ = 1040 kg/m^3 v = 0.499 **Orthotropic linear elastic bone:** ρ = 2090 kg/m^3 v_{12} = 0.19 Parietal: E1 = 453 Mpa, E2 = 1810 MPa,G = 662 MPa Occipital: E1 = 300 Mpa, E2 = 1200 MPa, G = 503 MPa **Linear elastic suture (ρ and v from adult primate):** ρ = 1130 kg/m^3 v = 0.49 E = 8.1 MPa **Linear elastic scalp (from adult primate):** ρ = 1200 kg/m^3 v = 0.42 E = 16.7 MPa	**Cortical bone:** E=13.7 GPa v = 0.3 **Cancellous bone:** E=7.9 GPa v = 0.3 **Teeth:** E=20.7 GPa v = 0.3 **Suture:** E=7.1 GPa v = 0.45

Complex, with face

Author	Klinich, et al. (2001)	Roth, et al. (2007, 2008)
Figure		
Software	LS-DYNA	
Geometry	CT from 27 week subject; facial geometry from Zygote model	CT from 6 month subject
Age	6 months	6 months
Elements	• Shell: scalp • Solid: CSF, dura, and brain • Thick shell: skull and suture	69,324 bricks 9,187 shells
Author	Klinich, et al. (2001)	Roth, et al. (2007, 2008)
Materials	**Skull (from porcine):** ρ = 2150 kg/m^3 E = 3.0 GPa v = 0.22 **Suture (from porcine):** ρ = 2150 kg/m^3 E = 1.95 GPa v = 0.22 **Brain (from porcine):** G_0 = 5.99 kPa , G = 2.32 kPa β = 9.43e-2 s K = 2110 MPa **CSF (from adult):** ρ = 1040 kg/m^3 E = 70 kPa v = 0.499 **Dura (from adult):** ρ = 1133 kg/m^3 E = 31.5 MPa v = 0.45 **Scalp (from adult):** ρ = 1200 kg/m^3 E = 17 MPa v = 0.42 **Face (estimated):** ρ = 9000 kg/m^3 E = 30 kPa v = 0.22	**Skull:** ρ = 2150 kg/m^3 E = 2.5 GPa v = 0.22 **Suture:** ρ = 2150 kg/m^3 E = 1.5 GPa v = 0.22 **Brain (from porcine):** G_0 = 5.99 kPa G = 2.32 kPa β = 9.43e-2 s K = 2110 MPa **CSF (from adult):** ρ = 1040 kg/m^3 E = 12 kPa v = 0.49 **Dura (from adult):** ρ = 1040 kg/m^3 E = 31.5 GPa v = 0.45 **Scalp (from adult):** ρ = 1200 kg/m^3 E = 16.7 MPa v = 0.42

APPENDIX 2
STRESS-STRAIN CONTOURS

7 DO SHELL e=7 NodeSurfErode thin membr
Time =   1.6
Contours of Effective Plastic Strain
max ipt. value
 min=0, at elem# 1354270
 max=0.0836384, at elem# 3020446
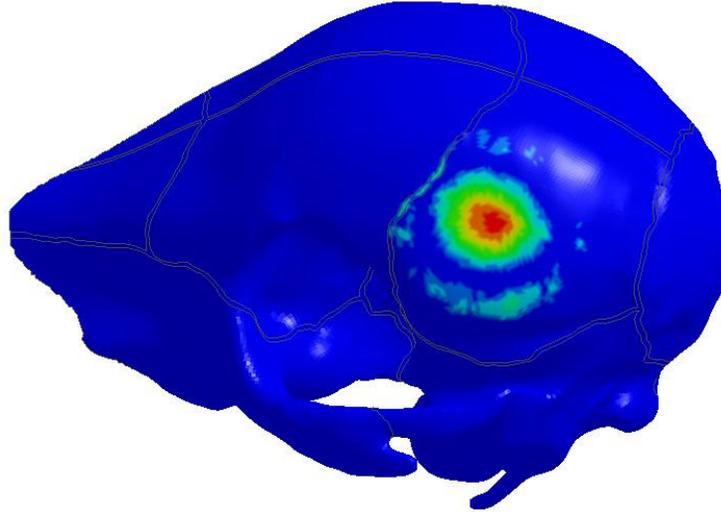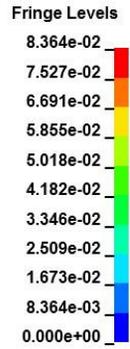
Fringe Levels

8.364e-02 _
7.527e-02 _
6.691e-02 _
5.855e-02 _
5.018e-02 _
4.182e-02 _
3.346e-02 _
2.509e-02 _
1.673e-02 _
8.364e-03 _
0.000e+00 _

21 DO SHELL e=5
Time =   1.6
Contours of Effective Plastic Strain
max ipt. value
 min=0, at elem# 800089
 max=0.0828938, at elem# 904938

Fringe Levels

8.289e-02 _
7.460e-02 _
6.632e-02 _
5.803e-02 _
4.974e-02 _
4.145e-02 _
3.316e-02 _
2.487e-02 _
1.658e-02 _
8.289e-03 _
0.000e+00 _

X   Z
Y
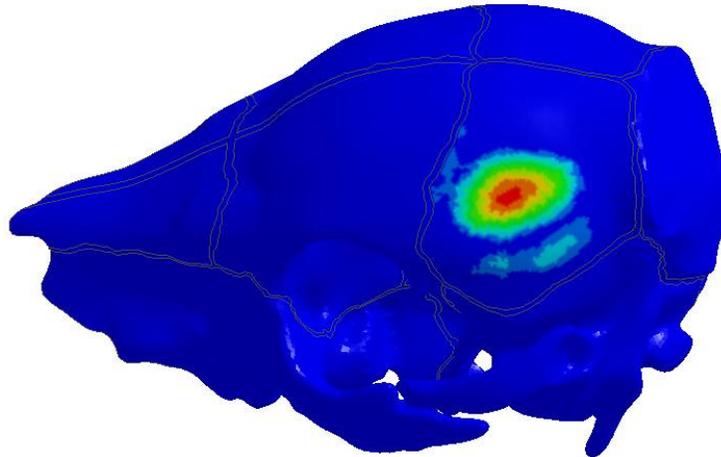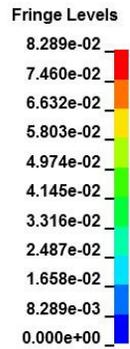
7 DO SHELL e=7 NodeSurfErode thin membr
Time =   1.6
Contours of Effective Stress (v-m)
max ipt. value
 min=0, at elem# 35961
 max=0.229664, at elem# 1355182

Fringe Levels

2.297e-01 _
2.067e-01 _
1.837e-01 _
1.608e-01 _
1.378e-01 _
1.148e-01 _
9.187e-02 _
6.890e-02 _
4.593e-02 _
2.297e-02 _
0.000e+00 _

X __ Z
Y
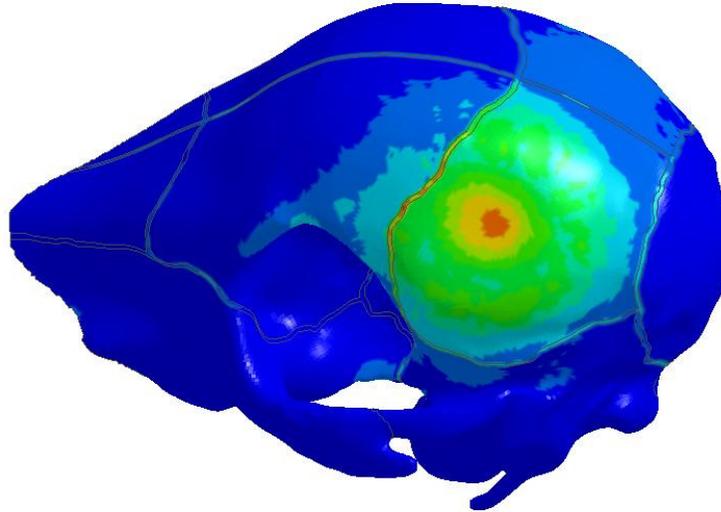
21 DO SHELL e=5
Time =   1.6
Contours of Effective Stress (v-m)
max ipt. value
 min=0, at elem# 800123
 max=0.203615, at elem# 904938
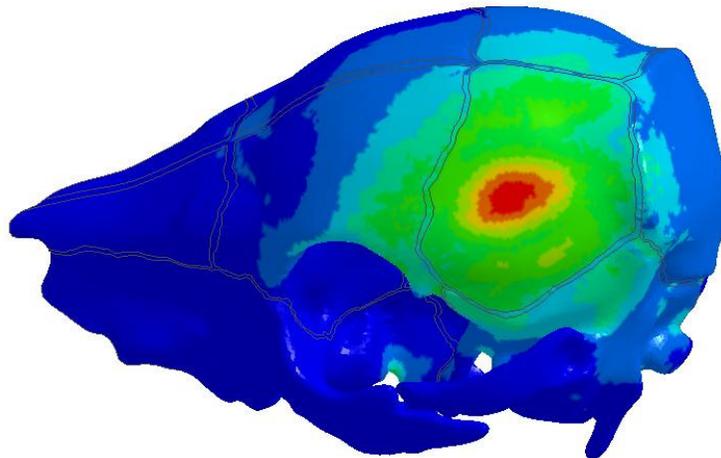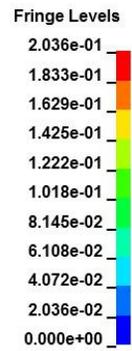
Fringe Levels

2.036e-01 _
1.833e-01 _
1.629e-01 _
1.425e-01 _
1.222e-01 _
1.018e-01 _
8.145e-02 _
6.108e-02 _
4.072e-02 _
2.036e-02 _
0.000e+00 _

X __ Z
Y

7 DO SHELL e=7 NodeSurfErode thin membr
Time =   1.6
Contours of Maximum Principal Stress
max ipt. value
 min=0, at elem# 35961
 max=0.180603, at elem# 1356891
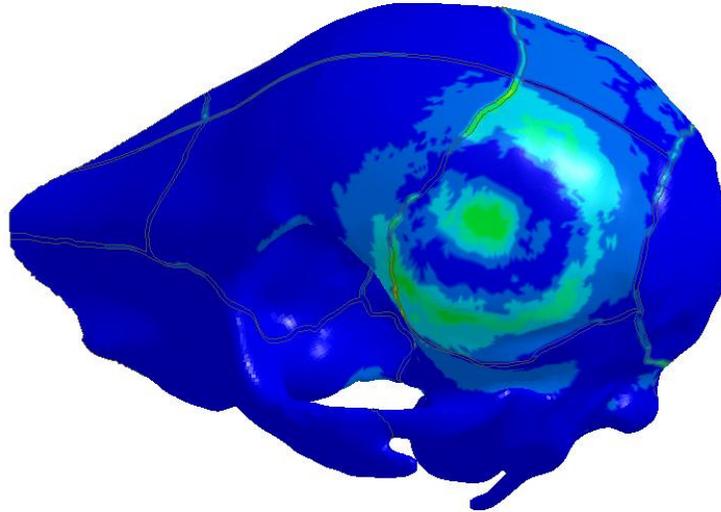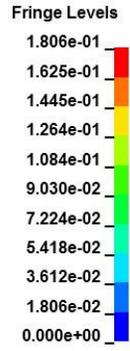
Fringe Levels

1.806e-01
1.625e-01
1.445e-01
1.264e-01
1.084e-01
9.030e-02
7.224e-02
5.418e-02
3.612e-02
1.806e-02
0.000e+00

X   Z
Y

21 DO SHELL e=5
Time =   1.6
Contours of Maximum Principal Stress
max ipt. value
 min=0, at elem# 800123
 max=0.113181, at elem# 908074
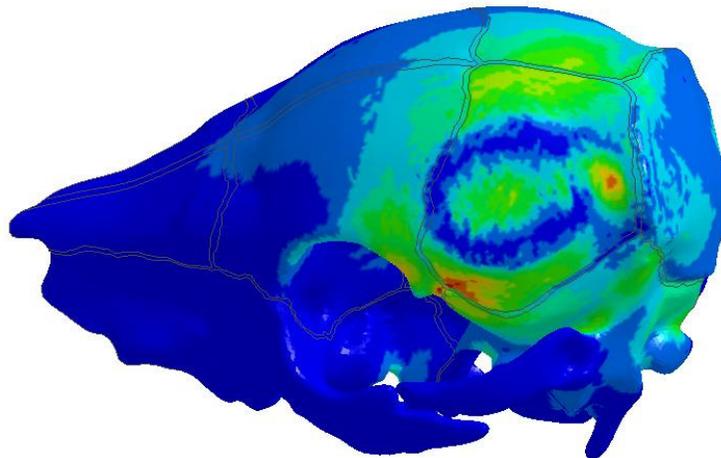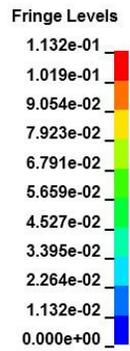
Fringe Levels

1.132e-01
1.019e-01
9.054e-02
7.923e-02
6.791e-02
5.659e-02
4.527e-02
3.395e-02
2.264e-02
1.132e-02
0.000e+00

X   Z
Y

7 DO SHELL e=7 NodeSurfErode thin membr
Time =   1.6
Contours of 2nd Principal Stress
max ipt. value
 min=-0.0512149, at elem# 1355197
 max=0.0699498, at elem# 3002082

Fringe Levels

6.995e-02
5.783e-02
4.572e-02
3.360e-02
2.148e-02
9.367e-03
-2.749e-03
-1.487e-02
-2.698e-02
-3.910e-02
-5.121e-02

X — Z
Y
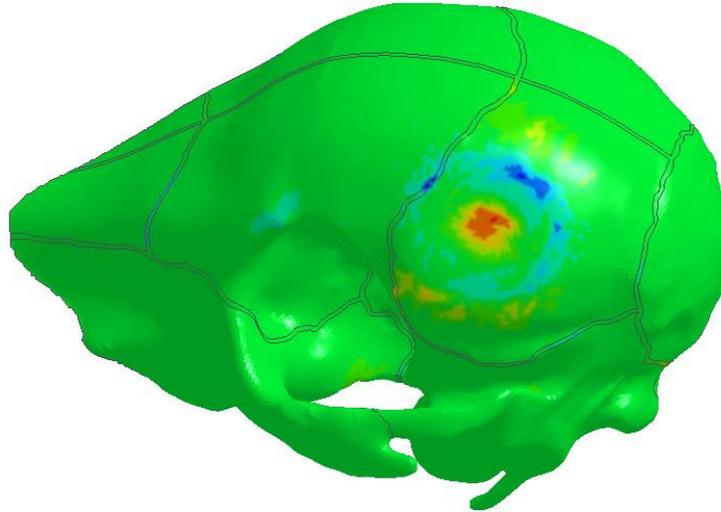
21 DO SHELL e=5
Time =   1.6
Contours of 2nd Principal Stress
max ipt. value
 min=-0.0626318, at elem# 907465
 max=0.0531991, at elem# 800406
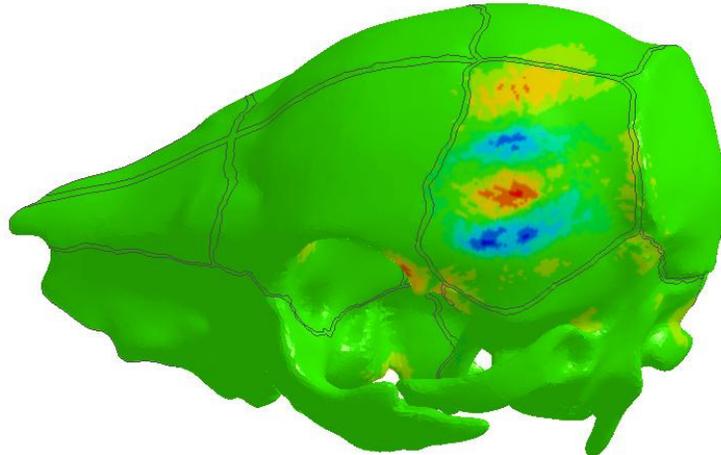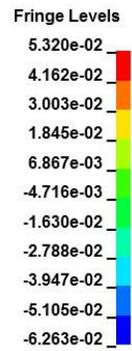
Fringe Levels

5.320e-02
4.162e-02
3.003e-02
1.845e-02
6.867e-03
-4.716e-03
-1.630e-02
-2.788e-02
-3.947e-02
-5.105e-02
-6.263e-02

X — Z
Y

7 DO SHELL e=7 NodeSurfErode thin membr
Time =   1.6
Contours of Minimum Principal Stress
max ipt. value
 min=-0.19222, at elem# 1355196
 max=0, at elem# 35961

Fringe Levels

2.776e-17
-1.922e-02
-3.844e-02
-5.767e-02
-7.689e-02
-9.611e-02
-1.153e-01
-1.346e-01
-1.538e-01
-1.730e-01
-1.922e-01
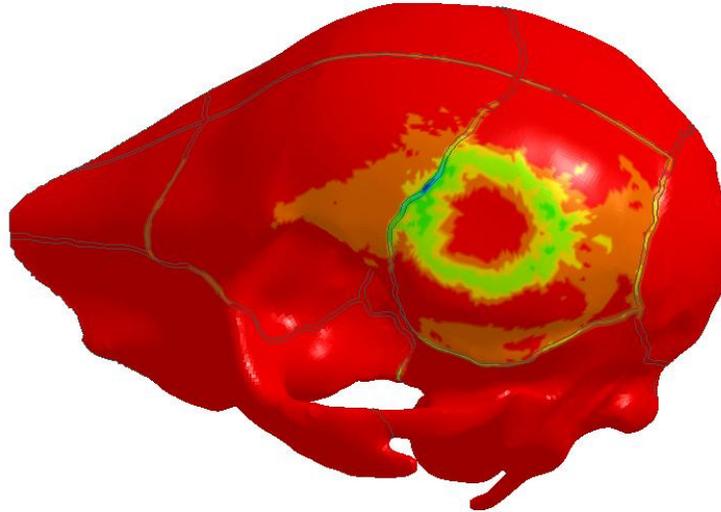
21 DO SHELL e=5
Time =   1.6
Contours of Minimum Principal Stress
max ipt. value
 min=-0.107749, at elem# 904767
 max=0, at elem# 800123
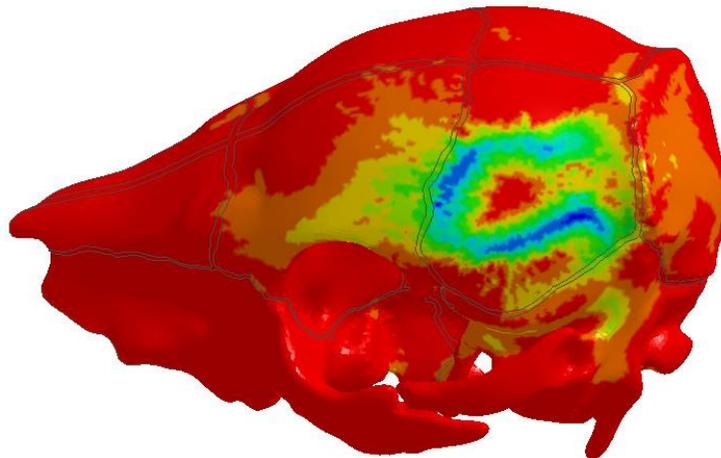
Fringe Levels

0.000e+00
-1.077e-02
-2.155e-02
-3.232e-02
-4.310e-02
-5.387e-02
-6.465e-02
-7.542e-02
-8.620e-02
-9.697e-02
-1.077e-01

7 DO SHELL e=7 NodeSurfErode thin membr
Time =   1.6
Contours of LS Plastic Strain or Hourglass Energy
 min=0, at elem# 1354270
 max=0.0398321, at elem# 1355182

Fringe Levels
3.983e-02
3.585e-02
3.187e-02
2.788e-02
2.390e-02
1.992e-02
1.593e-02
1.195e-02
7.966e-03
3.983e-03
0.000e+00
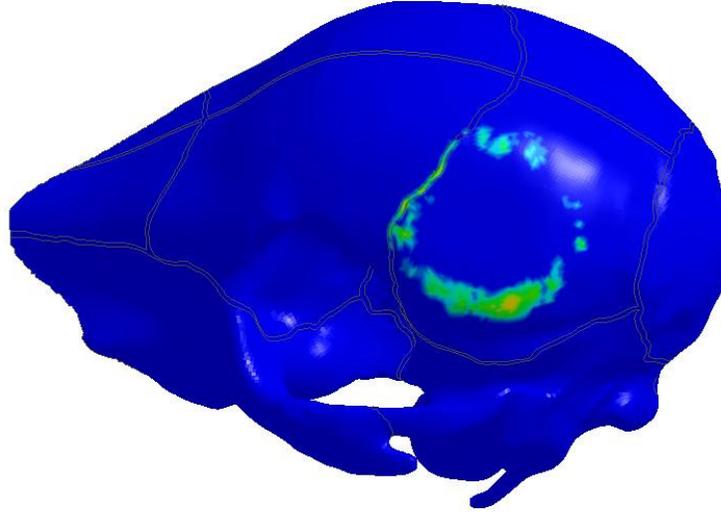
21 DO SHELL e=5
Time =   1.6
Contours of LS Plastic Strain or Hourglass Energy
 min=0, at elem# 800089
 max=0.0266843, at elem# 905469
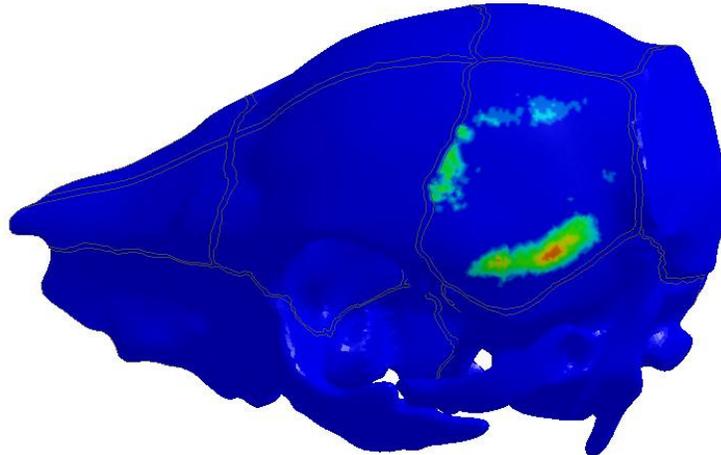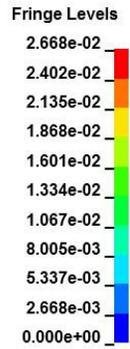
Fringe Levels
2.668e-02
2.402e-02
2.135e-02
1.868e-02
1.601e-02
1.334e-02
1.067e-02
8.005e-03
5.337e-03
2.668e-03
0.000e+00

7 DO SHELL e=7 NodeSurfErode thin membr
Time =   1.6
Contours of US Plastic Strain or Element Timestep
 min=0, at elem# 1354270
 max=0.0836384, at elem# 3020446

Fringe Levels

8.364e-02
7.527e-02
6.691e-02
5.855e-02
5.018e-02
4.182e-02
3.346e-02
2.509e-02
1.673e-02
8.364e-03
0.000e+00

X Z
Y

21 DO SHELL e=5
Time =   1.6
Contours of US Plastic Strain or Element Timestep
 min=0, at elem# 800089
 max=0.0828938, at elem# 904938

Fringe Levels

8.289e-02
7.460e-02
6.632e-02
5.803e-02
4.974e-02
4.145e-02
3.316e-02
2.487e-02
1.658e-02
8.289e-03
0.000e+00

X Z
Y
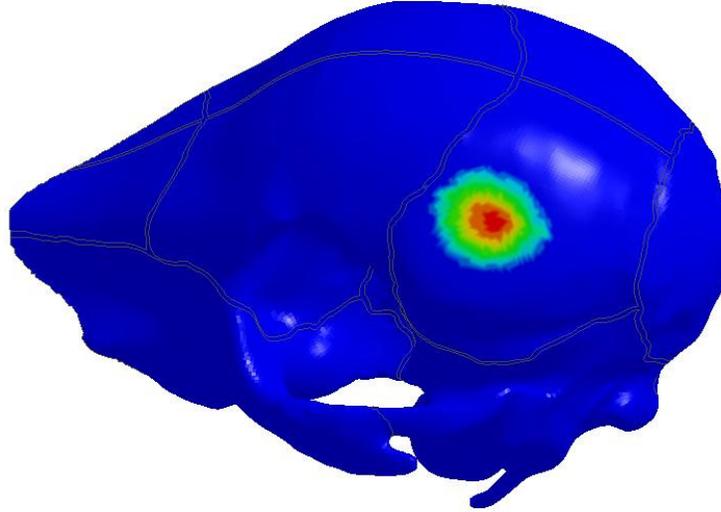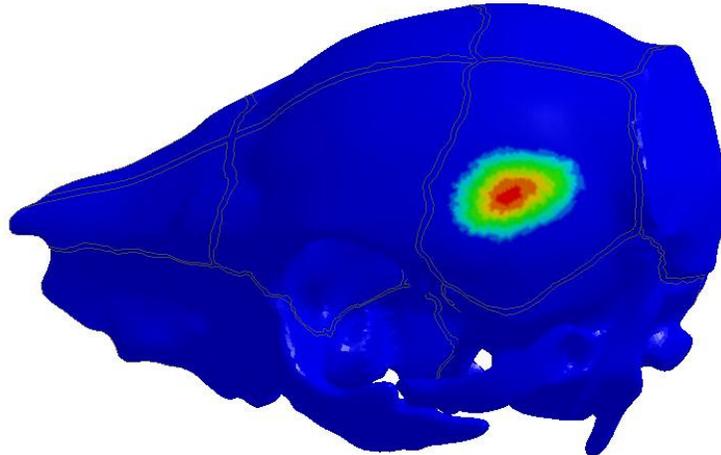
7 DO SHELL e=7 NodeSurfErode thin membr
Time = 1.6
Contours of Triaxiality Factor
max ipt. value
 min=-0.595404, at elem# 3020019
 max=0.659207, at elem# 2975643

Fringe Levels
6.592e-01
5.337e-01
4.083e-01
2.828e-01
1.574e-01
3.190e-02
-9.356e-02
-2.190e-01
-3.445e-01
-4.699e-01
-5.954e-01
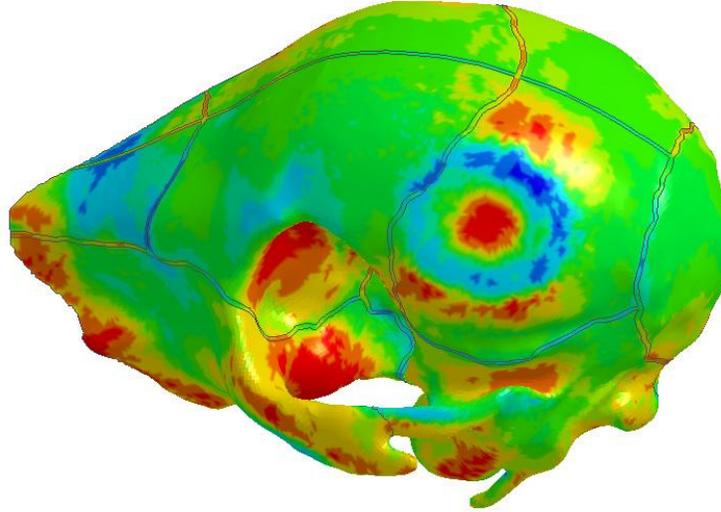
21 DO SHELL e=5
Time = 1.6
Contours of Triaxiality Factor
max ipt. value
 min=-0.623326, at elem# 972467
 max=0.664062, at elem# 849393
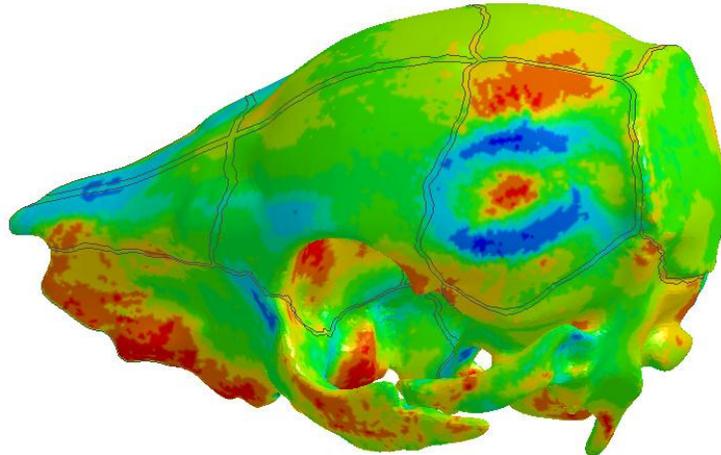
Fringe Levels
6.641e-01
5.353e-01
4.066e-01
2.778e-01
1.491e-01
2.037e-02
-1.084e-01
-2.371e-01
-3.658e-01
-4.946e-01
-6.233e-01

7 DO SHELL e=7 NodeSurfErode thin membr
Time = 1.6
Contours of Mean Strain-Green St Venant
 min=-0.0230995, at elem# 1355147
 max=0.0119403, at elem# 1356975

Fringe Levels

1.194e-02
8.436e-03
4.932e-03
1.428e-03
-2.076e-03
-5.580e-03
-9.084e-03
-1.259e-02
-1.609e-02
-1.960e-02
-2.310e-02

X — Z
Y
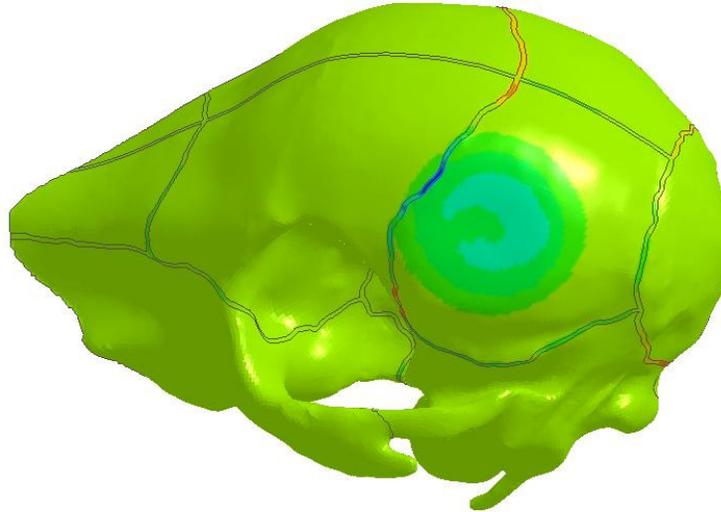
21 DO SHELL e=5
Time = 1.6
Contours of Mean Strain-Green St Venant
 min=-0.0230467, at elem# 904559
 max=0.00361732, at elem# 834742
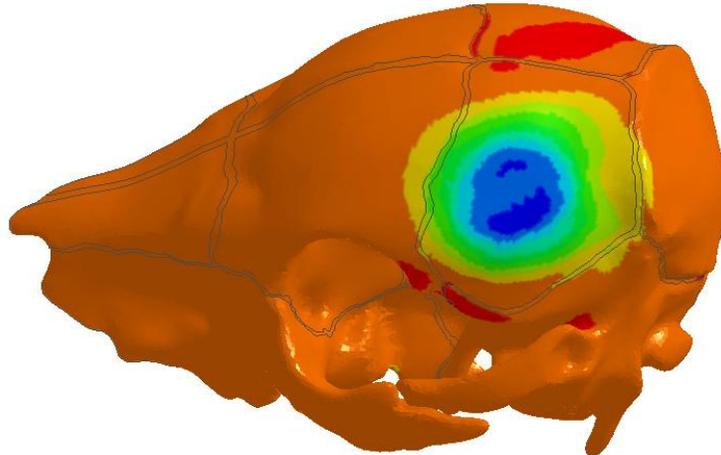
Fringe Levels

3.617e-03
9.509e-04
-1.715e-03
-4.382e-03
-7.048e-03
-9.715e-03
-1.238e-02
-1.505e-02
-1.771e-02
-2.038e-02
-2.305e-02

X — Z
Y

7 DO SHELL e=7 NodeSurfErode thin membr
Time = 1.6
Contours of Effective Strain (v-m)-Green St Venant
min=0, at elem# 35961
max=0.0602767, at elem# 1355193

Fringe Levels

6.028e-02
5.425e-02
4.822e-02
4.219e-02
3.617e-02
3.014e-02
2.411e-02
1.808e-02
1.206e-02
6.028e-03
0.000e+00
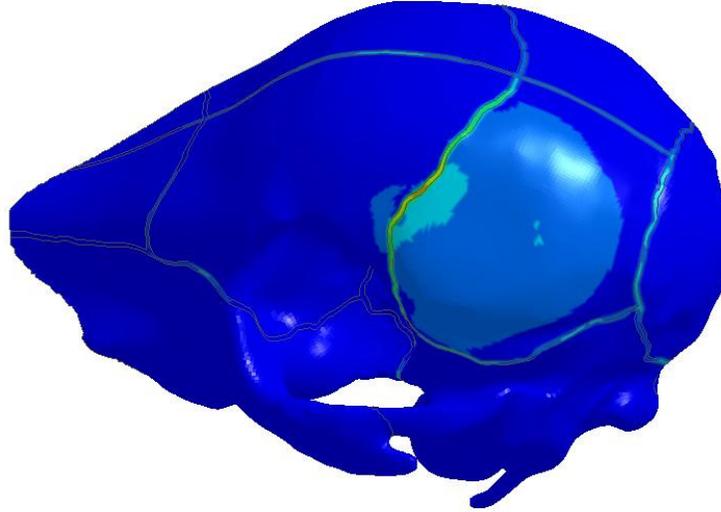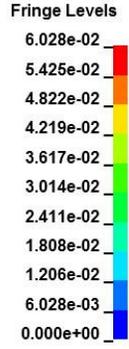
21 DO SHELL e=5
Time = 1.6
Contours of Effective Strain (v-m)-Green St Venant
min=0, at elem# 800123
max=0.028991, at elem# 904187
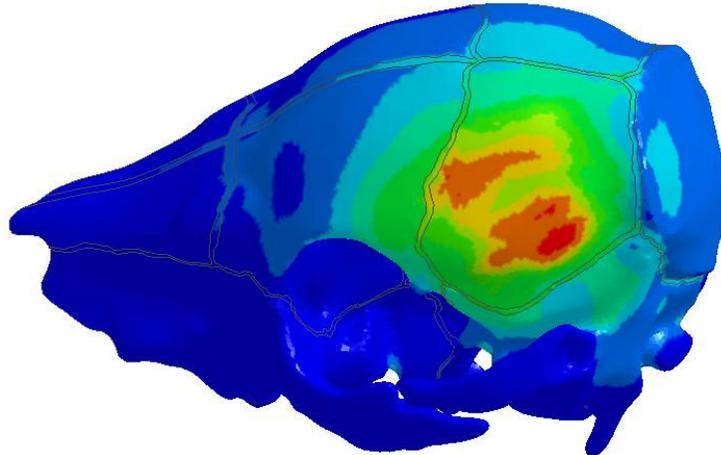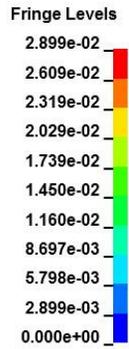
Fringe Levels

2.899e-02
2.609e-02
2.319e-02
2.029e-02
1.739e-02
1.450e-02
1.160e-02
8.697e-03
5.798e-03
2.899e-03
0.000e+00

7 DO SHELL e=7 NodeSurfErode thin membr
Time = 1.6
Contours of 1st Principal Strain-Green St Venant
 min=-2.82227e-07, at elem# 3002426
 max=0.0484114, at elem# 1356891

Fringe Levels

4.841e-02
4.357e-02
3.873e-02
3.389e-02
2.905e-02
2.421e-02
1.936e-02
1.452e-02
9.682e-03
4.841e-03
-2.822e-07
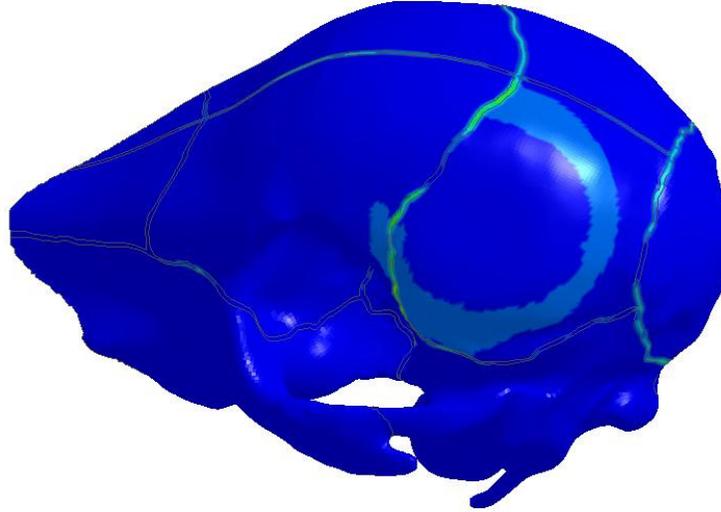
21 DO SHELL e=5
Time = 1.6
Contours of 1st Principal Strain-Green St Venant
 min=-2.76338e-07, at elem# 896200
 max=0.0174053, at elem# 804620
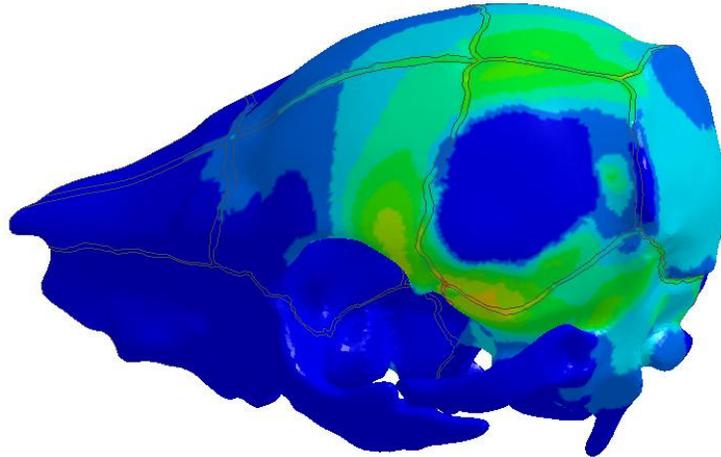
Fringe Levels

1.741e-02
1.566e-02
1.392e-02
1.218e-02
1.044e-02
8.703e-03
6.962e-03
5.221e-03
3.481e-03
1.740e-03
-2.763e-07

7 DO SHELL e=7 NodeSurfErode thin membr
Time =   1.6
Contours of 2nd Principal Strain-Green St Venant
 min=-0.0158644, at elem# 3020009
 max=0.000396386, at elem# 2975105

Fringe Levels
3.964e-04
-1.230e-03
-2.856e-03
-4.482e-03
-6.108e-03
-7.734e-03
-9.360e-03
-1.099e-02
-1.261e-02
-1.424e-02
-1.586e-02
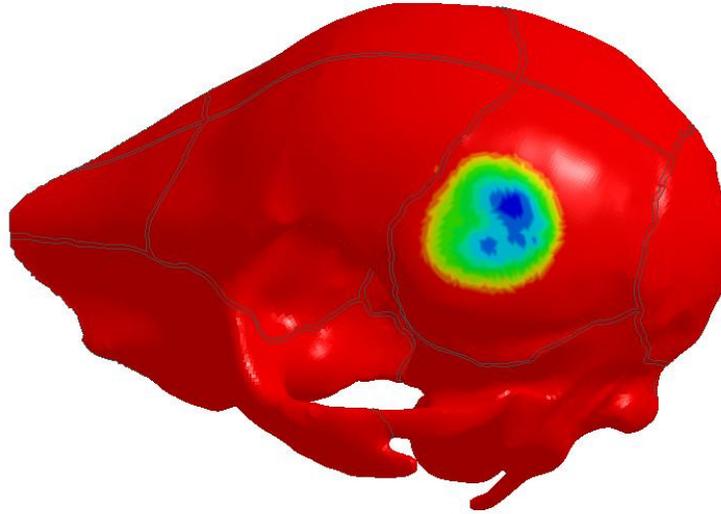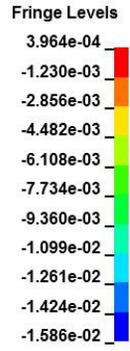
21 DO SHELL e=5
Time =   1.6
Contours of 2nd Principal Strain-Green St Venant
 min=-0.0302679, at elem# 905982
 max=0.000512058, at elem# 801033
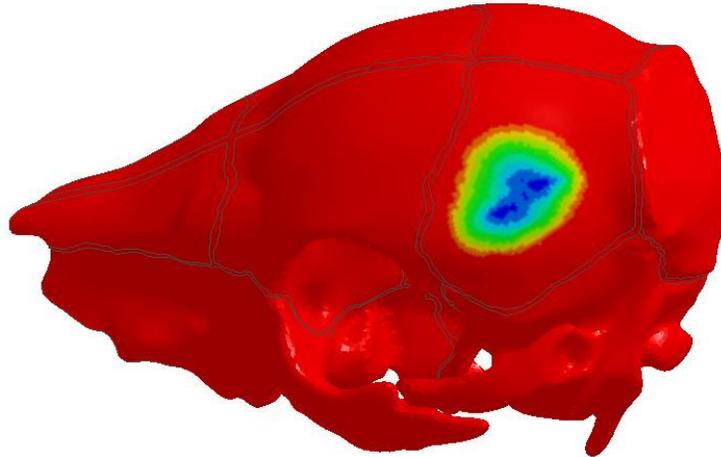
Fringe Levels
5.121e-04
-2.566e-03
-5.644e-03
-8.722e-03
-1.180e-02
-1.488e-02
-1.796e-02
-2.103e-02
-2.411e-02
-2.719e-02
-3.027e-02

7 DO SHELL e=7 NodeSurfErode thin membr
Time = 1.6
Contours of 3rd Principal Strain-Green St Venant
 min=-0.0795273, at elem# 1355195
 max=2.32485e-09, at elem# 2970535

Fringe Levels

2.325e-09
-7.953e-03
-1.591e-02
-2.386e-02
-3.181e-02
-3.976e-02
-4.772e-02
-5.567e-02
-6.362e-02
-7.157e-02
-7.953e-02
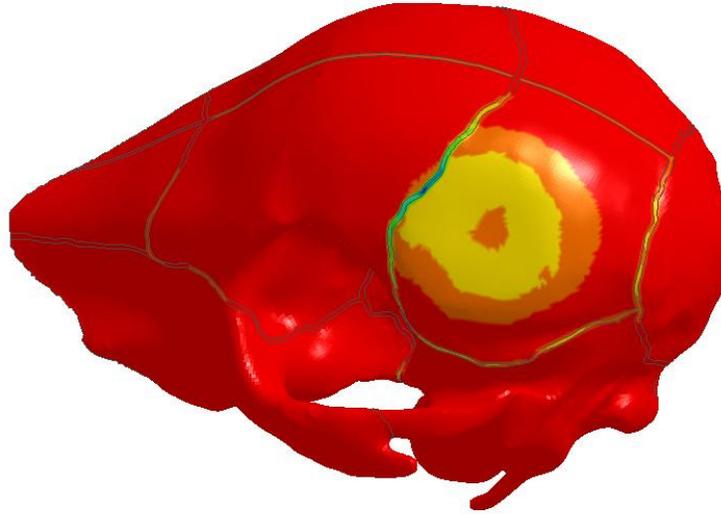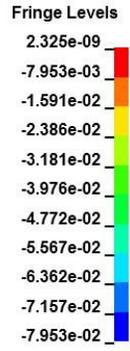
21 DO SHELL e=5
Time = 1.6
Contours of 3rd Principal Strain-Green St Venant
 min=-0.0459489, at elem# 904280
 max=8.26386e-10, at elem# 819348

Fringe Levels

8.264e-10
-4.595e-03
-9.190e-03
-1.378e-02
-1.838e-02
-2.297e-02
-2.757e-02
-3.216e-02
-3.676e-02
-4.135e-02
-4.595e-02
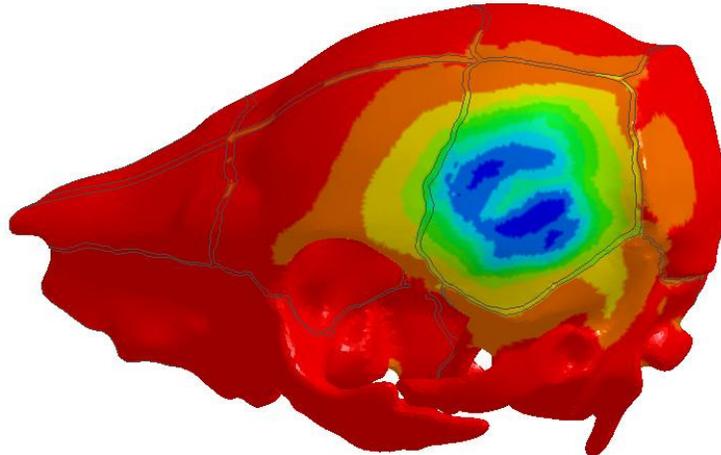
APPENDIX 3

FULL FACTORIAL DESIGN OF COMPUTER EXPERIMENTS RESULTS

|	
21 DO SHELL 105 run8 Time = 1.1173 X Z	**0** **DC = 0.001** **E = 8 GPa** **EPSD = 0.010**
21 DO SHELL 105 run8 Time = 1.5727 X Z	**1** **DC = 0.001** **E = 8 GPa** **EPSD = 0.015**
NO FRACTURE	**2** **DC = 0.001** **E = 8 GPa** **EPSD = 0.020**
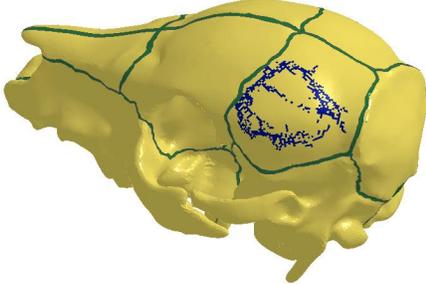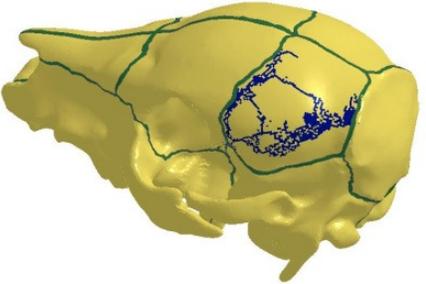
21 DO SHELL 105 run8 Time = 1.7469	**3** **DC = 0.001** **E = 10 GPa** **EPSD = 0.010**
21 DO SHELL 105 run8 Time = 1.283	**4** **DC = 0.001** **E = 10 GPa** **EPSD = 0.015**
21 DO SHELL 105 run8 Time = 2	**5** **DC = 0.001** **E = 10 GPa** **EPSD = 0.020**
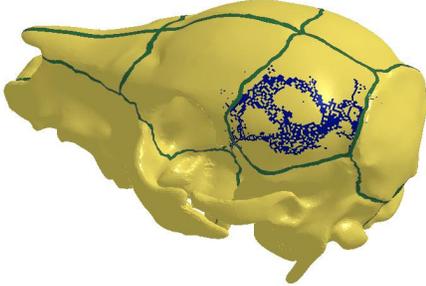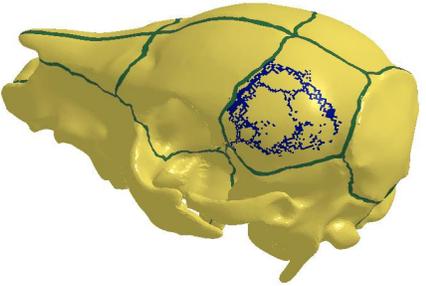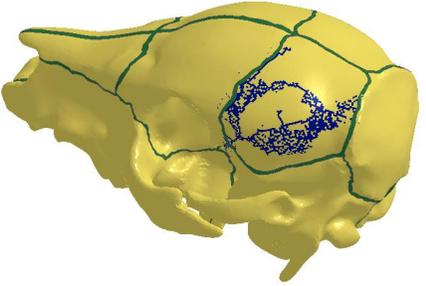
21 DO SHELL 105 run8 Time = 1.0236	**6** **DC = 0.001** **E = 12 GPa** **EPSD = 0.010**
21 DO SHELL 105 run8 Time = 1.1465	**7** **DC = 0.001** **E = 12 GPa** **EPSD = 0.015**
21 DO SHELL 105 run8 Time = 1.2741	**8** **DC = 0.001** **E = 12 GPa** **EPSD = 0.020**
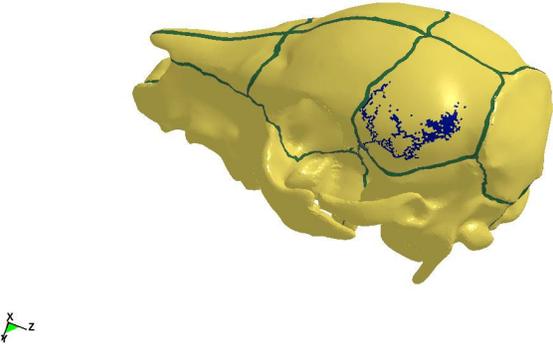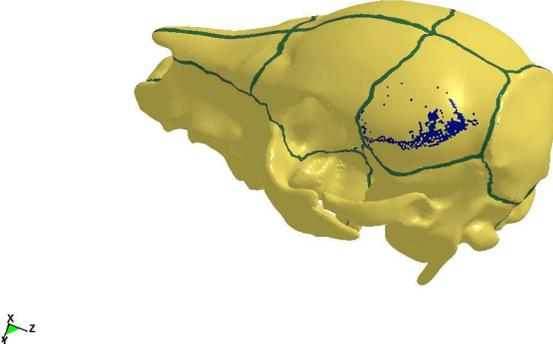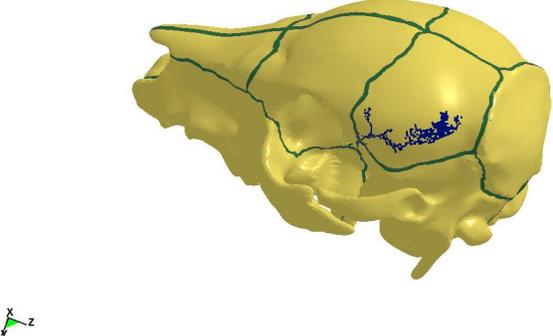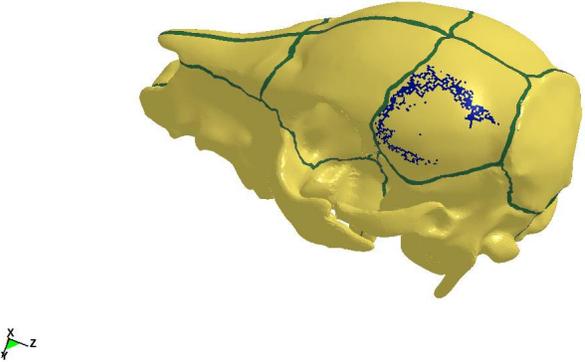
21 DO SHELL 105 run8 Time = 1.1502	**9** **DC = 0.002** **E = 8 GPa** **EPSD = 0.010**
21 DO SHELL 105 run8 Time = 1.4191	**10** **DC = 0.002** **E = 8 GPa** **EPSD = 0.015**
21 DO SHELL 105 run8 Time = 1.4379	**11** **DC = 0.002** **E = 8 GPa** **EPSD = 0.020**
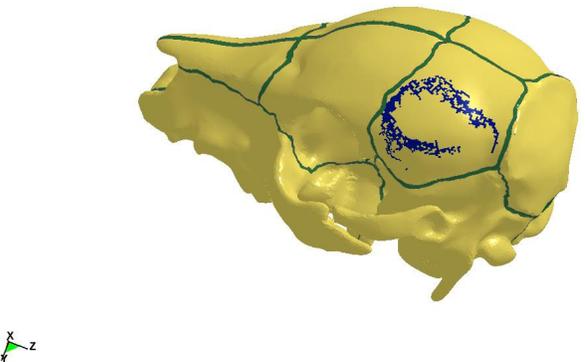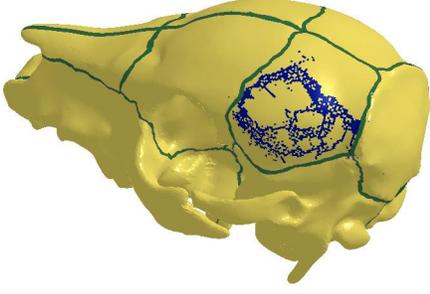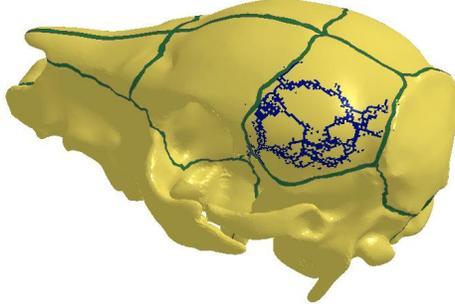
	12 **DC = 0.002** **E = 10 GPa** **EPSD = 0.010**
	13 **DC = 0.002** **E = 10 GPa** **EPSD = 0.015**
NO FRACTURE	**14** **DC = 0.002** **E = 10 GPa** **EPSD = 0.020**

21 DO SHELL 105 run8
Time = 1.1857
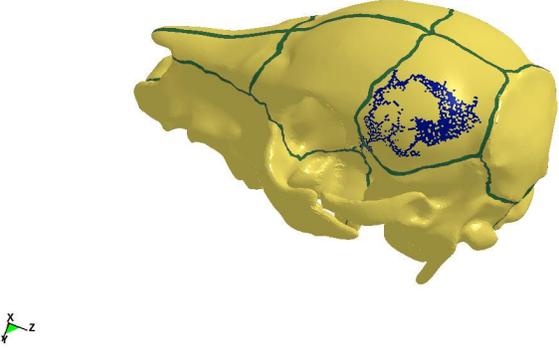
15

DC = 0.002
E = 12 GPa
EPSD = 0.010

21 DO SHELL 105 run8
Time = 1.1965
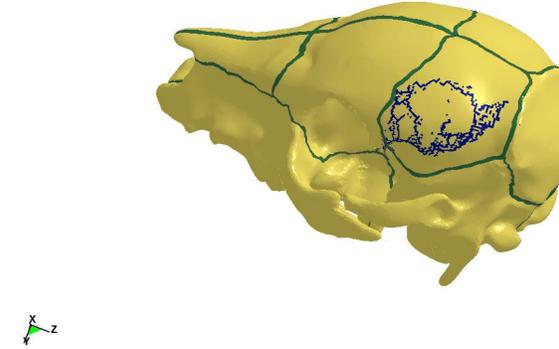
16

DC = 0.002
E = 12 GPa
EPSD = 0.015

21 DO SHELL 105 run8
Time = 1.36
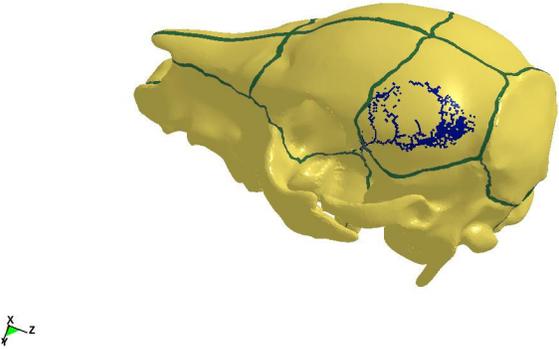
17

DC = 0.002
E = 12 GPa
EPSD = 0.020

21 DO SHELL 105 run8
Time =   1.1786
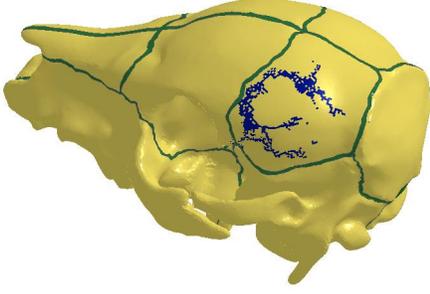
18

DC = 0.003
E = 8 GPa
EPSD = 0.010

21 DO SHELL 105 run8
Time =   1.3949
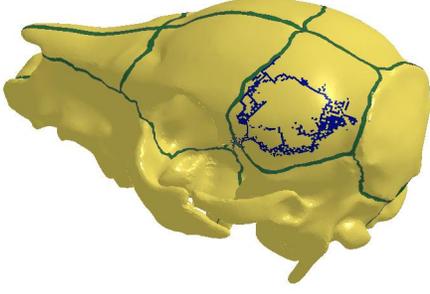
19

DC = 0.003
E = 8 GPa
EPSD = 0.015

21 DO SHELL 105 run8
Time =   1.6982
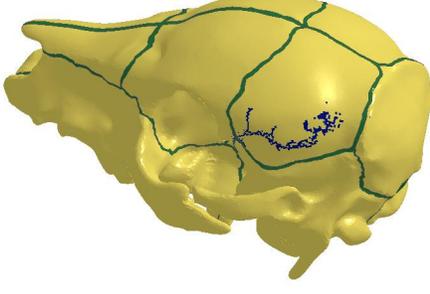
20

DC = 0.003
E = 8 GPa
EPSD = 0.020

21 DO SHELL 105 run8 Time = 1.1233 X Z	**21** **DC = 0.003** **E = 10 GPa** **EPSD = 0.010**
21 DO SHELL 105 run8 Time = 2 X Z	**22** **DC = 0.003** **E = 10 GPa** **EPSD = 0.015**
NO FRACTURE	**23** **DC = 0.003** **E = 10 GPa** **EPSD = 0.020**
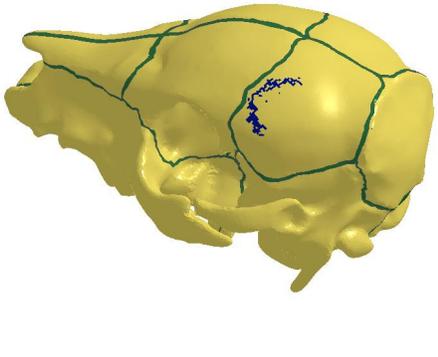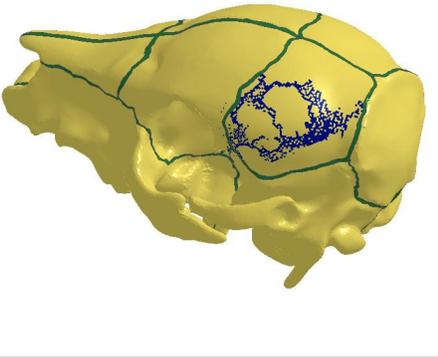
21 DO SHELL 105 run8 Time = 1.1035 	**24** **DC = 0.003** **E = 12 GPa** **EPSD = 0.010**
	25 **DC = 0.003** **E = 12 GPa** **EPSD = 0.015**
21 DO SHELL 105 run8 Time = 1.333 	**26** **DC = 0.003** **E = 12 GPa** **EPSD = 0.020**
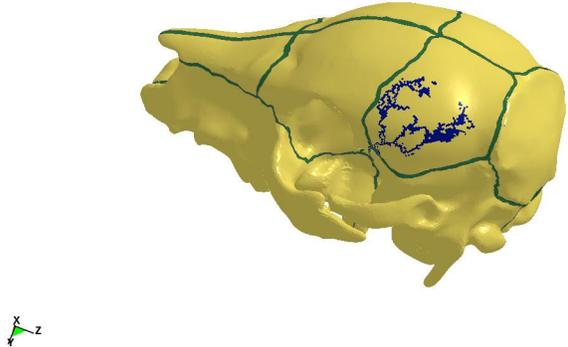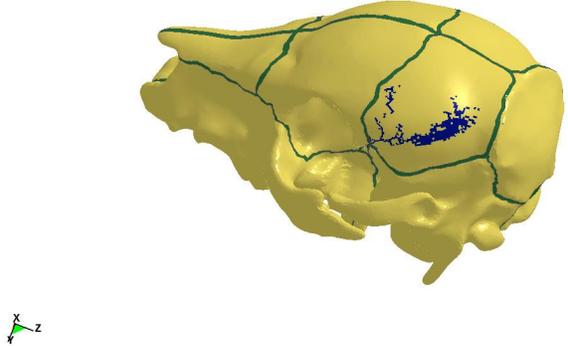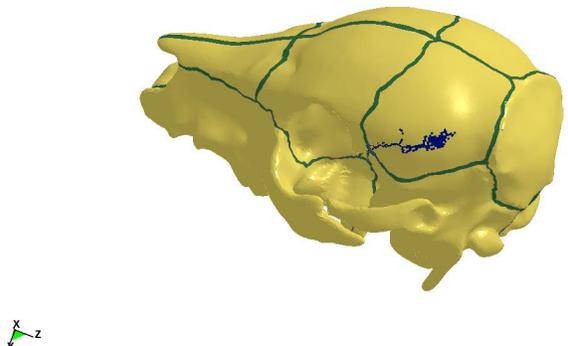
REFERENCES

Aerssens, J., S. Boonen, et al. (1998). "Interspecies differences in bone composition, density, and quality: potential implications for in vivo bone research." Endocrinology **139**(2): 663-670.

Baumer, T. G., N.V. Passalaqua, et al. (2010). "Age-dependent fracture characteristics of rigid and compliant surface impacts on the infant skull—a porcine model." J Forensic Sci. **55**(4):933-937.

Baumer, T. G., B. J. Powell, et al. (2009). "Age dependent mechanical properties of the infant porcine parietal bone and a correlation to the human." J Biomech Eng. **131**(11)111006.

Baumer, T. G. (2009). *Material property documentation and fracture analyses of the developing skull.* MS Thesis, Michigan State University, USA.

Berstad, T., Hopperstad, O.S., Lademo, O.-G. and Malo, K.A. (1999). "Computational model of ductile damage and fracture in shell analysis", Second European LS-DYNA Conference, Gothenburg, June 14-15.

Burstein, A. H., J. M. Zika, et al. (1975). "Contribution of collagen and mineral to the elastic-plastic properties of bone." J Bone Joint Surg Am. **57**: 956-961.

Bylski, D., T. J. Kriewall, et al. (1986). "Mechanical behavior of fetal dura mater under large deformation biaxial tension." J Biomech **19**(1): 19-26.

Coats, B. and S. S. Margulies (2006). "Material properties of human infant skull and suture at high rates." J Neurotrauma **23**(8): 1222-1232.

Coats, B., S. S. Margulies, et al. (2007). "Parametric study of head impact in the infant." Stapp Car Crash J **51**: 1-15.

Currey, J. D. (1969). "The mechanical consequences of variation in the mineral content of bone." J Biomech **2**: 1-11.

Currey, J. D. (1999). "What determines the bending strength of compact bone?" J Exp Biol **202**: 2495-2503.

Desantis Klinich, K., G. M. Hulbert, et al. (2002). "Estimating infant head injury criteria and impact response using crash reconstruction and finite element modeling." Stapp Car Crash J **46**: 165-194.

Dobbing, J. (1964). The later development of the brain and is vulnerability. Scientific foundations of paediatrics. J. A. Davis and J. Dobbing. Londeon, Heinemann Medical.

Franklyn, M., S. Peiris, et al. (2007). "Pediatric material properties: a review of human child and animal surrogates." Crit Rev Biomed Eng **35**(3-4): 197-342.

Gray, H. (1918). Anatomy of the Human Body. W. H. Lewis. Philadelphia, Lea & Febiger.

Guan, F., X. Han, et al. (2011). "Application of optimization methodology and specimen-specific finite element models for investigating material properties of rat skull. " Annals of Biomedical Engineering. **39**(1):85-95.

Gurdjian, E. S. and H. R. Lissner (1945). "Study of deformations of the skull by the 'stresscoat' technique." Surg. Gynec. & Obstet. **81**: 679.

Hobbs, C. J. (1984). "Skull fracture and the diagnosis of abuse." Arch Dis Child **59**(3): 246-52.

Holck, P. (2005). "What can a baby's skull withstand? Testing the skull's resistance on an anatomical preparation." Forensic Sci Int **151**(2-3): 187-191.

Hofman MA. (1989). On the evolution and geometry of the brain in mammals. <u>Prog Neurobiol</u> **32**(2):137-58.

Hummel, P. and D. Fortado (2005). "Impacting infant head shapes." <u>Adv Neonatal Care</u> **5**(6): 329-340.

Jans, G., R. Van-Audekercke, et al. (1998). <u>Bending properties of cranial bone segments of newborn children</u>. 11th Conference of the ESB, Toulouse, France.

Kent, R., S. Stacey, et al. (2006). "Biomechanical response of the pediatric abdomen, part 1: development of an experimental model and quantification fo structural response to dynamic belt loading." <u>Stapp Car Crash J</u> **50**: 1-26.

Kogutt, M. S., L. E. Swischuk, et al. (1974). "Patterns of injury and significance of uncommon fractures in the battered child syndrome." <u>Am J Roentgenol Radium Ther Nucl Med</u> **121**(1): 143-9.

Kriewall, T. J. (1982). "Structural, mechanical, and material properties of fetal cranial bone." <u>Am J Obstet Gynecol</u> **143**(6): 707-714.

Kriewall, T. J., G. K. McPherson, et al. (1981). "Bending properties and ash content of fetal cranial bone." <u>J Biomech</u> **14**(2): 73-79.

Kurtz, S. M., K. L. Thibault, et al. (1998). <u>Finite element analysis of the deformation of the human infant head under impact conditions</u>. 8th Injury Prevention Through Biomechanics Symposium, Detroit, Michigan.

Lapeer, R. J. and R. W. Prager (2000). "3D shape recovery of a newborn skull using thin-plate splines." <u>Comput Med Imaging Graph</u> **24**(3): 193-204.

Lapeer, R. J. and R. W. Prager (2001). "Fetal head moulding: finite element analysis of a fetal skull subjected to uterine pressures during the first stage of labour." J Biomech **34**(9): 1125-1133.

Lee, M. C. and R. C. Haut (1989). "Insensitivity of tensile failure properties of human bridging veins to strain rate: implications in biomechanics of subdural hematoma." J Biomech **22**(6-7): 537-542.

Leventhal, J. M., S. A. Thomas, et al. (1993). "Fractures in young children. Distinguishing child abuse from unintentional injuries." Am J Dis Child **147**(1): 87-92.

Li, Z., M. W. Kindig, et al. (2009) "Rib fractures under anterior-posterior dynamic loads: experimental and finite-element study." J Biomech. **43**: 228-234**.**

Loder, R. T. and J. R. Feinberg (2007). "Orthopaedic injuries in children with nonaccidental trauma: demographics and incidence from the 2000 kids' inpatient database." J Pediatr Orthop **27**(4): 421-6.

Margulies, S. S. and K. L. Thibault (2000). "Infant skull and suture properties: measurements and implications for mechanisms of pediatric brain injury." J Biomech Eng **122**(4): 364-371.

Margulies, S. S. and K. L. Thibault (2000). "Infant skull and suture properties: measurements and implications for mechanisms of pediatric brain injury." J Biomech Eng **122**(4): 364-371.

Mather, B. S. (1968). "The effect of variationin specific gravity and ash content on the mechanical properties of human compact bone." J Biomech **1**: 207-210.

McPherson, G. K. and T. J. Kriewall (1980). "Fetal head molding: an investigation utilizing a finite element model of the fetal parietal bone." J Biomech **13**(1): 17-26.

McPherson, G. K. and T. J. Kriewall (1980). "The elastic modulus of fetal cranial bone: a first step towards an understanding of the biomechanics of fetal head molding." J Biomech **13**(1): 9-16.

McPherson, G. K. and T. J. Kriewall (1980). "The elastic modulus of fetal cranial bone: a first step towards an understanding of the biomechanics of fetal head molding." J Biomech **13**(1): 9-16.

Meaney, D. F. (1995). "Biomechanical analysis of diffuse axonal injury." J Neurotrauma **12**: 689-694.

Melvin, J., J. McElhaney, et al. (1970). Development of a mechanical model of the human head- determination of tissue properties and synthetic substitute materials. Proceedings of the 14th Stapp Car Crash Conference, New York, SAE.

Merten, D. F., M. A. Radkowski, et al. (1983). "The abused child: a radiological reappraisal." Radiology **146**: 377-381.

Meservy, C. J., R. Towbin, et al. (1987). "Radiographic characteristics of skull fractures resulting from child abuse." AJR Am J Roentgenol **149**(1): 173-5.

Ommaya, A. K., W. Goldsmith, et al. (2002). "Biomechanics and neuropathology of adult and paediatric head injury." Br J Neurosurg **16**(3): 220-242.

Prange, M. T., G. Kiralyfalvi, et al. (1999). Pediatric rotational inertial brain injury: the relative influence of brain size and mechanical properties. Stapp Car Crash Conference.

Prange, M. T., J. F. Luck, et al. (2004). "Mechanical properties and anthropometry of the human infant head." <u>Stapp Car Crash J</u> **48**: 279-299.

Prasad, P. and R. P. Daniel (1984). "A biomechanical analysis of head, neck, and torso injuries to child surrogates due to sudden torso acceleration." <u>28th Stapp Car Crash Conference</u>.

Reece, R. M. and R. Sege (2000). "Childhood head injuries: accidental or inflicted?" <u>Arch Pediatr Adolesc Med</u> **154**(1): 11-5.

Roth, S., J. S. Raul, et al. (2007). "Finite element analysis of impact and shaking inflicted to a child." <u>Int J Legal Med</u> **121**(3): 223-228.

Runge, C. F., A. Youssef, et al. (1998). <u>Material properties of human infant skull and suture: experiment and numerical analysis</u>. 8th Injury Prevention Through Biomechanics Symposium, Detroit, Michigan.

Runge, C. F., A. Youssef, et al. (1998). <u>Material properties of human infant skull and suture: experiment and numerical analysis</u>.

Thibault, K. L. and S. S. Margulies (1998). "Age-dependent material properties of the porcine cerebrum: effect on pediatric inertial head injury criteria." <u>J Biomech</u> **31**(12): 1119-1126.

Walker, P. L., D. C. Cook, et al. (1997). "Skeletal evidence for child abuse: a physical anthropological perspective." <u>J Forensic Sci</u> **42**(2): 196-207.

Wainwright (1979)

Weber, W. (1984). "[Experimental studies of skull fractures in infants]." <u>Z Rechtsmed</u> **92**(2): 87-94.

Weber, W. (1985). "[Biomechanical fragility of the infant skull]." Z Rechtsmed **94**(2): 93-101.

Worlock, P., M. Stower, et al. (1986). "Patterns of fractures in accidental and non-accidental injury in children: a comparative study." Br Med J (Clin Res Ed) **293**(6539): 100-2.

Yoganandan, N. and F. A. Pintar (2004). "Biomechanics of temporo-parietal skull fracture." Clin Biomech (Bristol, Avon) **19**(3): 225-239.

Yoganandan, N., F. A. Pintar, et al. (1995). "Biomechanics of skull fracture." J Neurotrauma **12**(4): 659-668.

Zhang, H. Z., M. Hou, et al. (2007). "[The finite element study on zygomatic injury by impact in child]." Zhonghua Yi Xue Za Zhi **87**(20): 1420-1422.

ABSTRACT

COMPUTATIONAL SIMULATION OF SKULL FRACTURE PATTERNS
IN PEDIATRIC SUBJECTS USING A PORCINE MODEL

by

CHRISTINA DEVITO WAGNER

May 2012

Advisor: Dr. King-Hay Yang

Major: Biomedical Engineering

Degree: Doctor of Philosophy

In cases of suspected child abuse with skeletal trauma, it is often the role of the injury biomechanist, forensic pathologist, clinical radiologist, and forensic anthropologist to determine the mechanism of injury when the child victims cannot speak for themselves. This is a challenging task, especially for the head, as comprehensive biomechanical data on skull fracture in infants and children do not currently exist, and frequently the determination regarding cause of injury is based on anecdotal evidence from the medical literature and unsubstantiated eyewitness accounts. The current process may result in unreliable autopsy interpretation and miscarriages of justice due to a lack of scientific verification in expert witness testimony. A method to examine the mechanisms of skeletal trauma, specifically skull fracture, in children would be beneficial in providing a solid biomechanical foundation to the forensic investigators in these child abuse cases.

Finite element (FE) computational modeling techniques can be used to simulate failure of materials, including biological materials such as bone. However the efficacy of these methods has not been thoroughly tested against a well-defined experimental dataset, particularly for the pediatric population. The specific aims of this study were: (1)To determine appropriate constitutive laws and material properties for the piglet skull and suture, (2) To predict skull

fracture patterns in a piglet model using FE methods, and (3) To analyze the sensitivity and robustness of these FE techniques for reliable biomechanical and forensic analysis. Results highlight the ability of macro-scale blunt impact computational models to predict fracture initiation sites and the role of computational models in guiding future experimental work.

AUTOBIOGRAPHICAL STATEMENT

Christina DeVito Wagner

Education:

M.S.	2006	Wayne State University, Detroit, Michigan
B.S.E.	2003	University of Iowa, Iowa City, Iowa
B.A.	2003	University of Iowa, Iowa City, Iowa

Selected Publications:

Zhu F, **Wagner C**, Dal Cengio Leonardi A, Jin X, VandeVord P, Chou C, Yang KH, and King AI. Using a gel/plastic surrogate to study the biomechanical response of the head under air shock loading: A combined experimental and numerical investigation. Biomechanics and Modeling in Mechanobiology, in press

Guan F, Han X, Mao H, **Wagner C**, Yeni YN, and Yang KH. Application of optimization methodology and specimen-specific finite element models for investigating material properties of rat skull. Ann Biomed Eng 2011;39(1):85-89.

Yang KH, Mao H, **Wagner C**, Zhu F, Chou CC, and King AI. "Modeling of the Brain for Injury Prevention." Neural Tissue Biomechanics Bilston L (ed.) Berlin: Springer-Verlag, 2011. 69-121.

Zhu F, Mao H, Dal Cengio Leonardi A, **Wagner C**, Chou C, Jin X, Bir C, Vandevord P, Yang KH, and King AI. Development of an FE model of the rat head subjected to air shock loading. Stapp Car Crash J 2010;54:211-225.

Chou C, **Wagner C**, Yang KH, and King AI. A review of tripped rollover methodologies. Int J Vehicle Safety 2009;4(3):185-229.

Kim JE, Li Z, **Huber CD**, Shih AM, Eberhardt AW, Yang KH, King AI, and Soni BK. Finite element model development of a child pelvis with optimization-based material identification. J Biomech 2009;42(13)2191-2195.

Chou CC, **Wagner CD**, Yang KH, King AI, Hu J, Hope K, and Arepally S. A review of math-based CAE tools for rollover simulations. Int J Vehicle Safety 2008; 3(3):236-275.

Franklyn M, Peiris S, **Huber CD**, Yang KH. Pediatric material properties: a review of human child and animal surrogates. Critical Reviews in Biomedical Engineering. 2007;35(1-2):197-342.

Huber CD, Lee JB, Yang KH, King AI. Head injuries in airbag-equipped motor vehicles with special emphasis on AIS 1 and 2 facial and loss of consciousness injuries. Traffic Injury Prevention. 2005 Jun;6(2):170-4.